8-2017

Improved Sample Loading for Plutonium Analysis by Thermal Ionization Mass Spectrometry and Alpha Spectroscopy

Joseph Mannion
Clemson University, jmannio@g.clemson.edu

IMPROVED SAMPLE LOADING FOR PLUTONIUM ANALYSIS BY THERMAL IONIZATION MASS SPECTROMETRY AND ALPHA SPECTROSCOPY

A Dissertation
Presented to
the Graduate School of
Clemson University

In Partial Fulfillment
of the Requirements for the Degree
Doctor of Philosophy
Chemical Engineering

---

by
Joseph Mannion
August 2017

Accepted by:
Scott M. Husson, Committee Chair
Brian A. Powell
David A. Bruce
Douglas E. Hirt

ABSTRACT

Thermal ionization mass spectrometry (TIMS) and alpha spectroscopy are powerful analytical techniques for the detection and characterization of Pu samples. These techniques are important for efforts in environmental monitoring, nuclear safeguards, and nuclear forensics. Measurement sensitivity and accuracy are imperative for these efforts. TIMS is internationally recognized as the "gold standard" for Pu isotopic analysis. Detection of ultra-trace quantities of Pu, on the order of femtograms, is possible with TIMS. Alpha spectroscopy has a long history of use in the detection and isotopic analysis of actinides and can be a simpler and less expensive alternative to mass spectrometer based techniques. The sensitivity and accuracy of both techniques is highly dependent upon the method of sample loading. High quality sample loading is often tedious, time consuming, and expensive. In this work, we sought to simplify and improve high quality sample loading for TIMS in an effort to expand the utility and improve the sensitivity of this technique. During these efforts a promising sample loading method for alpha spectroscopy was developed.

Three improvements were developed for sample loading procedures for isotope ratio measurements of ultra-trace quantities of Pu using (TIMS). Firstly, a new filament geometry, the "dimple", was developed. The bead loading method was used for these analyses. Beads were loaded with New Brunswick Laboratory certified reference material (NBL CRM) Pu128 (^{239}Pu and ^{242}Pu) from an 8M HNO_3 matrix. Overall ion counts and isotopic ratios measured using the dimpled filament geometry were compared to those measured when using the established V-shaped filament geometry. The average number

of Pu counts detected when using dimpled filaments was approximately 34% greater than ion counts detected using V-shaped filaments. The accuracy and precision of isotopic ratio measurements were unaffected by the use of dimpled filaments. The well-like geometry of dimpled filaments aids in sample loading and alignment. Additionally, the use of dimpled filaments was found to reduce sample losses inside the ion source. Over the course of 25 measurements, no sample losses were experienced on dimpled filaments, in contrast to 15% total sample loss experienced with v-shaped filaments.

Secondly, a polymer fiber architecture for TIMS sample loading was developed using similar sample loading procedures as those used in bead loading. Fibers with diameter of approximately 100 μm were prepared from triethylamine-quaternized-poly(vinylbenzyl chloride) cross-linked with diazabicyclo[2.2.2]octane. Total ion counts (^{239}Pu + ^{242}Pu) and isotope ratios obtained from fiber-loaded filaments were compared to those measured bead loading. Fiber loading was found to improve sensitivity, accuracy, and precision of isotope ratio measurements of Pu compared to the established resin bead loading method, while maintaining its simplicity. The average number of detected Pu+ counts was 180% greater and there was a 72% reduction in standard deviation of ratio measurements when using fiber loading. An average deviation of 0.0003 (0.033%) from the certified isotope ratio value of NBL CRM Pu128 was measured when fiber loading versus a deviation of 0.0013 (0.133%) when bead loading. The fiber formation method can be extended to other anion-exchange polymer chemistries, and therefore offers a convenient platform to investigate the efficacy of novel polymer chemistries in sample loading for TIMS.

Thirdly, a sample loading procedure was developed that is based on a polymer thin film architecture. Rhenium filaments were degassed, dip-coated with a thin (~180 nm) hydrophobic base layer of poly(vinylbenzyl chloride) (PVBC), and spotted with an aqueous solution of triethylamine-quaternized-PVBC and a cross-liking agent (diazabicyclo[2.2.2]octane). Spotting resulted in the formation of a toroidal, hydrophilic extractive polymer disk surrounded by the hydrophobic base polymer. Thin film coated filaments were direct loaded with NBL CRM Pu128 from a 9 M HCl matrix. Aqueous sample droplets adhered to the extractive polymer spot, facilitating sample loading. The influence of spot thickness upon ion production was investigated. Overall ion counts and isotopic ratios obtained from thin film coated filaments were compared to those produced by the established resin bead loading method. Isotopic ratios were within error of those measured using the bead loading method with few background interferences. The average number of detected Pu+ counts was 175% greater when using thin film coated filaments with 20-30 μm thick toroidal spots. The use of dimpled filaments further aided sample loading by providing a well-shaped substrate to deposit the sample droplet. No sample loss was experienced with the thin film loading method over the course of 65 sample analyses. Finally, thin films used in this design were found to slow filament aging under atmospheric conditions, facilitating the bulk production of filaments for future analyses.

During this work, an unreported form of rhenium surface oxidation was discovered. Rhenium is the most common ionization filament material for Pu analysis by TIMS. Degassing is a common preparation technique for rhenium filaments and is performed to clean filaments before analysis. Degassing involves resistively heating the

filaments under high vacuum to volatilize and degrade contaminants. Collaborators at Savannah River National Laboratory reported anecdotally that the use of excessively aged filaments (on the order of 2 months of aging in atmosphere after degassing) decreased the sensitivity and precision of TIMS analyses. Although optimization studies regarding degassing conditions have been reported, little work has been done to characterize filament aging after degassing. In this study, the effects of filament aging after degassing were explored to determine a "shelf-life" for degassed rhenium filaments, and methods to limit filament aging were investigated. Zone-refined rhenium filaments were degassed by resistance heating under high vacuum before exposure to ambient atmosphere for up to 2 months. After degassing, the nucleation and preferential growth of oxo-rhenium crystallites on the surface of polycrystalline rhenium filaments was observed by atomic force microscopy and scanning electron microscopy (SEM). Compositional analysis of the crystallites was conducted using SEM-Raman spectroscopy and SEM energy dispersive X-ray spectroscopy, and grain orientation at the metal surface was investigated by electron back-scatter diffraction mapping. Spectra collected by SEM-Raman suggest crystallites are composed primarily of perrhenic acid. The relative extent of growth and crystallite morphology were found to be grain dependent and affected by the dissolution of carbon into filaments during annealing (often referred to as carbonization or carburization). Crystallites were observed to nucleate in region specific modes and grow over time through transfer of material from the surface. The roles of atmospheric humidity and carburization on the oxidation characteristics (i.e. aging) of rhenium filaments were studied. Degassed and carburized

filaments were aged for up to 79 days under dry and humid conditions, and the growth of oxo-rhenium crystallites was investigated intermittently by SEM to construct growth profiles. SEM images were analyzed to determine average crystallite size, number density, and percent surface coverage. Crystallite growth was found to be suppressed by both filament carburization and dry storage conditions (~13% relative humidity). Under humid conditions (75% relative humidity), crystallite growth progressed steadily over the investigatory period, reaching >2.3% surface coverage within 79 days of aging. Atomic ion production of Pu^+ was suppressed by approximately 20% and the standard deviation of isotope ratio measurements was increased by 170% when filaments with 1% oxide surface coverage were used in sample loading. Measurement sensitivity and reproducibility are imperative for applications involving ultra-trace analysis of Pu by TIMS. These findings offer validation for observations regarding the detrimental effect of excessive filament aging post-degassing, improve the understanding of conditions that impel the oxidation of rhenium filaments, and provide practical means to suppress the growth of oxides. PVBC nanolayers were found to slow the growth of oxo-rhenium crystallites on the filament surfaces and may serve as an alternative carbon source for filament carburization.

A novel substrate for the simultaneous concentration of actinides and sample preparation for alpha spectroscopy was developed using thin films originally intended for TIMS sample loading. Substrate preparation involved forming ultrathin films (10-180 nm) of quaternary amine anion-exchange polymers on glass and silicon by dip-coating. Samples were loaded by submerging the polymer-coated substrates into acidified

solutions of Pu or natural water with elevated uranium concentrations. High resolution (25-30 keV) alpha spectra were acquired from these substrates under certain loading conditions indicating that through further development they may be a useful, inexpensive, and potentially field deployable platform serving national security and environmental sampling applications.

DEDICATION

This dissertation is dedicated to my beloved father Mike Mannion and mother Alexis Mannion.

ACKNOWLEDGMENTS

I would like to express my special thanks to my advisor Dr. Scott Husson for his patient support and guidance throughout my graduate studies. Dr. Husson is an excellent mentor and role model. His organizational skills and work ethic are unparalleled, and his sage advice was priceless to the progress of our projects and my growth as a researcher. I greatly enjoyed the time I have spent in his research group and always looked forward to our meetings and discussions. I owe Dr. Husson a great debt of gratitude for helping me to have an outstanding experience as a graduate student.

I would also like to give special thanks my co-advisor Dr. Brian Powell for his guidance and support through my graduate studies. His wisdom, knowledge, insightful advice, and love of learning were crucial to the development of our projects and the growth of my abilities as a researcher. Dr. Powell helped to foster my interests in nuclear related research that I now hope will be part of my professional career. Dr. Powell's friendly smile and attitude always helped to brighten my days.

I would like to thank David Locklair for his collaboration on our projects and his friendship. David performed the research related to Pu uptake and kinetics and aided greatly in our works towards writing a TIMS review article. Without his help our achievements would not have been possible. His knowledge of Pu chemistry and diligent lab work were invaluable to our efforts.

I would like to thank my parents, Mike and Alexis, for their endless support. They were my foundation, and I could not have achieved my academic goals without them. They have always pushed me to do my best, and I thank them for that. I also thank my

wife, Danielle, for her love and patient support through my long nights of writing. Her comfort and encouragement are invaluable to me.

Our collaboration with SRNL was a great experience for me, and I feel very lucky to have been a part of this work. I would like to thank our collaborators Dr. Charles (Chuck) Shick, Jr., Dr. Glenn Fugate, and Dr. Matthew Wellons at SRNL. Chuck was our resident TIMS expert, and without his guidance, patience, and efforts we would have never achieved our goals. Chuck and I had many long conversations in the parking lot of the K-Mart in Greenwood as we exchanged filaments; I have learned a great deal from his openness, insights, and experience. Glenn, now at ORNL, was always willing to discuss our plans and offer new ideas. Without his suggestions and responsiveness the project would not have evolved as it did into the development of a successful product. Matt aided in our SEM investigations of rhenium filaments and performed Raman and SEM-EDS characterization at SRNL. Matt's insights and work were crucial to our rhenium related research, which would not have progressed without his help. I would also like to thank Taghi Darroudi at the Clemson SEM lab. Taghi trained me on the SEM and performed the EBSD characterization of rhenium surfaces. Taghi's patient training and EBSD work were crucial to our efforts. I learned a great amount from Taghi and always appreciated his kind spirit.

I thank my past and current group members Jinxiang, Heather, Steven, Jaime, Christine, Nikki, Mark, Anna, James, AB, and Valery for their help in lab and friendship out of lab. In particular, I would like to thank Valery for keeping me active with our weekly tennis matches.

Finally, I am grateful for the financial support of the TIMS and alpha spectroscopy related work by the National Nuclear Security Administration NA-221 Office of Proliferation Detection under Award No. DE-NA0001735. I am also grateful for the financial support by the South Carolina Universities Research and Education Foundation (SCUREF) under award G-SOW-A-013106 and the Defense Threat Reduction Agency under award HDTRA1-16-1-0016.

TABLE OF CONTENTS

Page

LIST OF TABLES

List of Tables (Continued) Page

LIST OF FIGURES

CHAPTER ONE

INTRODUCTION

1.1 Background information

Mass spectrometry refers to a family of analytical techniques that sort gas phase ions based on their mass-to-charge ratio. These techniques generally are used to determine the chemical or elemental composition of a sample. Mass spectrometers can be broken into three major components: the ion source, the mass analyzer, and the detector(s). Briefly, the sample is introduced into the ion source where gas phase ions are created and accelerated into the mass analyzer using electric potentials. The gas phase ions are then separated in the mass analyzer based on their mass-to-charge ratio. This separation is achieved through the use of magnetic fields. Heavier ions with greater momentum will be deflected less by the magnetic field than lighter ions (assuming equivalent ion charges). After separation, the ions beams are directed onto a detector for counting. Many variations of these three major components have been developed over the last 60 years and mass spectrometers have become cornerstone analytical tools in many fields.

In this work, our objective was to improve ion source performance for thermal ionization mass spectrometric (TIMS) analysis of ultra-trace quantities of Pu and simplify sample loading. TIMS is an older form of mass spectrometry with a relatively simple ion source design. For TIMS, the sample is loaded onto a thin metallic filament that is resistively heated to create thermal ions of the sample. Despite the apparent simplicity of TIMS ion sources, sample loading is often tedious and time consuming, and ionization mechanisms are not well understood. Sample loading methods have been shown to influence the sensitivity of TIMS measurements by several orders of magnitude [3]. Filament additives, sometimes referred to as “ionization

enhancers", are believed to alter the dominant mechanism of ionization from the filament surface [4]. Figure 1.1 graphically illustrates the classic model of thermal ionization and ionization of actinides in the presence of carbonaceous additives. It is believed that carbonaceous additives lead to the creation of carbide intermediates which stabilize the sample on the ionization surface, leading to greater levels of ionization upon decomposition of the carbide [4]. Ionization mechanisms in the presence of filament additives have remained theoretical due to the difficulties of *in situ* measurements of chemistries present on filament surfaces during these analyses due to high filament temperatures (>1200 °C) and high vacuum (~10^{-5} Pa). Research efforts in this area traditionally have been confined to the implementation of new loading methods to increase sensitivity, but fail to truly elucidate the ionization mechanism. Thus, vast improvements may still exist for TIMS.

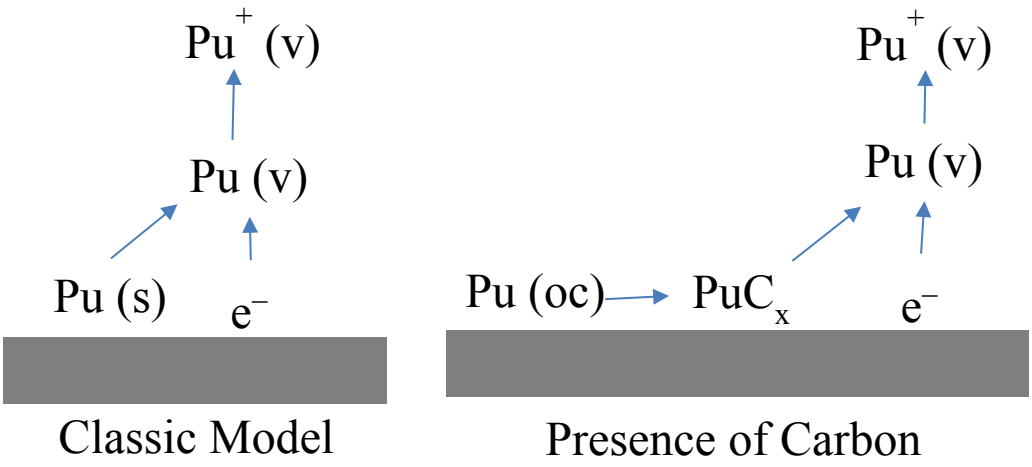

Figure 1.1 Classic model of thermal ionization (left) where the vaporized sample is ionized through interaction with a thermionically emitted electron, and the proposed ionization mechanism for actinides in the presence of carbonaceous filament additives (right).

TIMS is used actively in geo- and cosmochronology [5-7], nuclear safeguards, nuclear forensics, and environmental monitoring [1, 8, 9]. In these efforts, many sample loading procedures have been developed for various analytes. The selection of filament material and filament additives depends on the analyte of interest. Table 1.1 shows a survey of TIMS sample loading conditions for common analytes.

Table 1.1 A survey of sample loading chemistry, filament materials, and measured ions that has been reported in literature for various analytes. Under the category of filament type, (S) refers to a single filament assembly, (D) refers to a double filament assembly, and (T) refers to a triple filament assembly. Multiple filament assemblies can be used to decouple evaporation and ionization processes [1].

Atomic Number	Analyte	Additives	Filament Type	Measured Ion	References
3	Lithium	H_3BO_3	Ta (S), Re (S, D)	$Li_2BO_2^+$	[10-12]
		H_3PO_4	Re (D, T)	Li^+	[13-18]
5	Boron	CsOH	Ta (S)	$Cs_2BO_2^+$	[19]
		Graphite, $CsCO_3$, H_3PO_4 (ionization depressor, suppresses isobarics)[20], mannitol (optional)	Ta (S), Re (S)	$Cs_2BO_2^+$	[20-25]
		Mannitol, graphite, Rb_2CO_3	Ta (S)	$Rb_2BO_2^+$	[26]
		None	Re (S)	BO_2^-	[27]
16	Sulfur	H_3PO_4, Silica Gel, Sample converted to As_2S_3 before loading	Re (S)	AsS^+	[28-30]
17	Chlorine	Graphite (Neutral water matrix, Cs_2Cl)	Ta (S)	Cs_2Cl^+	[31-34]
		$AgNO_3$	Re		[35]
19	Potassium	H_3PO_4, Silica Gel	Ta (S) [aged 1 month	K^+	[36]

			after degassing] [Re (S),(D) and W also investigated]		
20	Calcium	H_3PO_4	Ta (S)	Ca^+	[37]
		Ta_2O_5	Re (S)	Ca^+	[38]
		None	Re (T)	Ca^+	[39]
23	Vanadium	Graphite	Re (S) [carburized with graphite]	V^+	[40]
24	Chromium	Silica Gel, H_3BO_3, Al, (HCl matrix)	Re (S)	Cr^+	[7]
		None* (HNO_3 matrix, $Cr(NO_3)_3*9H_2O$)	Re (D)	Cr^+	[41]
		*Zinc (enriches ionization of light isotopes)	Re (D)	Cr^+	[41]
26	Iron	BaF_2, $AgNO_3$, (HF matrix, FeF_3 form)	Re (D)	FeF_4^-	[42]
		BaF_2, Silver Flouride	Re (D)	FeF_4^-	[43]
		H_3PO_4, Al_2O_3, Silica gel	Re (S)	Fe^+	[44-46]
28	Nickel	H_3PO_4, $AlCl_3$, Fumed Silica, (HNO_3 matrix, $NiNO_3$ form)	Pt (S)-Special Cleaning	Ni^+	[47]
30	Zinc	H_3PO_4, Silica Gel	Re (T)	Zn^+	[48]
32	Germanium	Cellulose Nitrate Adhesive (Ge powder mixed with adhesive)	Re (D)	Ge^+	[49]
37	Rubidium		Re (T)		[50]
38	Strontium	H_3PO_4, TaF_5 (HCl matrix)	Re (S)	Sr^+	[51]
		H_3PO_4 (HCl matrix)	Re (D)	Sr^+	[52]
40	Zirconium	None (HNO_3 matrix)	Re (D)	Zr^+	[53]
42	Molybdenum				
43	Technetium	Collodion, Amyl Acetate, Anion-Exchange Resin Bead	Re (S)	Tc^+	[54]
		La_2O_3, $Ca(NO_3)_2$, NH_4OH	Re (S)	TcO_4^-	[55]
44	Ruthenium				
48	Cadmium				

52	Tellurium	$Ba(OH)_2$, NaOH (HCl matrix)	Re (S), W (S)	Te^-	[56]
55	Cesium	None (HNO_3 matrix)	Re (S, T*)	Cs^+	[57, 58]
60	Neodymium	H_3PO_4 (HCl matrix, $NdCl_3$)	Re (D, T)	Nd^+	[52, 59-63]
		None (HNO_3 matrix, Nd in nitric form)	Re (D)	Nd^+	[64]
62	Samarium	H_3PO_4 (HCl matrix)	Re (D)	Sm^+	[63]
63	Europium	None (HNO_3 matrix)	Re (T)	Eu^+	[65]
74	Tungsten	La_2O_3, Gd_2O_3, O_2 (g)	Re (S) [Ta, Pt also investigated]	WO_3^-	[66]
75	Rhenium		Pt (S), Ta (S)	ReO_4^-	[67]
76	Osmium	$Ba(OH)_2$, Na (optional)	Pt (S)	OsO_3^-	[67]
		La_2O_3	Pt (S)	OsO_3^-	[67]
77	Iridium				
82	Lead	H_3PO_4, Silica Gel/Acid Colloid (HNO_3 matrix for natural samples)	Re (S)	Pb^+	[68-73]
88	Radium				
90	Thorium	H_3PO_4, Graphite	Re (S)	Th^+	[74]
		Graphite (Aquadaq)	Re (S)	Th^+	[75]
		Graphite, Ir	Re (S)	Th^+	[75]
		H_3BO_3	Re (T)	Th^+	[75]
91	Protactinium	Graphite	Re (S)	Pa^+	[76]

In this work, we are concerned with the analysis of Pu by TIMS. Pu contamination is widespread in the environment primarily arising from atmospheric and oceanic nuclear weapons testing [77]. Global fallout contamination is further exacerbated by localized contamination from nuclear weapons production, reprocessing of irradiated fuel, disposal of nuclear waste, commercial nuclear operations, and nuclear accidents such as Chernobyl and those at the Tomsk-Seversk nuclear facility [78, 79]. Although global contamination of Pu is typically at trace levels, the radiotoxicity and persistence of many of its isotopes are of great concern to public health and safety. In addition, the isotopic signature of Pu can reveal the source of the contamination, a critical component in nuclear forensic measurements, health risk assessments, environmental fate

and transport systems, geologic dating, and nuclear safeguard measurements [80]. The isotopic ratio of $^{239}Pu/^{240}Pu$ can differentiate between Pu sources such as global fallout from weapons testing; undetonated weapon grade sources of Pu, spent nuclear fuel, and from failures at commercial nuclear reactors [2]. As such, it is desirable to have validated analytical techniques that can accurately and efficiently quantify the Pu concentration in a sample as well as its isotopic composition. Table 1.2 shows isotopic content of Pu from various sources.

1.2 Methods of Pu analysis

Alpha spectroscopy is commonly used to quantify alpha emitting radionuclides [81]. While this technique is powerful, it does not provide the necessary resolution to readily determine the isotopic $^{239}Pu/^{240}Pu$ ratio due to the small differences in alpha emission energy [82]. Furthermore, even if peak deconstruction is used to resolve the ^{239}Pu and ^{240}Pu alpha peaks, the levels are often so low that the sample must be counted for days to obtain the necessary

Table 1.2 The distribution of Pu isotopes from various sources [2]. Determining the isotopic content of a Pu sample can aid in determination of the sample source.

Pu source	^{238}Pu	^{239}Pu	^{240}Pu	^{241}Pu	^{242}Pu
Global fallout, northern hemisphere (average)		83.5	15	1.2	0.3
Commercial light water reactor: 20 GWd/t burn-up	0.5	73.5	20	5	1
Commercial light water reactor: 30 GWd/t burn-up	1	60	22	13	4
Commercial light water reactor: 60 GWd/t burn-up	4.4	46.3	24.9	12.7	11.7
Chernobyl nuclear accident	0.21	66.2	21.98	4.7	1.2
Weapons grade, <1 GWd/t burn-up	0.04	93.3	6	0.6	0.04
Nagasaki, nuclear explosion 1945		94.5	5.5		

number of counts for statistical purposes [83]. Mass spectrometric techniques are the most powerful analytical tools for ultra-trace isotopic analysis of stable isotopes or radionuclides with long half-lives [2] and can determine the composition of Pu isotopes accurately in trace level environmental samples [1, 8]. TIMS provides one of the lowest detection limits for Pu analysis and is capable of detecting Pu on the femtogram scale [83]. Although inductively coupled plasma-mass spectrometry (ICP-MS) has achieved comparable detection limits for certain elements, it has yet to achieve the detection limit for Pu analysis that TIMS maintains [2]. Additionally, the accuracy of ICP-MS analysis of Pu is hindered by the presence of ^{238}U, which interferes with the measurement of ^{239}Pu by the formation of the isobaric $^{238}UH^{+}$ ion in the plasma source [83]. Finally, as gaseous radioactive fumes are produced during the operation of an ICP-MS, implementation of an ICP-MS requires additional radioprotective measures [8]. Despite these shortcomings, ICP-MS generally is seen as a complimentary method to TIMS and is used routinely for bulk analysis of environmental samples and determination of elemental impurities that provide information related to material origin and processing history [8]. In general, TIMS is used for measurements requiring high sensitivity and accuracy [84]. Accelerator mass spectrometry (AMS) and resonance ionization mass spectrometry (RIMS) have been shown to provide sensitivity for Pu that is comparable to TIMS [2]; however, the usefulness of AMS is limited by expense and lack of available tandem accelerators [83, 85], and no RIMS systems are commercially available [86]. Table 1.3 shows a comparison of reported Pu detection limits for various analytical techniques.

Table 1.3 A comparison of Pu detection limits for various techniques [2]. The detection limit for ICP-MS is reported for a quadrupole system.

Analytical Technique	Pu Detection Limit [g]
α - Spec.	$10^{-11} – 10^{-13}$
ICP - MS	10^{-11}
RIMS	$10^{-15} – 10^{-16}$
AMS	$10^{-15} – 10^{-17}$
TIMS	$10^{-15} – 10^{-17}$

1.3 TIMS sample loading methods for Pu

1.3.1 Direct loading

TIMS often is selected as an analytical tool due to a need for high levels of sensitivity. Since sample loading methods effect the sensitivity of TIMS measurements, optimization of these methods has been the subject of many investigations. Direct loading is the simplest but most primitive form of sample loading. In direct loading, a small volume (0.5-2 μL) is deposited directly onto a degassed filament with the use of a micropipette and allowed dry. Drying may be expedited using a heat lamp or by resistively heating the filament [3]. Total efficiencies (atoms loaded to atoms detected) are typically less than 0.1% for direct loading [2], providing an experimental detection limit for ^{239}Pu of approximately 10^{11} atoms [3]. Direct loading onto a freshly degassed filament often causes the solution to spread across the filament. This outcome is undesirable as it causes spreading in the resulting ion beam during operation and a lower throughput of ions into the spectrometer. Anecdotal evidence suggests that freshly degassed filaments should be allowed to sit for several weeks (when direct loading onto bare filaments) to allow for a small degree of oxidation to occur on the rhenium surface. The ingrowth of rhenium oxide helps to keep the solution stationary and not spread across the filament. Direct loading

commonly is used when a large amount of sample is available [87]. Trace level samples require lengthier operation times and alternative loading techniques to obtain reliable data.

1.3.2 Electrodeposition

Electrodeposition of an analyte directly onto a metallic substrate has been used extensively in alpha spectroscopy analyses as it can be performed on many different ions [88]. Electrodeposition produces a thin, uniform layer of analyte, which is essential for making high resolution measurements. Electrodeposition also has been used in TIMS analyses; however, not nearly as universally as the other loading methods. A variety of parameters such as current, time, temperature, solution volume, distance between electrodes, pH, buffering solution, and electrolyte concentration will affect the quality and yield of the samples and so these parameters must be chosen carefully depending upon the analyte of interest. When optimized, deposition yields generally exceed 85% for actinides from purified samples [88-94]. Since optimization varies depending upon the analyte, extensive sample purification is often necessary to produce high yields and a quality spectrum free of interferences. Purification is especially important for environmental samples that contain a host of ions and organic matter which must be removed prior to deposition. Small concentrations of organic carbon drastically reduce deposition yields, and thus wet-ashing with nitric acid is a necessary step for environmental samples to remove organics [92].

Electrodeposition provides slightly higher ionization efficiencies than the direct loading method and aids in further purification from the sample matrix, especially for ions such as Na and K that are often difficult to remove [89]. The addition of an overcoat of Re or Pt further increases ionization efficiency and reduces the effect of isotopic fractionation [2, 84]. The addition of an overcoat is performed as a subsequent electrodeposition step, as sputtering of the

metal to form the overcoat often exhibits poor reproducibility in thickness and consequently poor reproducibility in the measurement [89].

U, Pu, and other actinides are deposited most commonly from a buffered ammonium sulfate solution (Talvitie method), although ammonium chloride, ammonium oxalate, and dimethylsulfoxide have been used [89-92, 94, 95]. In the Talvitie method, electrodeposition takes place from a 0.5-1.0 M ammonium sulfate solution that is adjusted to pH 2.0-2.3 [95]. Concentrated base (typically NH_4OH) is used to adjust the pH prior to deposition. The addition of concentrated base can cause localized areas of increased pH prior to thorough mixing, which can induce hydrolysis or polymerization of Pu, resulting in reduced yields. To combat this problem during Pu deposition, a small amount (<0.01 M) of chelating agent such as ethylene diamine tetraacetic acid (EDTA), diethyl triamino pentaacetic acid (DTPA), or nitrile triacetic acid (NTA) may be added to prevent these undesirable reactions [91, 95].

1.3.3 Bead loading

Ion-exchange resin bead loading has long been used in TIMS as it reproducibly provides one of the highest ionization efficiencies and produces a stable ion beam [4, 84]. This sample loading technique was the model system for our investigations and is discussed extensively in chapter 2, so the details of this method will not be introduced here.

1.3.4 Micro porous ion emitter

The micro porous ion emitter (PIE) has been developed recently to take advantage of the multitude of advancements for increased ionization efficiency in TIMS operation while maintaining good reproducibility in the measurement. The PIE consists of a 50/50 (w/w) mixture of rhenium and platinum powders combined with hot binder glue. The mixture is drawn into a syringe and extruded into a small diameter rope and allowed to cool. Prior to its use, the cooled

extruded mixture is cut with a scalpel into ~100 µm thick slices and positioned in the center of a rhenium filament. The PIE is initially attached to the filament by heating to 150 ˚C for 1 minute in a convection oven. A subsequent heat treatment is performed by heating the filaments with the attached PIE under vacuum to 1900 ˚C over a span of 15 minutes. Once the temperature is reached it is held at this temperature for 20 minutes to volatilize the binder glue and to melt the platinum (MP = 1768 ˚C). The melted platinum alloys with the rhenium and sinters the PIE to the filament. After the heat treatment, a highly porous matrix sintered to the rhenium filament is available for use in TIMS analyses. To provide sites for analyte binding, an ion-exchange polymer is wicked into the porous structure and allowed to dry. Often it is necessary to dilute the ion-exchange polymer to reduce its viscosity. The reduction in viscosity allows for appropriate capillary action to wick the polymer into the structure. Once the polymer is dried, the analyte is wicked into the PIE and allowed to dry. The sample is then ready for analysis.

The PIE pore size was determined to be a function of the Re powder since the Pt powder melts and alloys with the Re during preparation of the PIE. It was discovered that the smallest mesh Re powder produced a more compact PIE, and that the sample utilization efficiency was higher and more reproducible under these conditions [84]. The highly porous structure brings the analyte into closer contact with the metal allowing for more interactions between the volatilized element of interest and the hot metal surface of the PIE, increasing the chances of ionization as the gaseous analyte moves out of the PIE framework. The sintering of the PIE to the filament assures the matrix will not move or become dislodged from the filament during operation as sometimes occurs with the bead loading method. Additionally, the work function of Pt (5.65 eV) is higher than rhenium (4.96 eV) or rhenium carbide (5.25-5.36 eV), which is advantageous for increased formation of ions [84, 96, 97].

Early investigation by Delmore showed the PIE outperformed the bead loading method for uranium analyses [96]. Analyses with PIEs resulted in 2% ionization efficiency on average, a factor of 4 increase over that obtained from analyses of resin beads amended with uranium [2, 84, 96]; however, the ionization efficiency was not improved for Pu analysis. On average, Pu sample utilization efficiency was only 0.8% with the PIE, lower than the average of 1.2% with the bead loading method [96]. This outcome was perplexing as the ionization potential for Pu (6.06 eV) is lower than that of U (6.19 eV), and, therefore, Pu should undergo ion formation more readily. By varying the soaking times of the resin beads (in Pu bearing 8 M HNO_3) it was found that longer soaking times increased the ionization efficiency. It was hypothesized that the longer soaking times allowed the analyte to diffuse further into the bead structure, which aided in carbide formation upon pyrolysis of the resin bead. This hypothesis was tested by exploring the relative ionization efficiencies of praseodymium and lutetium. These two lanthanide elements were chosen due to their similar ionization potentials (5.464 eV for praseodymium and 5.426 eV for lutetium) but large mass difference within the lanthanide elements. When the sample preparation method for converting the analyte to the carbide was varied, the ion intensity for lutetium varied by up to two orders of magnitude, while the ion intensity for praseodymium remained essentially constant [96]. The variation in sample utilization efficiency between the elements was attributed to the ease with which the analyte underwent carbide formation (which is believed to increase ionization efficiency as will be discussed in chapter 2). It was discovered that praseodymium formed anionic nitrate complexes; whereas lutetium did not, and so only praseodymium would chemically associate with the anion-exchange polymer within the PIE. This interesting observation led to the conclusion that the analyte needs to be associated with the carbon matrix to efficiently convert the analyte to the carbide [96]. Unfortunately, funding for

PIE research ran out before this hypothesis could be tested. Research into the PIE design has since been continued at Los Alamos National Laboratory with additional funding.

1.4 Isotope dilution

Frequently in TIMS analyses the isotope of interest is present with a concentration near the detection limit of the instrument. This makes quantification difficult, if not impossible, and adds considerable uncertainty. The technique of isotope dilution often is used in these cases to increase the detector signal through the addition of a well characterized sample. A spike of known isotopic composition and concentration (often a certified reference material) is added to the sample and allowed to equilibrate. After equilibration, the "new" isotope ratio (spike + natural sample) is measured by mass spectrometry. Deviation from the certified isotope ratio of the spike solution is attributed to the isotopic composition of the sample [98]. When performed properly, isotope dilution can provide precise measurements with a relative standard deviation of <0.1% for minor isotopes and <0.05% for major isotopes [80, 98].

1.5 Dissertation structure

In this dissertation, I report work towards improving sample loading of Pu for analysis by TIMS and alpha spectroscopy. Chapter 2 discusses the evolution of a thin film loading strategy for TIMS. Chapter 3 discusses our discovery of an unreported form of rhenium surface oxidation and the effect of rhenium filament oxidation on TIMS analyses. Chapter 4 discusses the use of ultra-thin films for simultaneous concentration of radionuclides and sample preparation for alpha spectroscopy. Chapter 5 discusses our conclusions and my recommendations for future investigations.

CHAPTER TWO

DEVELOPMENT OF IMPROVED SAMPLE LOADING TECHNIQUES FOR THERMAL IONIZATION MASS SPECTROMETRY

2.1 Introduction

Thermal ionization mass spectrometry (TIMS) with isotope dilution is recognized internationally as the gold standard for obtaining isotopic ratios and mass amounts of Pu [1]. Isotopic analysis of ultra-trace quantities of Pu is possible by TIMS [83, 99], a technique that remains important in the fields of nuclear safeguards [8], nuclear forensics [100], and environmental monitoring [101]. TIMS analysis, while expensive and time consuming, is used for analyses requiring high levels of sensitivity and accuracy [84]. Sample preparation techniques have a large influence on Pu detection limits by TIMS (direct loading $\approx 10^{11}$ atoms; electroplating $\approx 10^{10}$ atoms; resin bead loading $\approx 10^{7}$ atoms) [3] and, in some cases, contribute significantly to the time investment associated with analysis [80].

Use of carbon-based additives in sample preparation methods for the thermal ionization of actinides dates back to at least the 1960s, when carbon addition was identified as a means to suppress sample oxidation in early vacuum systems [102]. Since this early development, methods of carbon incorporation have evolved and carbon-based additives are believed to provide at least three additional benefits to sample utilization:

1) Carbonaceous additives promote the formation of Pu-carbides [103]. The conversion of Pu to the carbide form is believed to stabilize the sample against thermal ionization, resulting in ionization occurring at elevated temperatures [4]. As described by the Saha-Langmuir equation

(equation 2.1) [104], when the difference between the work function of a surface and the ionization energy of the deposited sample is negative (rhenium work function ≈ 4.7 eV [105]; Pu first ionization = 6.06 eV [96]), thermal ionization efficiency is positively related to the temperature of ionization; therefore, ion production occurring at elevated temperatures vis-à-vis Pu carbide formation results in increased ionization efficiency.

$$\frac{n_+}{n_0} = \frac{g_+}{g_0} e^{\frac{W-I}{kT}} \quad (2.1)$$

n_+/n_0 is ionization efficiency, g_+/g_0 is the ratio of statistical weights of the ionic and atomic states, W is the work function of the ionization surface, I is the ionization energy of the sample, T is the temperature of ionization, and k is the Boltzmann constant.

2) “Carburization” or “carbonation” of rhenium filaments provides a more favorable surface for sample ionization to occur[106]. In thermal ionization processes, the work function of an ionization surface is related exponentially to ionization efficiency (equation 2.1); therefore, high work function materials are desired in the construction of TIMS ionization filaments (for the production of positive ions, referred to as P-TIMS). Rhenium is a preferred filament material for TIMS analysis of Pu, in part to its high work function [107], which can be increased further through carbon dissolution at high temperatures (>1500°C)[108]. Modern carburization processes often involve exposing rhenium filaments, under vacuum, to volatile organic compounds while restively heating the filaments [106, 109]. This process is estimated to increase the average work function of polycrystalline rhenium by ~0.4 eV [110]. Localized filament carburization also may occur with methods such as “bead loading”, where small (40–200 μm) polymer beads are affixed directly upon rhenium ionization filaments [111]. Other carbonaceous additives, such as collodion, aquadag, and graphite, which are applied directly to the filament

before analysis, have been tested for use in Pu analysis by TIMS[106] and will contribute to filament carburization when heated[112].

3) Extractive polymeric materials, such as anion-exchange resin beads, are capable of concentrating the sample into a geometrically small region on the ionization surface, producing a narrower ion beam [111]. This aides in ion-beam focusing, resulting in increased ion transmission into the mass spectrometer [84]. Bead loading, involving extraction of Pu on a small exchange resin beads [113], has shown improved ionization efficiency in comparison to more dispersed means of sample loading, such as electrodeposition and simple direct loading [3]. Anion-exchange resins often are used in the cases of Pu sample loading, as Pu readily forms an anionic complex in concentrated nitric [114] and hydrochloric acid [115].

Various filament materials have been reported in the literature for use in TIMS systems, and rhenium has been the preferred material in the low-level analysis of Pu [2]. Platinum has a higher work function than rhenium, but its melting point is close to ionization temperatures for Pu. Tungsten has better thermal properties than rhenium, but a lower work function. Efforts have been made to utilize platinum, due to its high work function, in platinum/rhenium composite filaments [9] and porous ion emitters [84]. Composite filaments were prepared by electroplating platinum over a loaded rhenium filament (with the Pu sample first loaded onto the rhenium filament by electroplating), and porous ion emitters include platinum in a dispersion with rhenium, which is sintered onto rhenium filaments forming a porous bimetallic structure [85]. Other metallic additives, such as gold and silver, also have been tested as coating materials [116].

Ion source geometries other than flat ribbon filaments have been studied in efforts to increase ion yields and focus ions emitted from the ion source. Modified filament designs have aimed at increasing contact, or the number of interactions, between the sample atoms and the ionization surface. In TIMS analysis of Pu, the majority of the loaded sample is emitted from the filament as neutral gas atoms (ionization efficiency: direct loading ≈ 0.01 - 0.1%; resin bead loading ≈ 0.1 – 1.0%) [2]. By loading the sample in a concave ionization source, neutral gas atoms emitted from the initial point of loading have opportunities to interact with the ionization surface multiple times. In one design, the cavity source, high ionization efficiencies (~10%) relative to other methods were achieved by loading the Pu sample into the back of a capped rhenium tube heated by an electron gun [117]. It is theorized that neutral gas atoms produced at the closed end of the tube will scatter along the inside of the tube, thus having multiple opportunities to collide with the tube surface and become ionized. Porous ion emitter designs have emulated this concept by creating micro-porous rhenium structures on electrically heated filaments [84]. Other ion source geometries include the "boat" or V-shaped filament, where rhenium ribbon is crimped into a trough shape. V-shaped filaments have been shown to increase ion focusing [118] and aid in sample loading [106].

The goals for this work were to simplify sample loading for TIMS analysis of Pu while retaining the sensitivity afforded by the established bead loading method and eliminate sample loss often experienced with the bead loading method (up to 25% in some cases [84]). Aggarwal *et al.* recently reported a membrane-based method of sample loading utilizing phosphate-bearing extractant polymers [119]. Two methods of membrane loading are reported by Aggarwal *et al.*: 1) membrane sections were submerged in sample-bearing solution before washing and being placed onto filaments; and 2) membrane sections were loaded in solution, washed, then held in

contact with the filament by hand while slowly heating the filament, melting and depositing the sample bearing polymer onto the filament. Although novel, these loading methods result in a more dispersed ion production region and lower sensitivity than in the case of bead loading. Additionally, membrane sections must carefully be manipulated by hand after exposure to radioisotopes, a challenge shared with the bead loading method. In this work, we sought to develop a filament pre-coating that retains the measurement sensitivity and accuracy afforded by the bead-loading method while also making direct loading by pipette possible, eliminating the need to directly handle and position radioisotope bearing anion-exchange material.

It was hypothesized that the introduction of a thin film of an extraction medium directly onto the rhenium ribbon would facilitate sample loading and eliminate sample loss due to explosive decompression. Explosive decompression of anion-exchange resin beads during heating (due to entrapped water) has been proposed as a possible mechanism by which high sample losses occur with the bead loading method. It was theorized that thin films would be better suited to releasing entrapped gasses than highly cross-linked resin beads. Additionally, the planar geometry of the thin film will ensure close proximity of the sample to the filament surface, potentially increasing the efficiency of the sample ionization as more of the sample may interact with the ionization surface. Furthermore, application of a thin film extractant would allow the use of alternative rhenium ribbon physical geometries that will increase the ionization of the neutral gas phase Pu atoms. An increase in either evaporation or ionization can increase the sensitivity of TIMS analysis.

In work by Smith et al. [111], it was shown that a graphitic, actinide-bearing residue remains on filaments after heating beads, indicating that incomplete dissolution of the anion-exchange material into rhenium filaments occurs in the case of bead loading. Carbon is

understood to be soluble in rhenium at elevated temperatures [108]. It was hypothesized within our group that more complete dissolution of anion-exchange material, and thus sample transport to the ionization surface, could be achieved with a thin film design through optimization of film thickness. One reason for selecting an ion-exchange polymer is that Delmore [96] hypothesized, after work on the micro ion source program at Idaho National Laboratory, that the sample species must react chemically with carbon additives to effectively be converted to the carbide form. A quaternary amine-bearing polymer was selected for Pu loading due to a history of use in radiochemistry[120] and because the bead loading methodology uses Q-type resin beads [113]. This chapter details the evolution of work on polymer thin-film coatings in the development of improved sample loading strategies for TIMS analysis of Pu.

2.2 Experimental

2.2.1 Materials

The following materials were used as received from Sigma-Aldrich: chloroform (Reagent Plus® ≥ 99.8% with 0.5-1.0% ethanol as stabilizer, CAS# 67-66-3); 1,4-diazabicyclo[2.2.2]octane (DABCO), (Reagent Plus® ≥99%, CAS# 280-57-9); hydrogen peroxide solution containing inhibitor (30 wt% in water, CAS# 7722-84-1); poly(vinylbenzyl chloride) (PVBC), (60/40 mixture of 3- and 4- isomers CAS# 121961-20-4); and sulfuric acid (95-98%, ACS reagent grade, CAS# 7664-93-9). NaCl (reagent grade) was obtained from VWR, and $NaNO_3$ and $NaNO_2$ (reagent grade) were obtained from Mallinckrodt.

Hydrochloric acid (Optima® grade for ultra-trace elemental analysis, CAS# 7647-01-0, 7732-18-5), nitric acid (Optima® grade for ultra-trace elemental analysis, CAS# 7697-37-2, 7732-18-5) and triethylamine (TEA, 99%, reagent grade, CAS# 121-44-8) were used as received from Fisher Scientific.

Silicon substrates were acquired from Nova Electronic Materials as 4" N/Ph <100> 1-10 Ohm-CM 500-550 μm thick SSP prime grade Si wafers diced to 1 cm × 3 cm pieces. Soda-lime glass capillaries (5 ± 0.05 μL type II glass) were acquired from Kimble Glass, Inc. Anion-exchange resin beads were obtained from Bio-Rad (AG® 1-X2 Anion-exchange Resin, analytical grade, 50–100 mesh, chloride form). Collodion solution (flexible, CAS# 60-29-7, 9004-70-0, 8001-79-4, 76-22-2, 64-17-5) was acquired from J.T. Baker. Rhenium ribbons (0.76 mm W × 0.03 mm H) and wafers (1 cm × 3 cm × 0.1 cm) were made of zone-refined rhenium (minimum of 4-pass zone refined; 99.999% Re) from H. Cross Company.

Pu solutions for TIMS measurements were prepared from a dilution of a primary standard containing New Brunswick Laboratory (NBL) certified reference material (CRM) 128 with a

certified $^{239}Pu/^{242}Pu$ atom ratio of 0.99937 ± 0.00026 (determined October 1, 1984) at Savannah River National Laboratory (SRNL). Based on the half-lives of ^{239}Pu and ^{242}Pu, the approximated $^{239}Pu/^{242}Pu$ ratio would be 0.9985 on October 1, 2017. The decay corrected $^{239}Pu/^{242}Pu$ ratio (October 1, 2017) was used for calculating the deviation of measured ratios from the certified value. Two sources of Pu were used at Clemson University for uptake and kinetic experiments. A ^{238}Pu source was obtained from Eckert and Zeigler Isotope Products (Valencia, CA), and, for higher Pu mass loading experiments, certified reference material 130 (CRM 130) from New Brunswick Laboratory containing >99% ^{242}Pu by mass was used. Pu solutions at Clemson University were prepared using ultrapure deionized (DI) water from an Elga Purelab Flex system.

DI water with a resistance of 18.2 MΩ prepared from distilled water that was passed through a Milli-Q water purification system (EMD-Millipore) was used for polymer preparation and deposition.

2.2.2 Construction and degassing of rhenium ionization filament assemblies

Degassing was performed prior to sample loading to clean filaments. Briefly, by heating filaments to high temperatures under vacuum, contaminates such as uranium and halogens can be driven from the filaments, thereby reducing measurement interferences. Rhenium strips (0.76 × 0.03 × 15.9 mm) were cut and spot-welded onto posts for electrical heating at SRNL where the TIMS system and degassing chamber reside. After mounting, filaments were crimped into either standard V-shapes, described elsewhere [118, 121] and commonly used at SRNL, or a novel filament geometry, referred to as the “dimpled” geometry, that was developed for this work. Figure 2.1 shows an image of V-shaped and dimpled filaments. After crimping, filament

degassing was performed in a vacuum chamber at a pressure of around 10^{-5} Pa. Each sample filament was heated incrementally from 0.5 Amps to 3.0 Amps using 0.5 Amp increments lasting 15 min each with 15 min cooling periods at 0 Amps between each step. Filaments were held at 3.0 Amps for a total time of 45 min, consisting of three 15 min heating periods and two intermittent 15 min cooling periods at 0 Amps. After the heating/cooling cycles were completed, the filaments were allowed to cool under vacuum at 0 Amps for at least 2 h before removing from the degassing chamber. Pyrometry was used to approximate filament temperatures at the conditions used for degassing. Three Amps of filament current was found to correspond to a filament temperature of approximately 1460 °C. Rhenium filament oxidation arising from atmospheric exposure has been shown to negatively impact the ionization efficiency and the precision of isotope ratio measurements of Pu [122], therefore, all filaments were used for analysis within 1 week of degassing when no filament coating was applied. In cases where polymer coating was applied to degassed filaments (vide infra), the coatings were deposited within 1 week of degassing, unless this was logistically impossible.

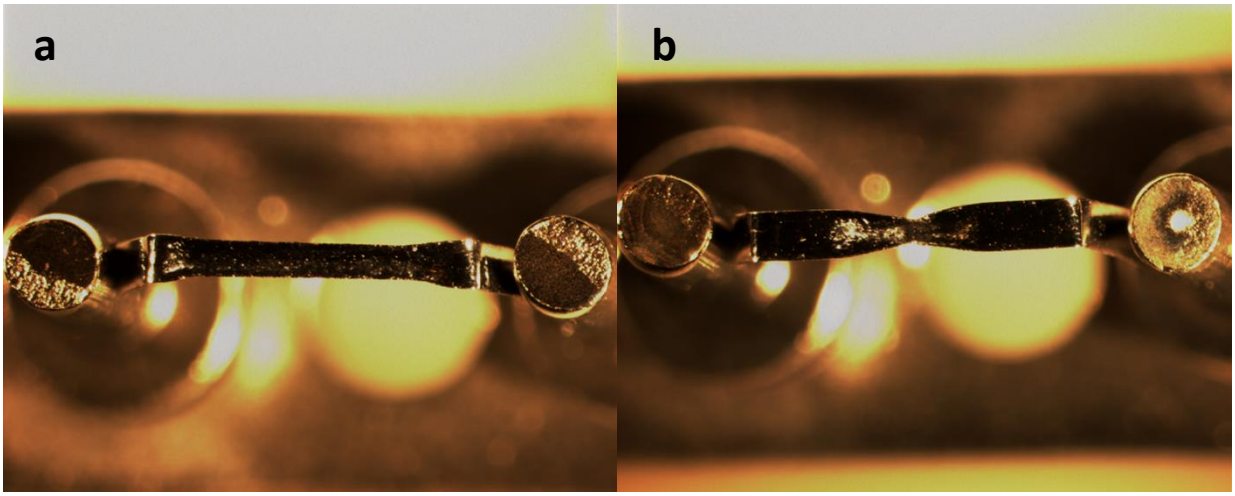

Figure 2.1 a) Traditional "boat" or V-shaped filament design and b) dimpled filament design presented in this work.

2.2.3 Silicon and glass substrate preparation for polymer coating

Silicon substrates (1 cm × 3 cm) were removed from their adhesive backing and etched with sample numbers. Glass substrates were prepared by cutting standard borosilicate glass slides into approximately 2.5 cm × 2.5 cm squares. Piranha wash solution was prepared by slowly adding 1 part 30 wt% hydrogen peroxide to 3 parts concentrated sulfuric acid. (Caution: To prepare this solution, hydrogen peroxide was poured slowly into the concentrated sulfuric acid under a hood. Piranha solution is a very strong oxidant that may react violently if it comes in contact with organics.) Substrates were cleaned first by sonication (Aquasonic 75HT, VWR Scientific) with DI water for 15 min. Next, each substrate was placed in either a test-tube with 10 mL of piranha solution (silicon substrates) or a 100 mL glass jar with 30 mL of piranha solution (glass substrates) and heated in a water bath to 85°C for 1 h. The used piranha solution was collected for safe disposal, and each test tube with substrate was washed with DI water 3 times before 15 min of sonication in DI water. The substrates were washed a final time with DI water and dried with compressed nitrogen.

2.2.4 Polymer film formation by dip-coating

After degassing (in the case of rhenium filaments) or piranha washing (in the case of silicon or glass), substrates were dip-coated from solutions of PVBC in chloroform with and without the addition of a cross-linker. The thickness of films produced by dip-coating depends on solution properties, such as density and viscosity, as well as processing parameters, such as the withdrawal rate[123]. To produce a film with a thickness of approximately 120 nm, the substrate was withdrawn from a 2 wt% PVBC solution at a withdrawal rate of 340 mm/min using a Qualtecs Product Industry QPI-128 dip coater. Figure 2.2 shows the relationship between

withdrawal rate and film thickness for different solution polymer concentrations. When preparing cross-linked films, DABCO was spiked into the solution immediately before dip-coating to serve as a cross-linker. The molar amount of DABCO added was limited by stoichiometry based on a 1:2 reaction of DABCO to benzyl chloride sites along the PVBC chains. A ratio of 18.4 mg DABCO:1 g PVBC was used to prepare films with approximately 5% cross-linking. Approximately 10 min after dip-coating, filaments were placed in an 80°C oven for 24 h to accelerate cross-linking of the films. A 5% degree of cross-linking was determined to be the minimum level of cross-linking to prevent film dissolution in chloroform after baking for 24 h at 80 °C. Films with 0.5, 1.0, and 2.5% cross-linking also were prepared in this manner but were not used in any other experimentation. Film thicknesses were determined with multi-angle ellipsometry (described in section 2.2.10). Figure 2.3 shows a graphical representation of the dip-coating process and the chemicals involved. In some cases, DABCO addition to the dip-coating solution was excluded from this procedure to prepare non-cross-linked PVBC films. PVBC films with no cross-linking were prepared to determine the influence of DABCO cross-linking on acid stability and Pu uptake.

2.2.5 PVBC-DABCO film quaternization process

PVBC films cross-linked with DABCO were cast on silicon, glass, and rhenium substrates by dip-coating and then submerged in neat TEA or a 5 wt% TEA solution in chloroform at room temperature for 48 h to produce quaternary amine functional groups. Figure 2.4 depicts the reaction between TEA and PVBC. After exposure to TEA, films were removed from solution with tweezers and lightly blown dry with a nitrogen gun connected to a compressed nitrogen cylinder (regulator pressure of 69–103 kPa). Film thicknesses were

measured before and after quaternization by multi-angle ellipsometry, described in section 2.2.10.

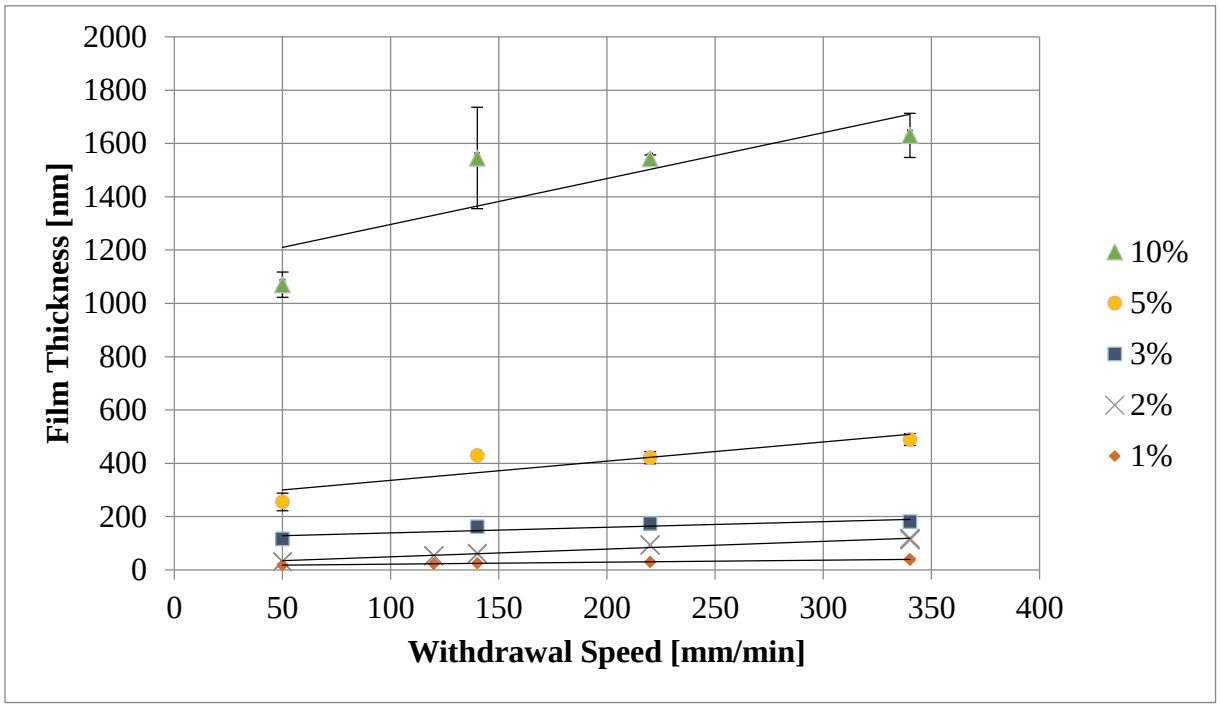

Figure 2.2 Thickness measurements for PVBC-DABCO films formed by dip-coating from chloroform solutions. Percentages in the legend indicate weight percent PVBC in chloroform. Directly prior to dip-coating, a solution of DABCO in chloroform was added to the polymer solution resulting in a 5% cross-linked film based on stoichiometric amounts of DABCO relative to benzyl chloride groups (1:2 reaction). Error bars represent ± 1 standard deviation based on a minimum of 5 measurements.

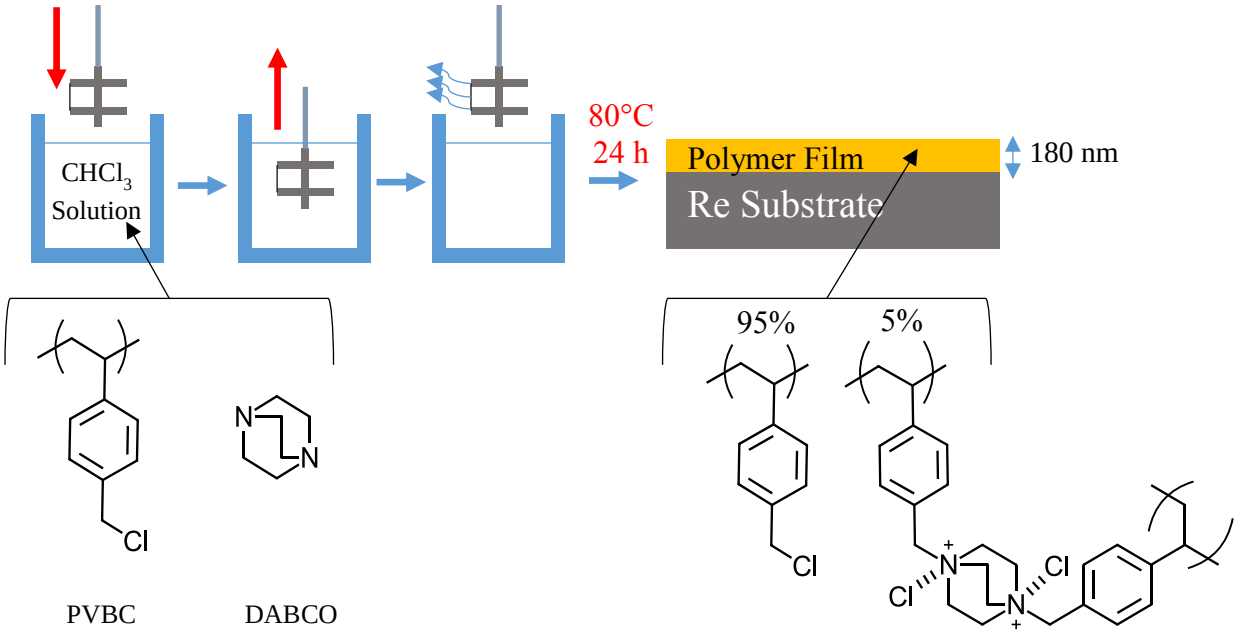

Figure 2.3 Dip-coating procedure and resulting film chemistry (PVBC-DABCO cross-linked film). A rhenium filament is represented in this illustration but the procedure also was applied to silicon and glass substrates.

2.2.6 Formation of localized quaternary amine functionalization within thin films of DABCO cross-linked PVBC

A method was developed using capillaries to create localized regions of TEA quaternization within PVBC-DABCO films. Figure 2.4 shows the chemicals involved and the synthetic design. Jigs were constructed from aluminum stock to hold and align capillaries filled with a mixture of TEA and chloroform in perpendicular contact with PVBC-DABCO films. After coating with a PVBC-DABCO film, rhenium filaments and silicon wafers were mounted into the jigs and then placed into a jar containing a reservoir of chloroform (Figure 2.5). The jar was sealed and a capillary was threaded through a hole in the lid of the jar and then through holes drilled in the jig, aiding in the alignment of the capillary on the substrate surface. Once in

place, the capillary was lifted slightly off the surface of the ribbon, and filled with approximately 2 μL of 5 wt% TEA in chloroform. Once filled, the capillary was lowered slowly to the polymer film coated substrate. The capillary was positioned such that the glass was not in direct contact with the film, as this would often damage the film, but close enough that a fluid bridge would form between the end of the capillary and the polymer coated substrate. The TEA solution diffused out of the capillary over the course of 3-4 h to produce a small hydrophilic spot of TEA quaternized PVBC-DABCO within the polymer matrix. Capillaries were refilled to produce spots with larger diameter. Contact times ranged from 4 to 24 h, with 24 h contact time requiring the capillary to be refilled approximately 7 times. This method was used to modify both PVBC-DABCO coated rhenium filaments and silicon wafers.

2.2.7 Polymer preparation for small toroidal polymer spots

A 10 wt% solution of PVBC in chloroform was prepared and 0.33 g TEA/g PVBC was added while stirring the solution magnetically. This solution was stirred continuously for approximately 48 h until TEA-quaternized PVBC separated as a viscous polymer-rich phase. The excess chloroform was decanted from the viscous polymer-rich liquid phase and discarded. The polymer-rich liquid phase was dried under vacuum (~85 kPa vacuum) for 48 h before being ground with a glass stir rod inside the scintillation vial used to perform the quaternization reaction and placed under vacuum for an additional 24 h. TEA-quaternized PVBC modified in this manner is water soluble. Assuming ideal conversion, 0.33 g TEA/g PVBC results in approximately 50% conversion of chlorobenzyl groups to quaternary amine sites.

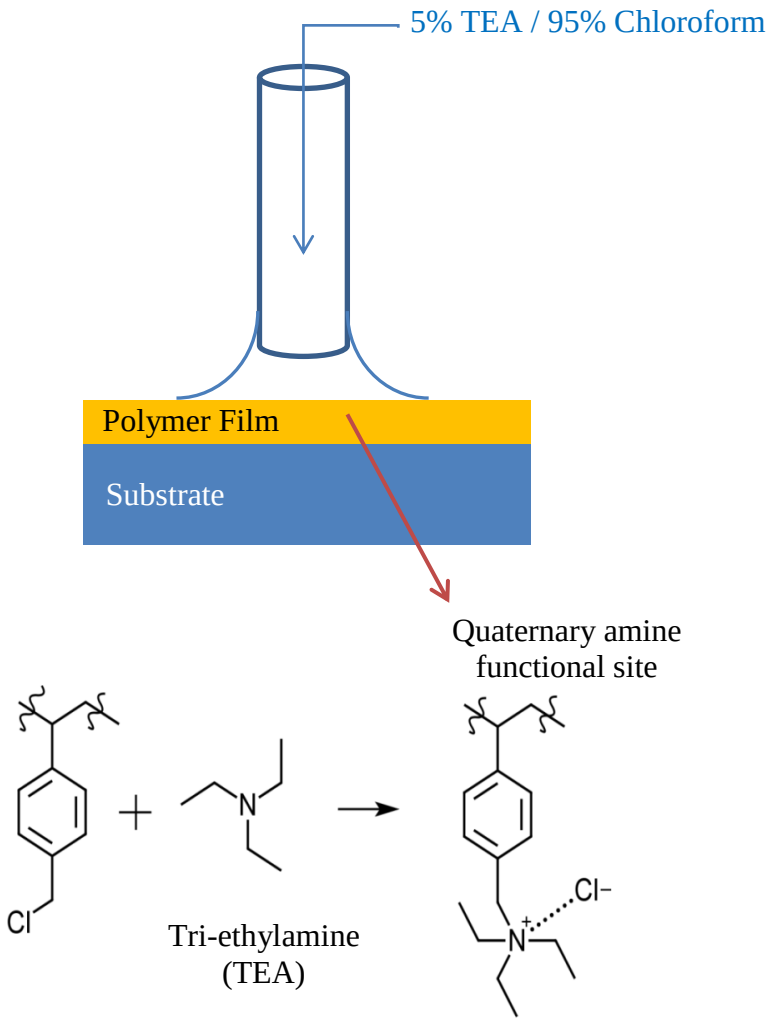

Figure 2.4 Synthetic methods developed to produce chemically stable films with small quaternary amine functionalized spots.

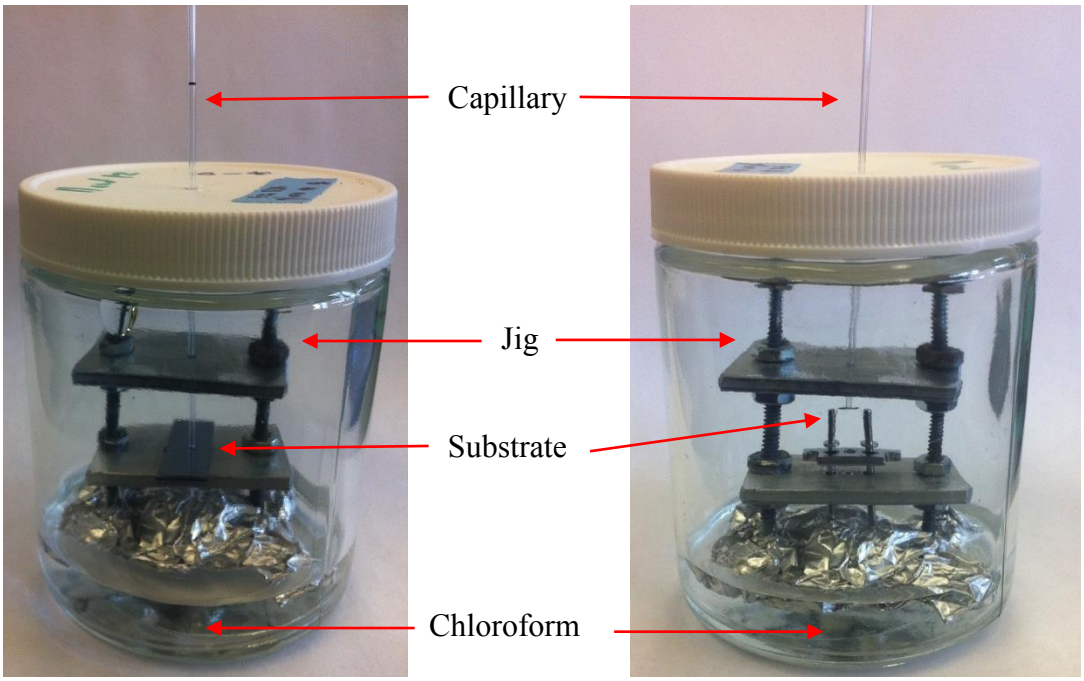

Figure 2.5 Equipment used to create localized quaternary amine functionalization on PVBC-DABCO coated substrates (left: silicon substrate, right: rhenium filament assembly) inside 500 mL glass jars.

2.2.8 Toroidal polymer spot formation using the "needle method"

Solutions from 0.5 to 15.0 wt% TEA-quaternized PVBC in deionized water were prepared alongside solutions of DABCO (0.275 g DABCO/g quaternized PVBC) in DI water. The TEA-quaternized PVBC and DABCO solutions were mixed for approximately 1 min immediately prior to spotting. Small spots were formed on PVBC-DABCO coated filaments and silicon wafers by the "needle method" (illustrated graphically in figure 2.6), which deposited a small droplet of the solution onto the PVBC-DABCO films. Based on the dimensions of deposited polymer spot (determined by 3-dimensional scanning electron microscopy and atomic force microscopy; described in sections 2.2.12 and 2.2.13), droplets formed by the needle method are approximately 5–50 nL in volume. Spotted substrates were allowed to dry for 20 min

at room temperature before being placed into an 80°C oven for 24 h to accelerate cross-linking both within the deposited polymer spot and between singly bound DABCO within the polymer spot and chlorobenzyl groups of the PVBC-DABCO film. Cross-linking within polymer spots prevents dissolution of the quaternized PVBC spots in aqueous Pu loading solutions, and cross-linking between singly bound DABCO within the polymer spot and the PVBC-DABCO film anchors the spots to the substrate, preventing spot detachment when it is swollen by contact with aqueous solutions. Figure 2.6 shows a graphical illustration of the chemistry and dimensions of deposited polymer spots. Spot thickness was controlled by manipulating the concentration of polymer in the spotting solution, and spot diameter was manipulated by controlling deposited droplet volume.

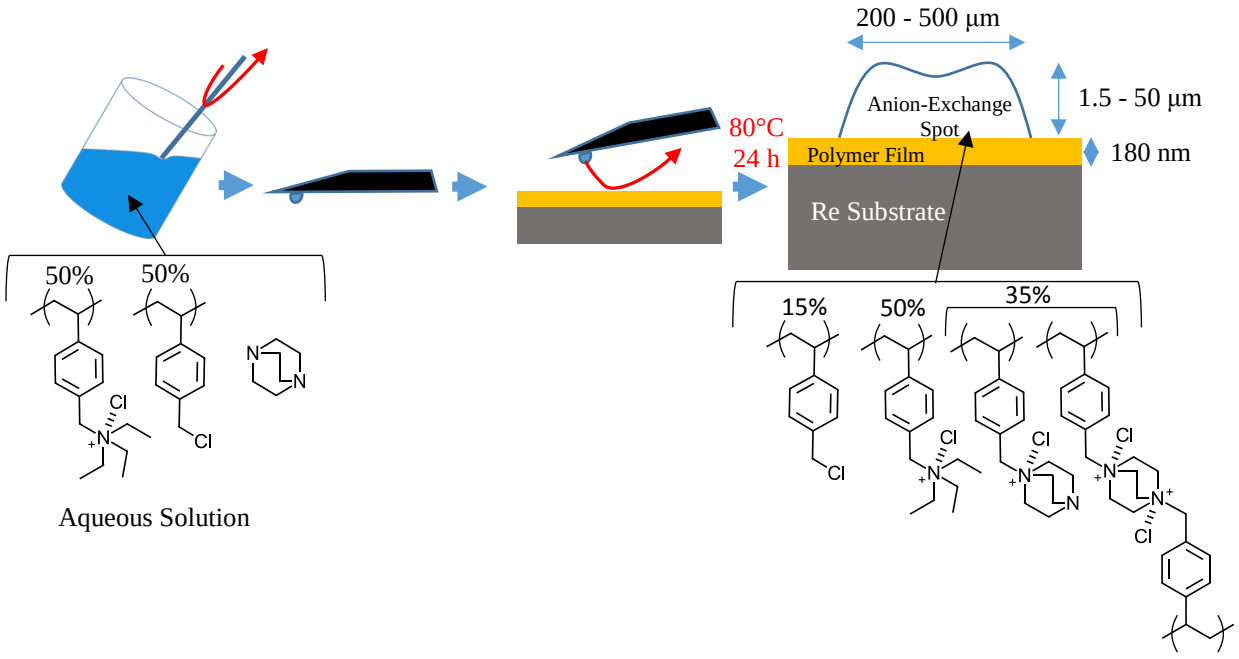

Figure 2.6 "Needle method" used to cast small polymer spots onto polymer coated rhenium filaments. Conversion values represent ideal conversion based on stoichiometry.

2.2.9 Anion-exchange fiber formation

A 30 wt% PVBC solution in chloroform (10 g total) was prepared alongside a solution of DABCO (18.4 mg DABCO/g PVBC) in 0.5 g chloroform. The PVBC and DABCO solutions were mixed for approximately 1 min immediately prior to fiber formation. Figure 2.7 illustrates the fiber formation method, which involved (a) drawing the PVBC/DABCO solution into a glass pipette, depositing 5–20 μL onto aluminum foil, and allowing it to dry for 2 min to a tacky state; (b) using the pipette to form a 5 cm long fiber by contacting the tip with the tacky solution, slowly drawing the tip upward, and holding the wetted fiber in place for approximately 1 min to allow it to dry partially; and (c) applying tension to the fiber after 1 min of drying to keep fibers from curling and to reduce fiber diameters. The fiber is held under tension for 1 min before cutting both ends with scissors. To attain fiber diameters of approximately 100 μm, the target final length of the fiber was 10 cm. After drying for approximately 1 h at room temperature, the polymer fiber was heated at 80 °C for 24 h to accelerate cross-linking with DABCO. Figure 2.3 depicts the reaction between PVBC and DABCO. Fibers were removed from the oven and submerged in a solution of 5 wt % TEA in chloroform for 48 h at room temperature. Figure 2.4 depicts the reaction of TEA with chlorobenzyl sites of PVBC to form quaternary amine sites capable of anion exchange. After soaking in the TEA solution, fibers were dried under vacuum (~85 kPa vacuum) at room temperature for 2 h. Figure 2.8 shows an image of a PVBC-DABCO-TEA fiber prepared by this method.

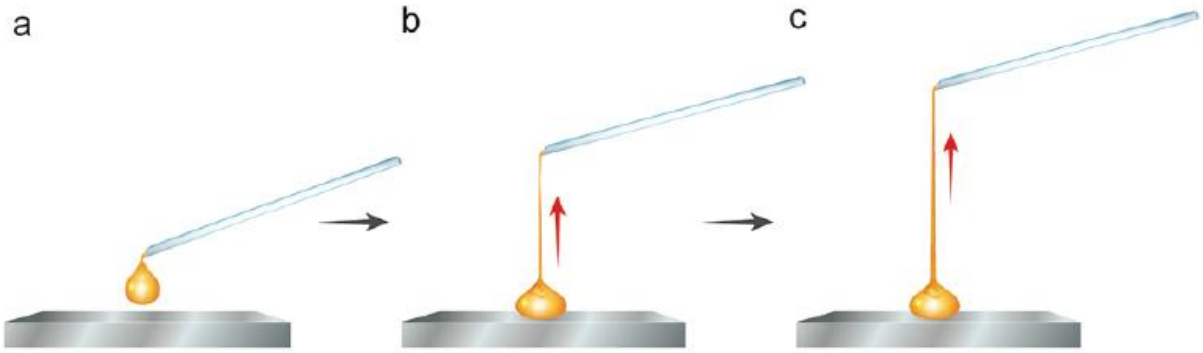

Figure 2.7 Method of forming ion-exchange polymer fibers with glass pipettes: a) 5–20 µL of a viscous polymer solution is deposited onto aluminum foil and allowed to dry to a tacky state (~2 min). b) A pipette is used to draw a fiber from the tacky droplet by contacting the tip and drawing upwards. c) After approximately 1 min of drying the fiber is placed under tension, increasing its length and narrowing, before drying for 1 min under tension.

Figure 2.8 An image of a fiber prepared using the fiber formation method. Note: a fiber with a diameter of ~300 µm was imaged due to difficulties imaging thinner fibers without magnification.

2.2.10 Determination of film thicknesses by ellipsometry

Film thicknesses were measured by multi-angle, single wavelength ellipsometry (Beaglehole Instruments, Picometer). Silicon wafers were used as surrogate substrates for thickness determination, as the geometry and roughness of rhenium filaments made direct measurements of films deposited on filaments by ellipsometry unreliable. The incident beam was produced by a 632.8 He-Ne laser source. Measurements were done at incidence angles from 62° to 80° with a step increment of 3°. The reported thickness is an average of five random locations on each wafer. A PVBC-silicon dioxide-silicon substrate three-layer model was applied to fit the data. PVBC thickness and refractive index based on a Cauchy model were allowed to vary and were calculated by IgorPro Software v4.0A.

2.2.11 Optical microscopy of anion-exchange fibers

Optical microscopy was used to determine the diameter of fibers and select fibers with diameters of approximately 100 μm for sample loading. An Amscope B-series binocular microscope with an Amscope MU900 USB digital camera and FMA 050 adapter was used to capture images of fibers at a magnification of 10x; an image of a fiber is shown in Figure 2.9a. A stage micrometer was used to calibrate size measurements and can be seen in Figure 2.9b. Major units on the stage micrometer represent 100 μm. Fibers were placed between microscope slides for imaging.

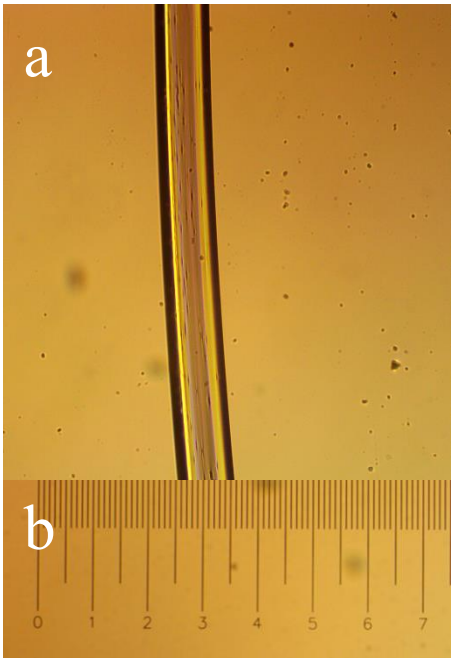

Figure 2.9 Optical microscopy image of a) ~100 μm diameter polymer fiber before sectioning and b) the stage micrometer used to determine the diameter of fibers. Major scale bar increments represent 100 μm.

2.2.12 3-Dimensional scanning electron microscopy and scanning electron microscopy energy dispersive X-ray spectroscopy

3-Dimensional scanning electron microscopy (3D SEM) was performed on a Hitachi S3400 variable pressure SEM at a pressure of 30 Pa. Variable pressure 3D-SEM was used to create 3D profiles of toroidal polymer spots to determine spot dimensions. The following instrument settings were used for 3D imaging: 10 mm working distance, 15 kV acceleration voltage, 50 μA of probe current, backscatter mode, and a magnification of 100x. Silicon wafers that had been dip-coated and deposited with toroidal polymer spots were attached to SEM grids with carbon tape. 3D profiles were created using 3-D Image Viewer version 1.01 by combining images from four opposing backscatter detectors and calculating dimensions based on shading.

SEM imaging in secondary electron mode, SEM backscatter imaging, and SEM-energy dispersive X-ray spectroscopy (SEM-EDS) was used to map the elemental composition of filaments that broke during analysis. This work was performed at SRNL. A 20 kV acceleration voltage and a working distance of ~8.5 mm was used for these analyses. SEM imaging of dimpled filaments was performed at Clemson University on a Hitachi SU6600 Variable Pressure SEM under high vacuum. These images were collected in secondary electron mode with an acceleration voltage of 20 kV and a working distance of ~9.5 mm.

2.2.13 Atomic force microscopy

Atomic force microscopy (AFM) images were obtained using a Bioscope AFM (Bruker, Inc.) with NanoScope III A controller. Silicon cantilevers (MikroMasch, Inc., NSC15/Si3N4/AIBS/50) were used as probes for the tapping mode measurements. AFM images were taken with 256 × 256 pixel resolution over areas of 1-10000 μm^2 at scan rates of 0.25-1.0 Hz. Toroidal polymer spots were deposited on transparent glass that had been dip-coated with a PVBC-DABCO film so that spots could be located using the optical microscope attached underneath the AFM stage. The AFM has a maximum Z-range of 7 μm, so only a portion of the toroidal polymer spots could be imaged using AFM.

2.2.14 Batch Pu uptake study

David Locklair performed the work presented in this section using sample substrates that I prepared. He carried out the uptake measurements during his graduate studies under the advisement of Dr. Brian Powell. Batch Pu uptake experiments performed by David Locklair are described in his Master's Thesis [124].

2.2.15 Determination of binding capacities

David Locklair performed the work presented in this section using sample substrates that I prepared. He carried out the uptake measurements during his graduate studies under the advisement of Dr. Brian Powell. Binding capacity experiments performed by David Locklair are described in his Master's Thesis [124].

2.2.16 Alpha Spectroscopy

David Locklair performed the majority of the work presented in this section using sample substrates that I prepared. He carried out the alpha spectroscopy during his graduate studies under the advisement of Dr. Brian Powell. Alpha spectroscopy experiments performed by David Locklair are described in his Master's Thesis [124].

2.2.17 Acid stability of thin films

Rhenium and silicon wafers were dip-coated with PVBC-DABCO films following the procedure described in section 2.2.4, and a portion were quaternized with TEA following the procedure described in section 2.2.5. After casting, film coated substrates were soaked in DI water for 24 h to remove any unreacted TEA or DABCO physically entrapped in the film. PVBC-DABCO-TEA films (and PVBC-DABCO) on silicon wafers were exposed to either 8 M HNO_3 or 9 M HCl by submerging for up to 72 h. After exposure, films were allowed to drip-dry (suspended above reservoirs of the respective acid solution) for approximately 24 h. Film thicknesses were measured using the procedure described in section 2.2.10 before and after acid exposure (only performed with silicon substrates). Polymer coated rhenium wafers (1 cm × 3 cm

sheets) were placed in 8 M HNO_3 for 5 h. Coated rhenium wafers were weighed and photographed before and after exposure to nitric acid.

2.2.18 Bead-loading and TIMS analyses

The bead loading method is described elsewhere [3] and commonly used by team members at SRNL. Four anion-exchange resin beads were contacted in 50 µL of 8 M HNO_3 containing 10 pg of NBL CRM Pu-128 to extract the Pu sample, in the form of a $Pu(NO_3)_6^{2-}$ anionic complex, into the bead structure. Figure 2.10 shows a depiction of this equilibrium reaction. Beads were submerged in solution and agitated using a Tekmar VSR-S10 shaker for a minimum of 4 h before being removed and glued to degassed filaments using 10 µL flexible collodion solution. The four beads were loaded onto a single filament in a line at the center of a V-shaped or dimpled filament. After gluing beads, several filament assemblies were loaded into the TIMS sample turret for analysis. Each filament assembly represents one sample. A consistent instrument methodology was used for all analyses including alternative sample loading strategies described in other sections.

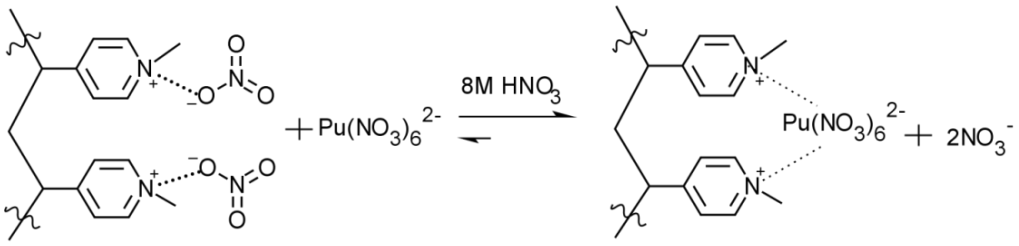

Figure 2.10 Equilibrium between Q-type anion exchange resin and $Pu(NO_3)_6^{2-}$ in concentrated nitric acid solutions.

2.2.19 Sorption of Pu onto thin-film coated filaments

Thin film coated filaments (films prepared with localized TEA quaternization, section 2.2.6 and toroidal polymer spots, sections 2.2.8) were direct loaded with 10 pg of NBL CRM Pu128 from either a 9 M HCl or 8 M HNO_3 matrix (5 µL deposited volume) onto the hydrophilic region of the film and dried using a heat lamp. In the case of toroidal spot sample preparation, loading from an 8 M HNO_3 matrix was found to result in degradation of the rhenium substrate and subsequent sample loss; therefore, 9 M HCl was used for the majority of these trials. After direct loading and drying filament assemblies were placed in the TIMS sample turret and analyzed.

2.2.20 Anion-exchange fiber loading

Fibers were cut into six 2.5 mm sections. Each was placed in 50 µL of 8 M nitric acid containing 10 pg of NBL CRM Pu128 and agitated using a Tekmar VSR-S10 shaker for a minimum of for 4 h. Thereafter, the Pu loaded fibers were removed from solution and glued to degassed V-shaped filaments (degassing described in section 2.2.2) using 5 µL of collodion solution. After gluing fibers filament assemblies were placed inside the sample turret of the TIMS system.

2.3 RESULTS AND DISCUSSION

2.3.1 Determination of baseline TIMS performance using the established bead-loading technique

The bead-loading technique described in section 2.2.18 is used regularly by our collaborators at SRNL for ultra-low-level isotopic ratio measurements of Pu. As described in section 2.1, the method has been in use for several decades and is considered the "gold standard" for low-level determination of isotopic ratios and mass amounts of Pu. A major detraction to the method is that sample loading for Pu is time-consuming, difficult, and expensive. Collaborators at SRNL state that the cost of analysis using this method, when charging external clients, is between $1,500 and $2,500 per purified sample. The cost of analysis doubles if sample purification is required. Due to the high monetary costs of these measurements, a limited set of control samples were analyzed using the standard loading procedure at SRNL. These samples were used as a comparative baseline for the performance of alternative sample loading techniques, and a summary of these data is shown in table 2.1.

A performance metric not shown in table 2.1 is sample loss. Of the 7 control samples run, one resulted in total sample loss during the tuning phase of analysis due to a filament failure (i.e., a broken filament). This represents approximately 15% sample loss for our trials; however, due to the small number of control runs, this metric is difficult to quantify statistically for the standard method. Up to 25% sample loss has been reported in the literature when using the standard bead-loading technique [84]; however, our experienced operator at SRNL has stated this figure is closer to 20%. Sample loss when using the bead loading technique can occur either from filament failure or bead detachment. To mitigate the latter phenomenon, 4 beads are loaded onto filaments at SRNL; however, this practice is believed to reduce the sensitivity of the method

as ion production is more dispersed across the filament (as opposed to the case where a single bead is loaded) and more of the actinide sample may remain entrapped on the filament in the graphitic skeleton that forms when using bead loading [111]. The cause of bead detachment is unknown but it has been hypothesized that it is the result of explosive decompression due to the vaporization of water entrapped in rigid Dowex anion-exchange resin beads. It also has been noted by collaborators at SRNL based on post-run observations of filaments that beads migrate from their original location of deposition during the heating process; therefore, beads may simply migrate to a filament edge and fall off of the filament.

Table 2.1 TIMS runs conducted using the standard SRNL bead loading method with V-shaped rhenium ionization filaments. Ten picograms of NBL CRM Pu128 were loaded onto beads from an 8M HNO_3 matrix and attached to filaments using a flexible collodion solution. Pu^{239} + Pu^{242} counts refers to the number of Pu atoms detected and represents relative measurement sensitivity. Runs that resulted in 0 Pu atom counts due to filament failure are not shown or included in statistical calculations reported.

Sample #	Pu^{239} + Pu^{242} Counts	Pu^{239} / Pu^{242} Ratio
1	369,054	1.001
2	45,125	1.004
3	208,767	1.001
4	166,263	1.003
5	452,711	0.999
6	361,867	1
Average	267,298	1.001
Standard Deviation	152,755	0.002
Relative Standard Deviation	57.1 %	0.186 %

Table 2.1 shows that the relative standard deviation in the total counts acquired from a series of runs (~57%) is two orders of magnitude greater than the relative standard deviation in the measured isotopic ratio (~0.19%). This behavior is typical in TIMS systems, and is why isotope dilution is used for quantity measurements (described in Chapter 1). The sample utilization (defined as atoms detected per atoms loaded; represented by total measured counts in table 2.1) can vary by up to an order of magnitude between samples prepared identically. This behavior is well known but not understood at this time. It has been theorized that inter-sample variability may be due to the polycrystallinity of rhenium surfaces, as different crystalline planes of rhenium exhibit significantly different work functions [105]; however, this theory is not supported by studies that have shown that polycrystalline rhenium filament surfaces are highly oriented in the basal (0001) direction [125]. The work function of a thermal ionization surface is proportional to the ionization efficiency of a loaded analyte, as described in section 2.1. Efforts were made in our group to map the orientation of polycrystalline rhenium filament surfaces used in this study [126] and are described in chapter 3. Our work also indicated that these surfaces are highly oriented in the basal direction with few non-basal grain orientations being present. Non-basal oriented grains represent a small fraction of the surface and cannot fully account for the ubiquitous inter-sample variability in ionization efficiency measured using these analyses. We propose an alternative theory [122] regarding this behavior in chapter 3.

The average sample utilization efficiency (defined as [atoms loaded / atoms detected] × 100%) using the standard SRNL bead loading procedure is approximately 0.001% given a 10 pg load of Pu standard. Sample utilization is a measure of overall efficiency and is a function of the ionization efficiency, instrument ion transferal efficiency, and detection efficiency. Sample utilization using the SRNL TIMS system and bead loading procedure is below some efficiencies

reported in the literature for the method (approximately 0.1 – 1.0 % overall efficiency [106]). This difference is the result of several factors. Most importantly, the SRNL TIMS is operated in what is known as a "peak-hopping" (a.k.a. peak –jumping) mode. Figure 2.11 shows a typical mass spectrum produced by the SRNL TIMS system used for all analyses in this study. In peak-hopping mode, the ion detector is physically moved within the apparatus, scanning a mass range defined by the physical position of the detector. Ions pass through a magnetic field produced by a permanent magnet; therefore, the magnetic field strength is constant during a run and the trajectories of ions with a given mass-to-charge ratio (m/z) are constant. Moving the detector across the various streams of ions in periodic sweeps scans a defined mass range based on the trajectory of the ion beams. Figure 2.12 shows a graphical representation of this concept. Peak-hopping can also be performed with a static detector by altering the magnetic field strength in the mass analyzer or the electrostatic potentials within the system. The width of the peaks shown in figure 2.11 are a result of the detector size and slight differences in the trajectory of ions, arising from differences in the physical origin of ions and/or differences in kinetic energy. A downside to the peak-hopping method of detection is that it inherently leads to loss of some fraction of the sample while the detector is out-of-place for a given ion beam. Multi-collector systems have been developed in recent year to overcome this limitation and improve overall efficiencies. In multi-collector systems, multiple ion detectors are used simultaneously; thus, the detectors do not have to be moved and sample atoms are not lost due to the position of the detector. The study reporting overall efficiencies from 0.1 to 1.0% used this multiple ion counting strategy to improve sample utilization [106]. Differences in ionization efficiency also can arise from the type of detector, as these have improved greatly in terms of detection efficiency in recent years [1], the use of total evaporation techniques (running a sample to exhaustion) [127], and the

efficiency of ion optics within the TIMS system. All trials in this study were limited to a maximum of 4 h of analysis time due to operator constraints. Due to these factors, sample utilization efficiencies presented in for this body of work do not represent highest achievable efficiencies using a given sample loading procedure. A consistent instrument methodology was used for all trials to allow for valid comparison of the relative performance of various sample loading methods and procedures.

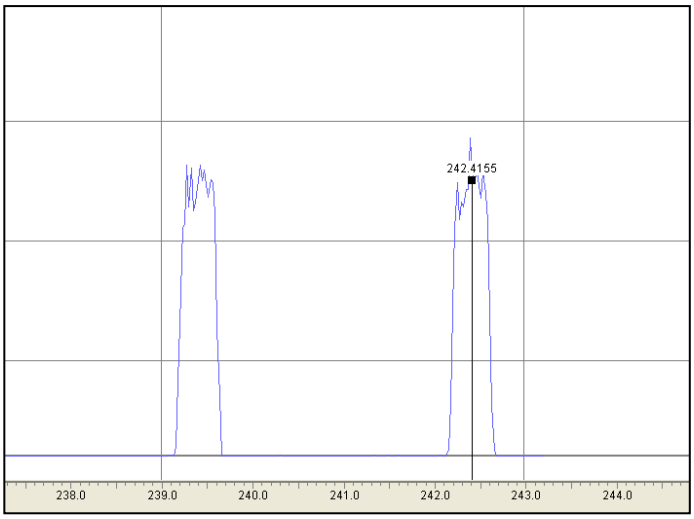

Figure 2.11 A typical mass spectrum acquired when analyzing NBL CRM Pu128 using the bead loading method. NBL CRM Pu128 has a certified Pu^{239} / Pu^{242} ratio of 1. To obtain an isotopic ratio, counts under each peak are summed and the quotient of counts is taken. Note: no interference or peak tailing can be seen in this mass spectrum. Random interferences across the entire mass spectrum usually are related to organic interferences, while natural uranium contamination usually is identified as a peak at m/z = 238.

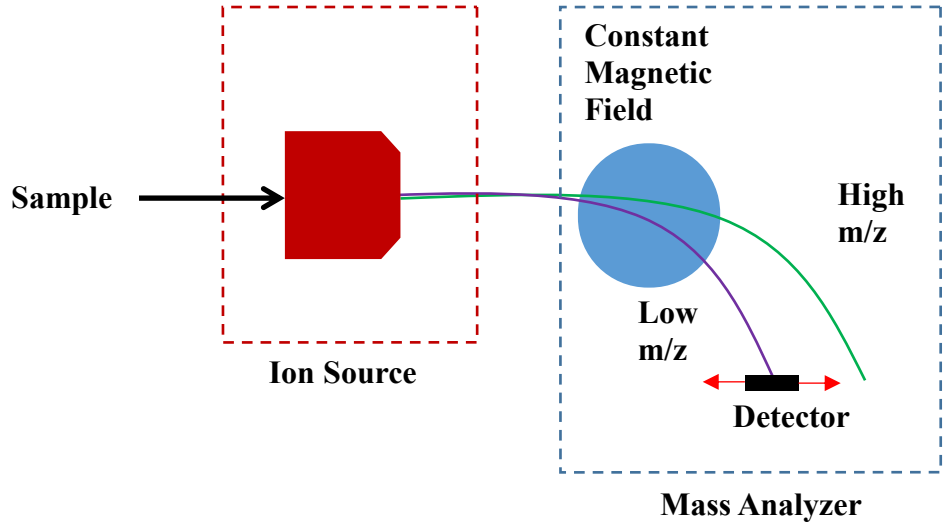

Figure 2.12 Depiction of a TIMS system operated in "peaking hopping" detection mode with a magnetic sector. Low m/z ions are deflected to a greater extent than high m/z ions by the constant magnetic field due to differences in momentum.

2.3.2 Effect of the "dimpled" filament geometry on TIMS analyses of ultra-low-level Pu samples using the established bead-loading technique

Thermal ion source geometries used in TIMS analyses have been studied in efforts to increase ion yields and focus the transmission of ions into the mass spectrometer [84, 117, 118, 128]. A goal in some ion source designs has been to increase contact, or the number of interactions, between the sample atoms and the ionization surface. In TIMS analyses of Pu, the majority of the loaded sample is emitted from the filament as neutral gas atoms (maximum ionization efficiency: direct loading ≈ 0.01 - 0.1%; resin bead loading ≈ 0.1 – 1.0%) [2]. By loading the sample in a concave thermal ion source, neutral gas atoms have opportunities to interact with the ionization surface multiple times [128]. In one design, the cavity source, high ionization efficiencies (~10%) relative to other methods were achieved by loading sample-bearing resin beads into the back of a capped rhenium tube heated by an electron gun [117]. It is

theorized that neutral gas atoms produced at the closed end of the tube will scatter along the inside of the tube, thus having multiple opportunities to collide with the tube surface and become ionized. Porous ion emitter designs have emulated this concept by creating micro-porous rhenium structures on electrically heated filaments [84]. Other ion source geometries include the V-shaped filament (a.k.a. “boat” or “canoe” type filaments), where the rhenium ribbon is crimped into a long channel. V-shaped filaments have been shown to increase ion focusing [118] and aid in sample loading [106]. In this study, we investigated the use of a new concave filament geometry, the “dimple”.

The dimple filament geometry was developed to simplify sample loading and improve the performance of thin-film based TIMS sample loading procedures that were under development by our group [129], but it has been extended to the bead-loading strategy. It was hypothesized that dimpled filaments would improve sample utilization over that of V-shaped filaments when employing the bead loading method due to three mechanisms: 1) The more concave geometry of dimpled filaments would present greater opportunity for neutral gas atoms to interact with the ionization surface after volatilization. 2) The more confined geometry of dimples would limit the migration of beads on the ionization surface during analysis, aiding in ion focusing and retaining a concentrated ion production region. 3) The cup-shape of dimpled filaments would allow for greater direct interaction between beads and the ionization surface. Figure 2.1 shows a comparison of the V-shaped and dimpled filament geometries. The crimped region of dimpled filaments is limited to the geometric center of the filaments, aiding in sample alignment during loading. Proper sample alignment improves transference efficiency of ions into the TIMS system. Figure 2.13 shows an SEM image of the crimped region of dimpled filaments.

The dimpled region is approximately 400 μm × 400 μm. The small size of dimples helps to maintain a concentrated ion source aiding in ion focusing into the mass spectrometer.

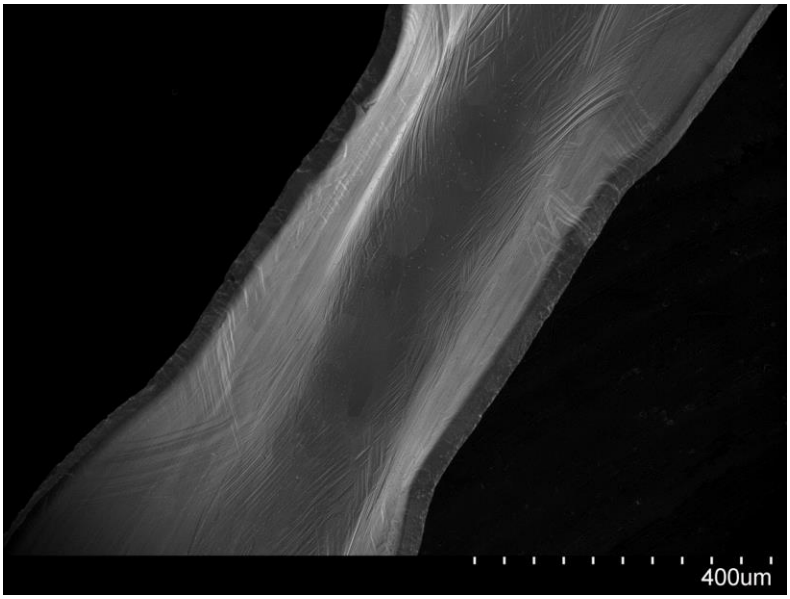

Figure 2.13 SEM image of the crimped region of a dimpled rhenium filament.

Dimpled filaments were loaded with beads in the same manner as V-shaped filaments and the average sample utilization and isotopic ratios measured using the filament geometries were compared. Table 2.2 shows a comparison of ion production (atom counts) between the standard V-shaped filament design and dimpled filaments. The average number of Pu counts detected using dimpled filaments was approximately 34% greater than that using the standard V-shaped filament geometry. The average isotope ratio measured for NBL CRM Pu128 when using dimpled filaments was comparable to the average ratio measured using V-shaped filaments (1.0018 versus 1.0013). More importantly, no sample losses were experienced when beads were loaded onto dimpled filaments (25 samples), compared to the 15% sample loss experienced with V-shaped filaments (7 samples). Sample loss is a notorious problem when employing the bead

loading method [84], so overcoming it represents a major accomplishment. We hypothesize that the reduction in sample loss when using dimpled filaments is the result multiple points of, or greater, contact between beads and the ionization surface. Additionally, the use of dimpled filaments limits the migration of beads on the surface of heated filaments. The frequency and necessity of ion beam refocusing was reduced in analyses using dimpled filaments compared to cases where V-shaped filaments were used. Inspection of V-shaped filaments post-analysis suggest that beads move from their point of deposition when heated in the ion source. This behavior was significantly suppressed when dimpled filaments were used. Section 2.3.9 describes the used of dimpled filaments with the thin film loading strategy.

Table 2.2 A comparison of TIMS performance using the bead-loading method and 10 pg Pu loads between the V-shaped and the dimpled filament geometries. Uncertainties represent 95% confidence intervals. Runs that resulted in 0 Pu atom counts due to filament failure are not shown or included in statistical calculations reported.

Filament Geometry	V-Shaped	Dimpled
Average Detected Pu Counts	267,298 ± 122,229	360,394 ± 69,348
Standard Deviation in Pu Counts (RSD)	152,755 (57%)	176,908 (49%)
239Pu/242Pu Ratio	1.0013 ± 0.0015	1.0018 ± 0.0009
Standard Deviation in Isotope Ratio Measurements (RSD)	0.0019 (0.19%)	0.0024 (0.24%)
Number of Measurements	7	25
Number of Filament Failures	1	0

2.3.3 Development of quaternary amine bearing thin-films for rhenium filament coating and characterization of Pu uptake kinetics

Functionalized films composed of PVBC cross-linked with DABCO and quaternized with TEA were prepared by methods described in section 2.2.4 and 2.2.5 on silicon substrates for Pu uptake characterization. PVBC-DABCO films cast from 2 wt% PVBC in chloroform solution were approximately 120 nm in thickness prior to TEA modification. Film thicknesses increased to approximately 180 nm after modification with TEA in chloroform. Substrates modified using the "neat TEA" method (with no DABCO cross-linking) were not used in this study as these films did not swell in aqueous solutions and there were concerns regarding film dissolution due to the lack of cross-linking. TEA does not dissolve or swell PVBC, and so neat-TEA treatment could be used to create quaternized films of PVBC without cross-linking. Neat TEA also does not swell PVBC-DABCO films (with 5% cross-linking). In the case of neat TEA conversion, we have hypothesized that quaternization is limited to a thin layer near the surface of films due to the lack of swelling, thus, penetration into the PVBC film. When TEA is mixed with chloroform, the mixed solution swells PVBC-DABCO films during the conversion process, creating quaternary amine sites within the bulk of the films. This method could not be performed with non-cross-linked PVBC films as the TEA/chloroform solutions would dissolve the films.

Polymeric films were functionalized with TEA to produce quaternary amine anion-exchange sites for binding $PuCl_6^{2-}$ and $Pu(NO_3)_6^{2-}$ anions. A quaternary amine-bearing polymer was selected for Pu loading due to a history of use in radiochemistry [120] and because the bead loading methodology uses Q-type resin beads [113]. PVBC is commercially available and offers a convenient platform to produce quaternary amine sites from a variety alkyl-amine reagents. TEA was selected as the amination reagent due to its ease of use. Unlike trimethylamine, TEA is

in a liquid state at room temperature. DABCO, a diamine, was used as a cross-linking agent to prevent dissolution of the TEA-quaternized PVBC films when exposed to aqueous solutions. Quaternary amine sites are produced in the reaction between DABCO and PVBC; therefore, it was theorized that high levels of cross-linking could be achieved without great sacrifice to ion-exchange capacity or hydrophilicity of the film. PVBC films and PVBC-DABCO films with no TEA modification were prepared as controls. PVBC and PVBC-DABCO films are hydrophobic while PVBC-DABCO-TEA films are hydrophilic. Five percent cross-linking, based on a 1:2 reaction of DABCO to chloride sites along the PVBC chains, was determined to be the minimum level of cross-linking required to prevent film dissolution in chloroform after baking films at 80 °C for 24 h. Although the reaction between DABCO and PVBC creates quaternary amine sites, it was theorized that by minimizing the level of cross-linking, films with a high degree of swelling could be created that would improve uptake kinetics. However, this theory was not tested, as the thin-film loading strategy was abandoned early in development as irreconcilable problems were identified with the strategy. These issues are discussed in section 2.3.5. Despite the abandonment of the initial thin-film loading design, the following work forms the basis of our understanding of the PVBC-DABCO-TEA system with regards to anionic-Pu complexation. This general polymer formulation was used for all other work towards the development of an alternative sample loading strategy for Pu analysis by TIMS.

In addition to the TEA functionalization, cross-linking of the films by DABCO also produces possible binding sites and so the uptake of Pu(IV) was examined for three sets of films. The first set was PVBC only. The second set was PVBC with 5% cross-linking by DABCO. The third set was PVBC with 5% cross-linking by DABCO and functionalized with TEA. All film types were cast on silicon substrates. The decrease in activity of the aqueous phase as determined

by ICP-MS and LSC was attributed to the ion exchange of the Pu species onto the polymer. Experiments were conducted to ensure that the silicon substrate or container walls were not appreciably contributing to Pu uptake from solution.

Batch uptake experiments are described in detail in David Locklair's Master's Thesis [124]. The following analyses, discussion, and data are recreated with permission from David Locklair. The data were fit to a linear distribution coefficient (K_d) that relates the mass of sorbed Pu per kg of sorbent ($mol_{Pu}\ kg^{-1}_{sorbent}$) to the equilibrium aqueous phase concentration ($mol_{Pu}\ L^{-1}_{solution}$). The concentration of sorbed Pu on the thin-film sorbent ($[Pu]_{solid}$) is given by equation 2.2 where $[Pu]_{aq(0)}$ represents the initial Pu concentration at time zero, $[Pu]_{aq(t)}$ is the aqueous Pu concentration at equilibrium, V is the volume of the solution (L) and $m_{sorbent}$ is the mass of the sorbent (kg). The linear distribution coefficient is defined in Eq. (2.3) as the ratio of the concentration on the solid at equilibrium ($[Pu]_{solid}$) to the concentration of Pu in the aqueous phase at equilibrium ($[Pu]_{aq(t)}$).

$$[Pu]_{solid} = \frac{([Pu]_{aq(0)} - [Pu]_{aq(t)}) * V}{m_{sorbent}} \tag{2.2}$$

$$K_d = \frac{[Pu]_{solid}}{[Pu]_{aq(t)}} \tag{2.3}$$

The K_d of the 5% cross-linked, TEA functionalized films showed relatively good reproducibility with an average K_d of 9070 ± 2960 L kg^{-1} (shown in figure 2.14). The average calculated K_d is slightly lower but comparable to the approximate value of 10000 L kg^{-1} for Dowex 1 anion-exchange resin commonly employed in TIMS measurements. Differences in the K_d value calculated from the three replicates in figure 2.14 may be due to sample-to-sample variation in the degree of conversion during TEA functionalization or differences in the polymer

mass. Determining the mass of polymer films was difficult due to the very low mass of films and the hygroscopic nature of these films. It is unknown exactly what conversion was achieved for each of the three replicate samples; therefore, an assumed total mass of the film (0.001 g) was used in the K_d calculation based on the average mass of 20 films weighed in the presence of desiccant. Silica gel desiccant was placed inside the microbalance chamber and the film was allowed to equilibrate for ~10 min before recording the mass.

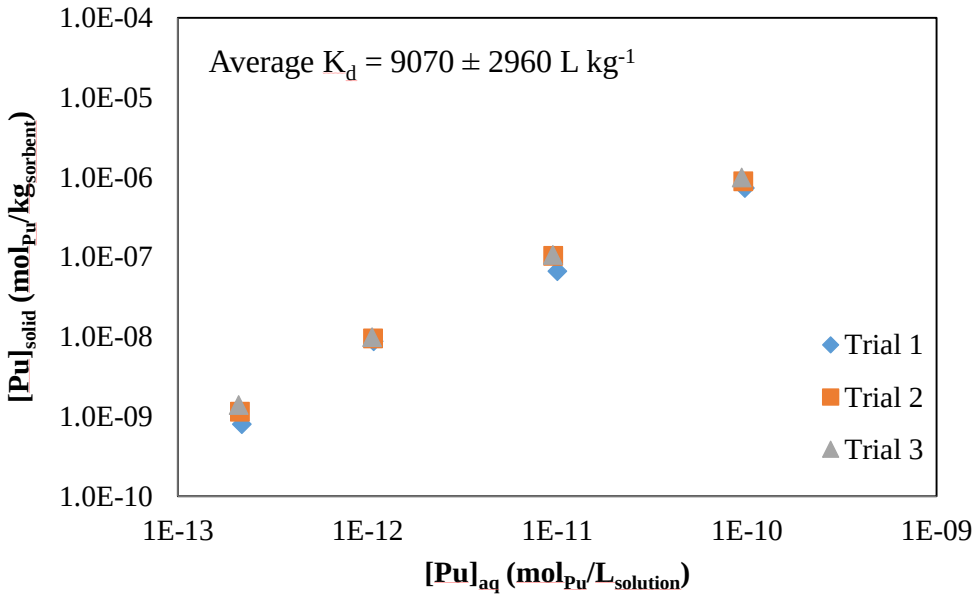

Figure 2.14 Recreated with permission from David Locklair. Sorption isotherm of ^{238}Pu (IV) on 5% cross-linked films with TEA functionalization. The corresponding K_d calculations were 10485 L/kg, 9208 L/kg and 7531 L/kg for trial 1, 2, and 3. All R^2 values were > 0.999. The uncertainty value is given as 2σ.

Uptake of Pu(IV) on the PVBC-DABCO films were examined for comparison and are given in Figure 2.15. The PVBC films exhibited virtually no uptake and so are not given in the

plot. The data in figure 2.15 are plotted as the average of triplicate measurements and the uncertainty is given as 2σ. The data indicate a 10^3-fold increase in uptake for the PVBC-DABCO-TEA films. A K_d was not calculated for the PVBC and PVBC-DABCO films due to the low uptake onto those films.

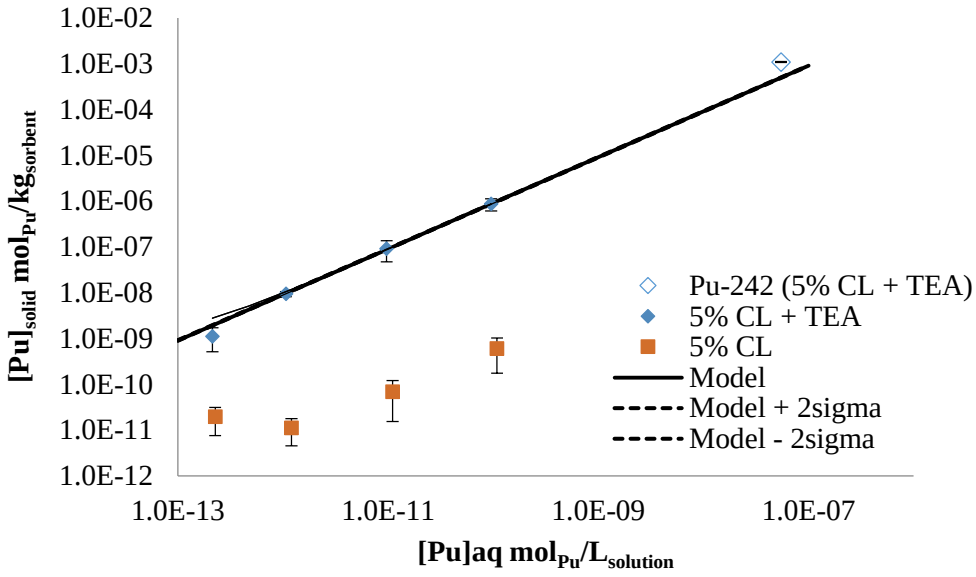

Figure 2.15 Recreated with permission from David Locklair. Sorption isotherm results for ^{238}Pu (IV) PVBC-DABCO-TEA films represented by blue diamonds and PVBC-DABCO films represented by red squares. The unfilled blue diamond is from an uptake experiment with CRM 150 (mainly ^{242}Pu by mass). All data are the average of triplicate measurements and the uncertainty is represented as 2σ. The equation for the linear model fit is given by $[Pu]_{solid} = 9057[Pu]_{aq} + 8.62 \times 10^{-10}$.

The solid-state ^{238}Pu mass was quantified with alpha spectroscopy for comparison to the LSC measurements. The LSC data compared very well with the alpha spectroscopy data for the 1000, 100, and 10 dpm mL^{-1} solutions. A mass balance was calculated for the Pu systems using

the LSC data to calculate the aqueous phase Pu mass and alpha spectroscopy data to calculate the bound Pu mass. The sum of the masses from LSC and alpha spectrometry data was divided by the known mass of Pu in each system to provide a percent balance. The calculated percent mass balances for the 10–1000 dpm mL^{-1} solutions gave values of 88-100%. The lower working concentration of 1 dpm mL^{-1} did not have enough radioactivity to obtain sufficient LSC counts or a good enough alpha spectrum to accurately compare the two methods.

Figure 2.16 shows a typical alpha spectrum from the ^{242} Pu batch uptake experiments with the PVBC-DABCO-TEA film. This is an excellent quality alpha spectrum with resolutions on the order of 25-30 keV, comparable to values obtained from electrodeposited samples for our detectors. Alpha spectra for the PVBC and PVBC-DABCO films (not shown) exhibited significantly lower count rates by 3 orders of magnitude with considerably poorer spectral quality. Chapter 4 discusses our investigation of PVBC-DABCO-TEA films for alpha spectroscopy sample preparation.

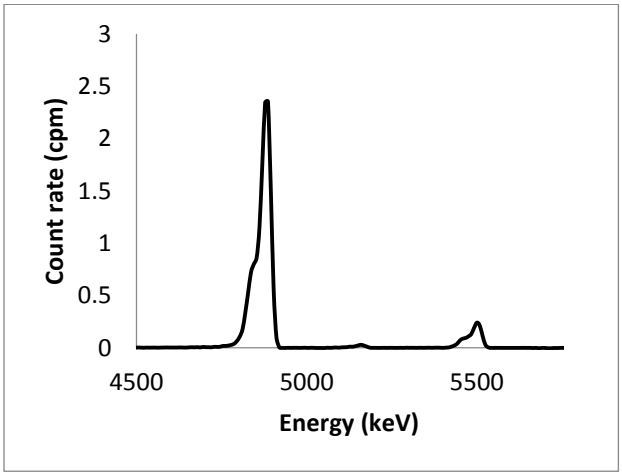

Figure 2.16 Recreated with permission from David Locklair. Alpha spectrum of 5% cross-linked, TEA functionalized films (PVBC-DABCO-TEA) submerged in CRM (^{242}Pu, $^{239/240}$Pu, ^{238}Pu).

Figure 2.17 demonstrates rapid ion exchange under the experimental conditions for both acid systems. Equilibrium between the sorbed Pu species and aqueous Pu was reached within 15 min. The figure is plotted as the fraction of final equilibrium state ($[Pu]_{solid(t)}$ / $[Pu]_{solid(eq)}$) versus the duration of 242Pu exposure. The fraction of final equilibrium state was calculated by dividing the solid Pu concentration at the designated time by the solid Pu concentration at the last data point (t = 15 min). Values were constant past 15 min, however these data are not plotted for simplicity.

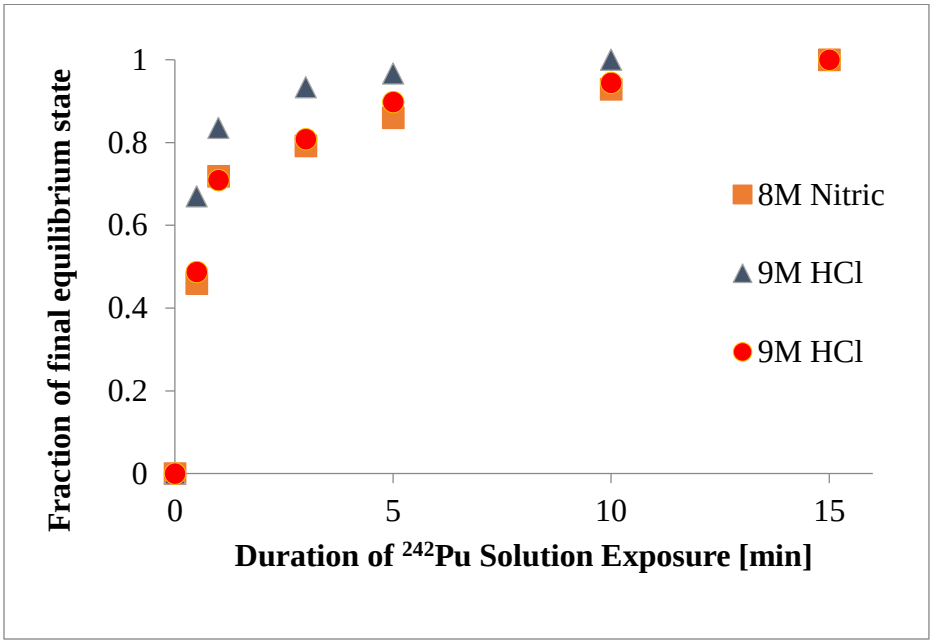

Fig 2.17 Recreated with permission from David Locklair. Uptake of $Pu(NO_3)_6^{2-}$ and $Pu(Cl)_6^{2-}$ on poly(vinylbenzyl chloride) functionalized with tri-ethyl amine on silicon substrates as determined by ICP-MS measurements of aqueous Pu^{242} (NBL CRM 130).

2.3.4 Determination of binding capacities

Binding capacity experiments are described in detail in David Locklair's Master's Thesis [124]. The following analyses, discussion, and data are recreated with permission from David Locklair. An experiment was devised to calculate the total binding capacity of the films per unit mass. For this experiment, radioactive ^{36}Cl was spiked into a 0.02 M NaCl solution to produce a 10,000 dpm/mL working stock solution. A functionalized film was submerged in 10 mL of the ^{36}Cl solution and allowed to equilibrate for 24 h to saturate the binding sites with $^{36}Cl^-$ and Cl^-. The assumption is that the radioactive chlorine-36 will bind to the polymer with the same molar ratio as is present in the solution. The film is then removed from the solution, blotted dry, and placed in 10 mL of a 1 M $NaNO_3$ solution for 24 h. The nitrate effectively displaces the bound chlorine. Figure 2.18 shows the proposed reaction.

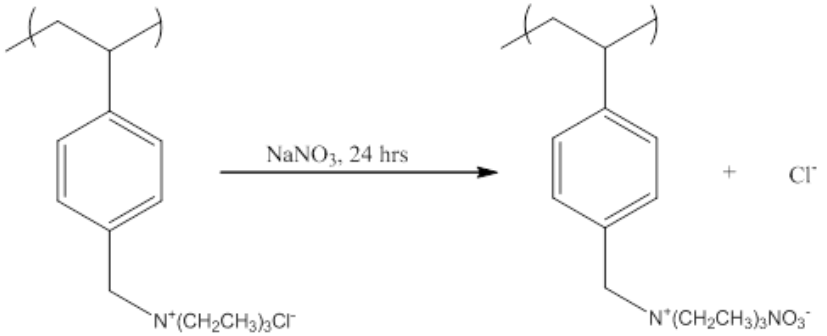

Figure 2.18 Recreated with permission from David Locklair. Reaction scheme for binding site capacity determination.

The nitrate solution was then isolated, and the aqueous ^{36}Cl was measured with LSC. To ensure that all of the bound chlorine was displaced, the film was placed in a third solution of 1 M Na_2SO_4. Sulfate is a much stronger nucleophile than Cl^- and should displace any remaining $^{36}Cl^-$. The aqueous phase concentrations of both solutions were determined and the binding capacity

was back calculated based on the molar ratio of radioactive chlorine to the total chlorine present in the system.

The binding site capacity of PVBC-DABCO-TEA films was found to be $1.25 \times 10^{-4} \pm 1.07 \times 10^{-5}$ eq $g^{-1}_{polymer}$, which is an order of magnitude lower than the Dowex 1 anion-exchange resin capacity of 3.1×10^{-3} eq g^{-1} of resin. The full mass of the polymer film was used in the calculations, as the percentage conversion to functionalized anion-exchange polymer is unknown. The binding capacity of the Dowex 1 resin reported by the manufacturer was verified using the same experimental approach.

2.3.5 Acid stability of quaternary amine bearing films on silicon and rhenium substrates

The conditions needed to load Pu onto Q-type anion-exchange resin requires exposure to high acid concentrations (up to 8 M HNO_3 or 9 M HCl). Nitric acid is used more commonly than hydrochloric acid in separations involving U and Pu, such as in the industrial scale PUREX process that was used extensively in the manufacture of nuclear weapons. Nitric acid is used commonly in Pu sample loading for TIMS, and is used in the standard TIMS sample loading procedure at SRNL. Pu chemistry is complex, and at near neutral pH many oxidation states of Pu can exist simultaneously, including colloidal forms. At very low pH, Pu exists predominately in the +IV oxidation state, and at high HNO_3 concentrations will form the $Pu(NO_3)_6^{2-}$ anion allowing for separations with anion-exchange materials. The $Pu(NO_3)_6^{2-}$ complex reaches peak thermodynamic stability at around 8 M nitric acid. Similarly, in concentrated hydrochloric acid, Pu will form the $PuCl_6^{2-}$ anion, reaching a peak thermodynamic stability at 9 M HCl. Due to the commonality of its use, 8 M HNO_3 was first tested for Pu loading onto anion-exchange polymer films.

To ensure that high acid concentrations do not destabilize the polymer extractant coatings, experiments were done to test stability in HNO_3 and HCl. Table 2.3 summarizes our findings for films cast on silicon wafers. For both PVBC-DABCO and PVBC-DABCO-TEA films, film thicknesses remained the same within measurement uncertainties after soaking in 8 M nitric acid for 2 h and 9 M HCl for 72 h. It is clear that the films are stable over the timeframe needed for sample loading (<15 min, described in section 2.3.3), but exposure to 8 M HNO_3 for greater than 2 h often led to film delamination. PVBC-DABCO-TEA films are not covalently attached to rhenium or silicon substrates, and are held in place by electrostatic interactions. We hypothesize that delamination from silicon substrates in nitric acid solutions after long periods of exposure (>2 h) is due to interruption of electrostatic interactions, possible due to strong interactions between NO_3^- anions and silanol groups on the piranha washed silicon surface. One interesting result was that thickness increased for PVBC-DABCO-TEA films after exposure to 8 M HNO_3. We hypothesize that the increase in thickness is due to exchange of NO_3^- for Cl^-, resulting in an increase in polymer density that manifests as a change in thickness. In contrast, film thickness did not increase appreciably for samples exposed to 9 M HCl. This result supports our hypothesis that increased thickness is due to exchange of NO_3^- for Cl^- as these films are natively in a chloride form after synthesis.

Table 2.3 Results of film stability testing in 8M HNO_3 and 9M HCl. All films were on cast on silicon wafers. Uncertainties represent standard deviations among five measurements.

Film Type	Original Film Thickness	Thickness after Treatment	Treatment Type
	[nm]	[nm]	
PVBC-DABCO (no TEA)	131.4 ± 1.7	131.2 ± 1.4	8M HNO_3 - 2 h
PVBC-DABCO-TEA	174.1 ± 2.1	183.0 ± 3.6	8M HNO_3 - 2 h
PVBC-DABCO-TEA	178.1 ± 1.5	174.9 ± 1.0	9M HCl - 1 h
PVBC-DABCO-TEA	177.2 ± 2.4	176.6 ± 3.4	9M HCl - 17 h
PVBC-DABCO-TEA	183.2 ± 3.0	178.4 ± 2.8	9M HCl - 3 d
PVBC-DABCO-TEA	184.3 ± 1.9	180.3 ± 4.1	1 month aging in atmosphere, no acid exposure

Figure 2.19 presents representative AFM images at two scales for PVBC-DABCO-TEA films before and after soaking in 8 M nitric acid for 2 h. The film morphology remains unchanged by the acid exposure. This supports our hypothesis that film delamination in nitric acid is due to interactions of NO_3^- with the silicon substrate rather than degradation of the film via oxidation or other mechanisms. We do not believe that delamination after long exposure to nitric acid occurs due to film swelling, as films swell rapidly (near instantaneously) upon exposure to aqueous solutions and no delamination was seen in the case of long term exposure to HCl solutions (72 h) when films are also in a swollen state. We hypothesize that films have greater stability in HCl solutions, in terms of delamination resistance, is due to weaker interaction between Cl^- anions and the silanol groups on the oxidized silicon surface than in the case of NO_3^- anions, which are capable of hydrogen bonding with OH groups. Interaction

between NO_3^- anions and the oxidized silicon substrate may disrupt electrostatic interactions between the substrate and the polymer film, thus, leading to delamination of the film.

Similar acid stability tests were conducted with polymer coated rhenium substrates in 8 M HNO_3. Although polymer films were stable on silicon substrates for up to 2 h in 8 M HNO_3, and showed no signs of chemical degradation during this period of time, a major issue was encountered when these experiments were performed with rhenium substrates. Rhenium is soluble in nitric acid, and degradation of the rhenium surface begins immediately upon exposure to nitric acid solutions even when rhenium is coated with polymer. Figure 2.20 shows images of PVBC, PVBC-DABCO, and PVBC-DABCO-TEA coated rhenium wafers after 5 h of nitric acid exposure.

All film types were almost entirely detached from the rhenium substrate after 5 h of nitric acid exposure. Additionally, the rhenium substrate surface was chemically etched away. Coated substrates on average lost 21% of their mass during this treatment. Film detachment began within 5 min of acid exposure, as the rhenium substrate became oxidized and dissolved to form perrhenic acid. Hydrochloric acid is a reducing acid; therefore, rhenium substrates have good stability in HCl as the substrate does not become oxidized. The realization that rhenium substrates rapidly corrode in HNO_3 lead our group to investigate the acid stability of the steel rhenium filament mounts that are used for electrically heating filaments. Both HNO_3 and HCl solutions were found to rapidly corrode the steel posts. These corrosion issues, along with other concerns, lead our group to reevaluate our initial loading strategy and film design.

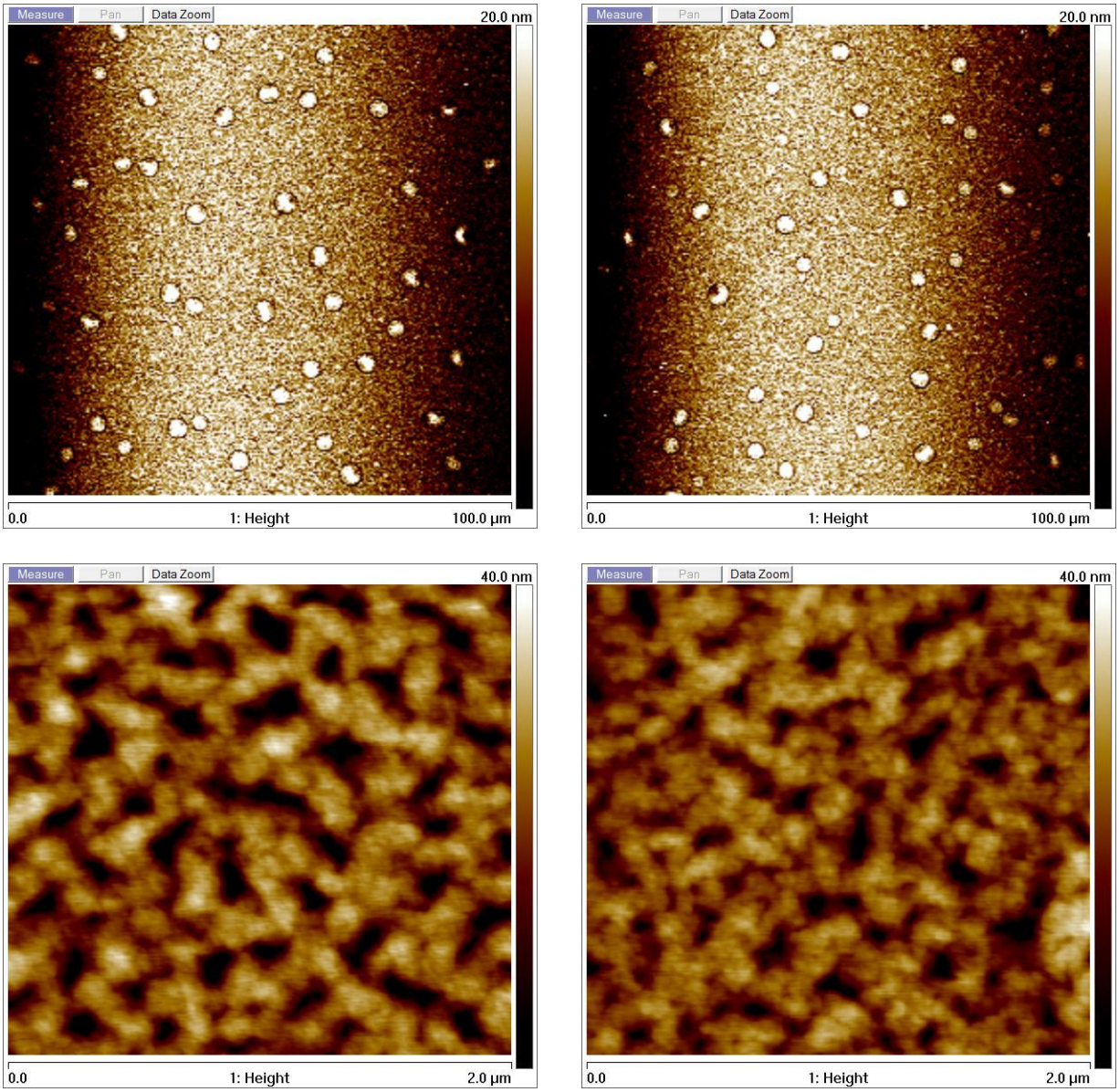

Figure 2.19 AFM images of PVBC TEA modified films before (left side) and after (right side) treatment in 8 M nitric acid for 2 h. Images on top are 100 µm × 100 µm with a 20 nm height scale. Images on the bottom are 2 µm × 2 µm with a 40 nm height scale.

No Nitric Exposure **5 Hours in 8M Nitric Acid**

Figure 2.20 Films cast on rhenium substrates

Originally it was envisioned that rhenium filaments assemblies would be coated with extractive polymer, then submerged into the sample bearing acid solution, extracting and concentrating the Pu sample onto the polymer coated filament. Corrosion of the rhenium filament and steel mounting posts in HNO_3 and HCl made this strategy impractical. The original film design was a uniformly functionalized film where Pu would be distributed evenly across the film. It was brought to our attention, by experts in the TIMS community, that one of the benefits of bead loading is that the method concentrates the sample into a geometrically small region of the filament, producing a narrower ion beam that is more efficiently transferred from the ion source chamber into the mass spectrometer. By loading the Pu sample in a dispersed manner, across the entire area of the filament, this focusing would be lost. To overcome this limitation of our thin film design with regards to ion focusing while attempting to limit filament/steel post corrosion (due to acid exposure), direct loading onto filaments was proposed. Direct loading refers to simply placing the Pu sample dissolved in a small (~5 µL) droplet onto the center of the filament. This method is sometimes used for TIMS sample loading of higher quantity samples where high sensitivity is not required. (TIMS sensitivity for Pu is several orders of magnitude

lower using direct loading compared to bead loading.) However, direct loading onto uniformly functionalized PVBC-DABCO-TEA films was problematic, as the films are hydrophilic and the aqueous sample wets the entire film. Additionally, droplets deposited onto hydrophilic filaments tend to pool towards the "legs" of the filament (the space between the filament and mounting post), which hinders ion focusing. To combat these issues and create coated filaments that are easily direct loadable, a method was developed to create films where quaternization with TEA is restricted to a small area of the film coating. This approach is described in section 2.3.6.

2.3.6 Development and TIMS performance of PVBC films with localized quaternization

After abandonment of the initial design of a uniformly TEA-quaternized PVBC-DABCO film, the idea was proposed to restrict the quaternization reaction with TEA to a small area of the film. It was theorized that by limiting the conversion of chlorobenzyl sites to quaternary amine sites to a geometrically small region of the film, the extraction of Pu would be concentrated into this area, and ion focusing would be improved (over that of a uniformly quaternized film) by limiting the size of the ion point of origin from the filament. Additionally, the base PVBC-DABCO film is hydrophobic, while functionalized PVBC-DABCO-TEA is hydrophilic. Therefore, by creating a small region of hydrophilic polymer amid a hydrophobic polymer film, the aqueous load solution could be contained in a geometrically small region rather than dispersing across the entire filament area when direct loading. Various methods were attempted to limit TEA functionalization of a base PVBC-DABCO film, including simply placing a small drop of TEA onto the center of films. This approach was unsuccessful, as TEA would rapidly evaporate (<5 min) before appreciable quanternization of the PVBC-DABCO film could occur. To functionalize a small region of the PVBC-DABCO film with TEA, a method had to be

developed to maintain contact between liquid phase TEA and the PVBC-DABCO film surface for longer periods of time (ideally on the order of 24 h to mimic TEA exposure times used with uniformly quaternized films described in previous sections).

The capillary spotting technique, described in section 2.2.6, was developed to produce localized TEA-quaternization of PVBC-DABCO films (PVBC-DABCO film thickness of ~120 nm). Contact between liquid phase TEA and PVBC-DABCO films was maintained for up to 4 h (one capillary load) using this method. Capillaries could be refilled (6–7 times) to reach 24 h of contact time between the PVBC-DABCO film and liquid phase TEA. Jigs were constructed to align the capillary, as rhenium filaments are small (< 1 mm in width) and capillaries were difficult to align centrally in the filament without the aid of a guide. Additionally, the jigs maintained a consistent capillary location on the film between refillings of the capillary. Rhenium filaments are delicate; therefore, capillaries were raised off the surface of filaments when refilling the capillaries to prevent deforming the filament. Maintaining a consistent capillary location on the film was necessary to create a concentrated region of TEA quaternization. Figure 2.21 shows a comparison of films quaternized using the capillary method with and without the aid of a jig to align the capillaries between refillings. After filling a capillary, a droplet would form at the capillary tip, and the capillary was lowered until this droplet contacted the film forming a “liquid bridge” between the capillary and the film. Direct contact between the glass capillary and the film was avoided, as this would often damage the film. As the solution dried from the film surface, more was drawn from the capillary and the

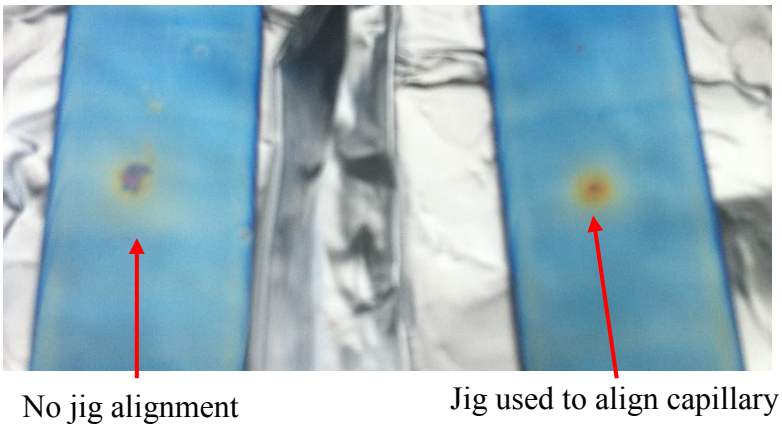

Figure 2.21 Two PVBC-DABCO films prepared on silicon wafers (1 cm x 3 cm) with localized regions of TEA quaternization. The base PVBC-DABCO film is blue while the TEA quaternized region is yellow/red. The left film was modified using the capillary method without the aid of a jig to align the capillary, while a jig was used to align the capillary on the right film. Notice the small red spot of high TEA conversion at the center of the quaternized spot on the right film while the quaternized spot on the left film is larger and less circular.

"liquid bridge" was maintained. A TEA/chloroform solution was used to fill capillaries rather than pure TEA to limit the size of the TEA-functionalized spot. When the droplet on the capillary tip first touched the film surface, the droplet would spread across the entire film surface before drying over the course of ~20 min. After several capillary fillings, this process produced large regions of quaternization. Using chloroform solutions with a low concentration of TEA (~ 5 wt% TEA) restricted quaternization to regions of the film wetted continuously by the capillary (i.e., the area within about 1 mm of the liquid bridge). The capillary aided quaternization process was conducted under a chloroform atmosphere in a closed container to slow the rate of drying from the capillary and to swell the base PVBC-DABCO film with chloroform. It was found that

quaternization of the PVBC-DABCO film occurred more rapidly when exposed to TEA in the swollen state.

Using this method, films with small (~1-2 mm diameter) quaternized spots were created. These spots formed "hydrophilic wells" that adhered aqueous droplets, as needed for direct loading. Figure 2.22 shows an image of a film with a capillary quaternized spot before and after submersion in water.

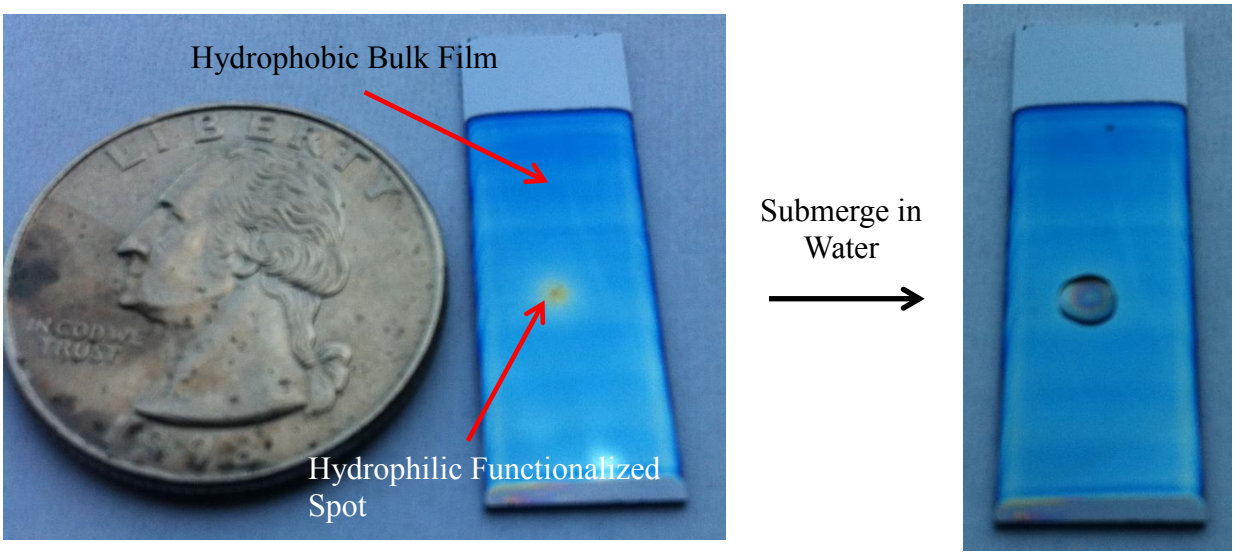

Figure 2.22 Silicon wafer dip-coated to form a hydrophobic PVBC-DABCO film and quaternized in a restricted region using the capillary method. After quaternization using the capillary method and submersion in water, a droplet will cling the hydrophilic spot. We refer to this design (a hydrophilic spot within a hydrophobic film) as the "hydrophilic well".

Capillary quaternized films prepared on degassed rhenium filaments were the first thin-film loading design that was tested on the TIMS instrument at SRNL. These film-coated filaments were each direct loaded via pipette with 10 pg Pu from an 8 M HNO_3 matrix. (Sample

loading with thin film coated filaments is described fully in section 2.2.19.) The film-coated filaments performed poorly compared to filaments prepared using the bead loading method, and provided similar sample utilization to that of direct loading onto bare rhenium filaments. These data are shown in table 2.4, where sample utilization is represented by the total number of detected Pu counts. Due to the similarities with direct loading, it was concluded that the films were too thin (~ 120 nm), and that the carbon of the film dissolved rapidly into the hot rhenium filament (>1500 °C during analysis), thus, performing similarly to filaments that had no film present. This hypothesis was supported by short ion production periods of approximately 15 min (where beads produce ions for at least 4 h of heating).

We decided to test thicker films with localized TEA conversion. PVBC-DABCO base films with a thickness of ~1μm were cast on rhenium filaments by dip-coating and localized TEA quaternization was created using the capillary method with ~24 h of TEA contact time. These films produced more counts than thinner films, but were still well under the performance of filaments prepared using the bead loading method. In addition, these samples had a significantly higher rate of filament failure (8 of 12 filaments with ~1 μm polymer films broke during analysis; 4 filaments broke before any Pu atom counts were detected). These data also are shown in table 2.4. At the time, we were unsure of the cause of these filament failures, but believed that further increasing film thickness in an attempt to further increase sample utilization would likely result in an even higher rate of filament failure since the thinner films (120 nm) resulted in none. Additionally, it would be difficult to produce thicker films using dip-coating due to limitations of the dip-coater (withdrawal rate) and the limited solubility of PVBC in chloroform. There were additional concerns related to organic interferences due to high carbon loading, as several runs with ~1 μm thick films produced highly erroneous isotope ratios. The

certified ratio of $^{239}Pu/^{242}Pu$ in CRM Pu128 is 1, whereas one trial with ~1 μm thick films resulted in a measured $^{239}Pu/^{242}Pu$ ratio of 26). Therefore, it was decided to develop a multi-layer thin film design that would increase carbon loading in the region of Pu deposition, while minimizing the polymer loading elsewhere on the filament. This design strategy, in some ways, mimics the physical distribution of polymer on a filament when using bead loading.

Table 2.4 Comparison of the standard SRNL bead loading method and direct loading to film coated filaments with localized TEA quaternization. Runs that resulted in 0 Pu atom counts due to filament failure are not shown or included in statistical calculations reported.

Trial #	SRNL bead loading method	Direct loading onto bare filament	Capillary method - 120 nm film	Capillary method- 1000 nm film
	Total ^{239}Pu + ^{242}Pu Counts (Atoms) Detected			
1	411,884	12,524	276	84
2	369,054		1,200	490
3	45,125		5,719	83,939
4	208,767		4,717	44
5	166,263		13,027	15
6	452,711		11,308	46,121
7	361,867			16,932
8				10
Average	287,953	12,524	6,041	18,454
Standard Deviation	149,772		5,198	31,019
N Trials	7		6	8
95% Confidence Interval	110,952		4,159	21,495
Minimum Counts	45,125	12,524	276	10
Maximum Counts	452,711	12,524	13,027	83,939
Filament Failure Rate	1 of 8	0 of 1	0 of 6	8 of 12

2.3.7 Initial development of the toroidal polymer spot loading technique

To better mimic the physical distribution of anion-exchange polymer achieved when using the bead loading technique, a method was developed to deposit small anion-exchange polymer spots on rhenium ionization filaments. The goal was to increase the amount of deposited anion-exchange polymer that interacts with the Pu sample while maintaining a concentrated ion source and minimizing the overall amount of polymer deposited onto rhenium filaments. The selected approach was to created small polymer disks on rhenium filaments by applying anion-exchange polymer in a small droplet of solvent. To keep the spot size on the order of anion-exchange resin beads (40–300 μm), the droplet volumes had to be on the order of nanoliters. This small volume precluded the use of standard pipettes to deposit the polymer-bearing droplet. Commercial devices capable of dispensing droplets on the nanoliter scale are available but are expensive. Prior to investing in a nanoliter dispenser device, we decided to test this concept using an inexpensive method. The "needle method" was developed and is described in section 2.2.8. Briefly, a nanoliter scale droplet is formed on the *outside* of a steel needle by plunging the needle into a polymer bearing solution, which is then deposited on a substrate by sweeping the needle across the surface. The substrates are coated with PVBC-DABCO prior to spot deposition. This underlayer serves two purposes. First, the PVBC-DABCO coating is hydrophobic, causing the deposited droplet to "bead up". This ensures that the deposited droplet remains small. Conditions that lead to the deposited droplet wetting the substrate result in a dispersed deposition of Pu extractive polymer. Second, this PVBC underlayer provides a coating to which the deposited polymer spot can be cross-linked, anchoring the spot to the surface. Thirty-five percent DABCO cross-linking was determining to be the minimum level of cross-linking required to prevent both spot dissolution and detachment from the coated filament

surface upon swelling in aqueous solutions. Fifty percent TEA converted PVBC was used because this was the minimum level of TEA conversion to cause phase separation of the polymer in chloroform within 48 h. (The synthesis of water soluble PVBC-TEA polymer is described in section 2.2.7.)

Spots created by the needle method were imaged and profiled with 3D SEM, described in section 2.2.12. Upon 3D-SEM investigation it was discovered that polymer spots created using the needle method were toroidal in shape, with a thick outer rim. This geometry is caused by a phenomenon known as the "coffee ring effect", where capillary forces in the drying droplet drive solute towards the edges [130]. We have defined the spot "thickness" as the maximum height of the toroidal ring. Spots cast from 15 wt% PVBC-TEA in water were found to be approximately 30–50 microns in thickness and between 200 and 500 µm in diameter. A 3D SEM image of a deposited spot can be seen in figure 2.23, and height profiles of two spots measured using 3D SEM can be seen in figure 2.24. A range of droplet sizes was studied, and the diameter range of 200 to 500 µm does not represent the natural error in this spotting method. Deposited polymer spots were hydrophilic, adhering aqueous droplets (demonstrated in figure 2.25). We refer to this bilayer film design comprising a hydrophobic base PVBC-DABCO film with a hydrophilic spot as the "hydrophilic well" design. This design aids in direct loading filaments, as aqueous samples will dry into the hydrophilic extractive polymer spots positioned at the ion optical center of filaments.

Fifteen rhenium filaments were prepared using the needle method and shipped to collaborators at SRNL for Pu loading and analysis. Toroidal spots with a thickness of 30–50 µm and diameters of 200–500 µm were found ubiquitously to cause filament failure upon heating in the SRNL TIMS system. The cause of these failures was unknown and was explored to

understand why rhenium filaments with toroidal spots deposited by the needle method resulted in high failure rates while anion-exchange resin beads with a diameter of 40 – 300 µm did not. These efforts are discussed in section 2.3.8.

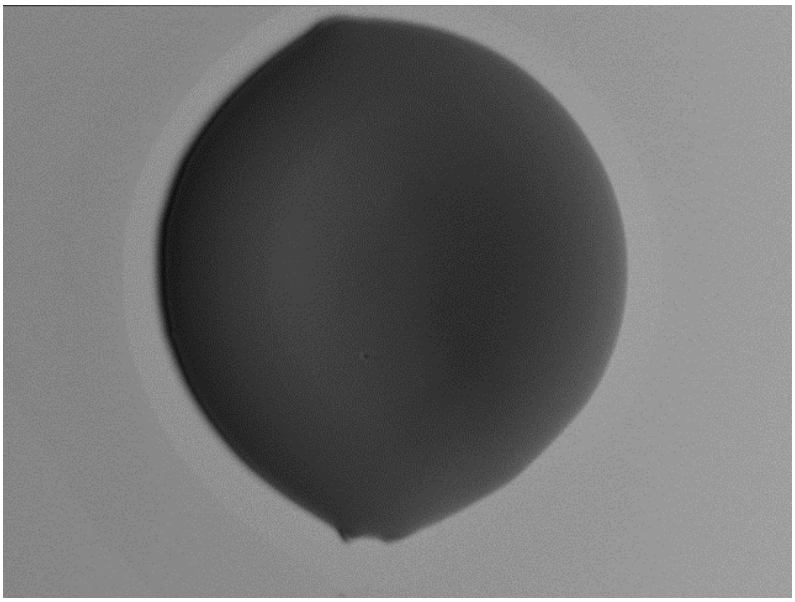

Figure 2.23 3D SEM image of a polymer spot deposited (15 wt.% polymer in water) by the needle method onto a PVBC-DABCO coated silicon wafer. Notice: the polymer spot is torroidal in shape, with a thick outer rim and thinner center region.

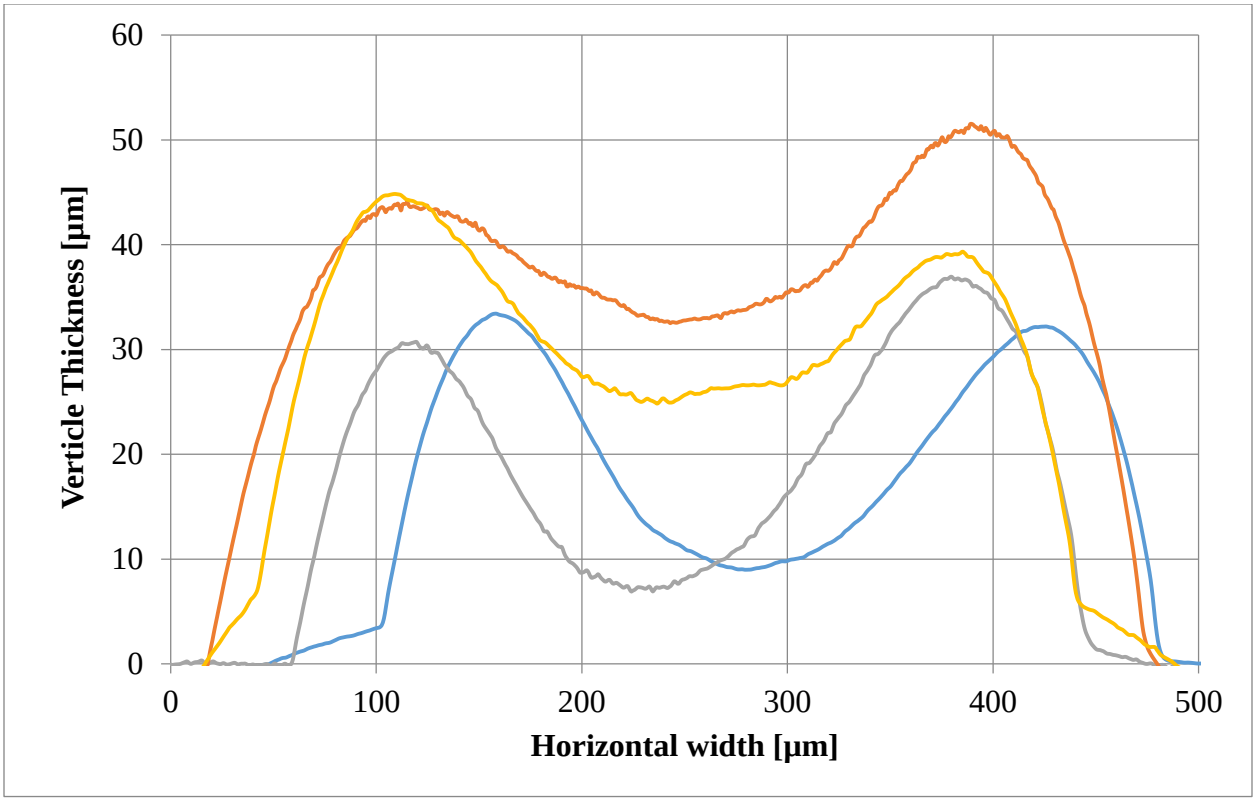

Figure 2.24 Height profiles of two spots measured using 3D SEM. Orangeand yellow lines represent the cross-section of a larger spot with a diameter of ~450 µm and maximum thickness of ~50 µm, while blue and grey represent the cross-sectional profile of a smaller spot with a diameter of ~400 and maximum thickness of ~37 µm.

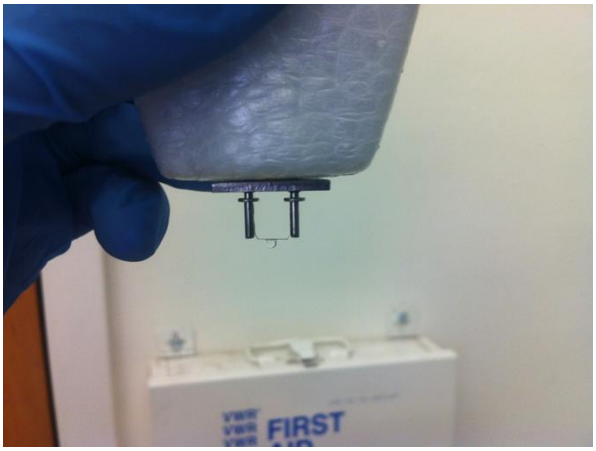

Figure 2.25 A droplet of water placed on a rhenium ribbon adheres to the hydrophilic quaternary amine-functionalized polymer spot prepared using the needle method. The hydrophobic PVBC-DABCO base film aids in preventing aqueous load solutions from spreading from the center of the filament, where the hydrophilic spot is located. When direct loading, the sample solution is dried down completely before loading filaments in the TIMS system, the Pu load solution dries into the hydrophilic spot, concentrating the Pu sample in the center of the filament on the TEA-functionalized toroidal spot.

2.3.8 Investigation of filament failure

Figure 2.26 shows optical microscope images of a dip coated rhenium filament before and after spotting using the needle method. The polymer mound can be seen clearly in the right image of 2.26 and is slightly thicker than the filament itself. The polymer spots were measured to be 30–50 µm thick, while rhenium filament material is reported by the manufacturer to be ~30 µm thick. No filament damage was found from inspection of 20 filaments prepared using the needle method. Of note: inspection by optical microscopy was performed at Clemson University prior to shipping filaments to SRNL for loading and analysis; therefore, damage incurred during

the shipping process could not be ruled out as a possible cause of filament failure described below.

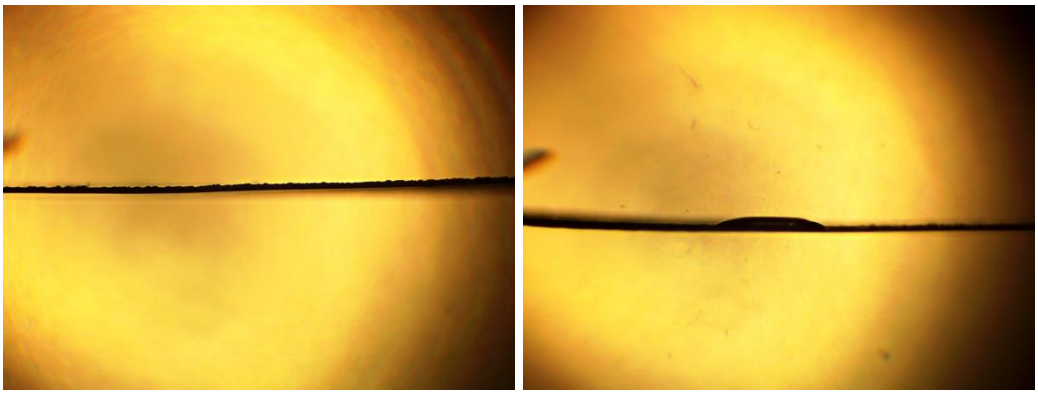

Figure 2.26 Rhenium filament before (left) and after (right) applying spots of PVBC-DABCO-TEA polymer using the needle method. No filament deformation is visible after spotting.

Eight filaments with PVBC-DABCO-TEA toroidal polymer spots were loaded with Pu by direct loading with a pipette and heated in the TIMS instrument; however, all filaments broke prior to the tuning step (during the initial ramp-up of filament current). The filaments broke in the middle, near the point of polymer deposition, as shown in Figure 2.27. Anecdotally, when the filaments break using the bead loading method, the point of failure is located near the spot weld connecting the filament to the mounting post. The expert TIMS operator at SRNL stated that filament failure occurring at the center of filaments was unusual, and the high rate of filament failure (100%) suggested that some detrimental interaction was occurring between the filament and the deposited spot. Damage incurred from using the needle method was not supported by optical microscopy, and filament failure occurring consistently at the center of filament seemed unlikely to be related to shipping related damage, as damage incurred from shaking the package

would result in random bending of the filament rather than consistent damage at the point of polymer deposition.

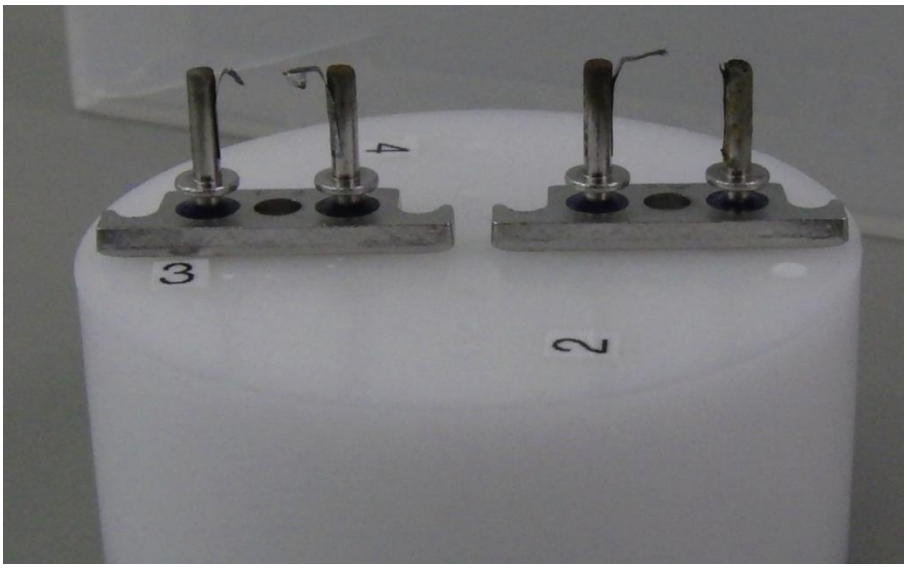

Figure 2.27 Image of filament showing break point. Dr. Charles Shick, Jr., the expert TIMS operator at SRNL, stated that breaks at the center of filaments are uncommon when bead loading. Rather, filament failure usually occurs near the weld locations on the mounting posts.

Two broken filaments were examined by SEM and SEM-EDS (procedure described in section 2.2.12) to assess the cause of breakage. Both filaments showed obvious signs of overheating (figure 2.28), and, therefore, it was suggested that a melting event occurred causing ultimate failure.

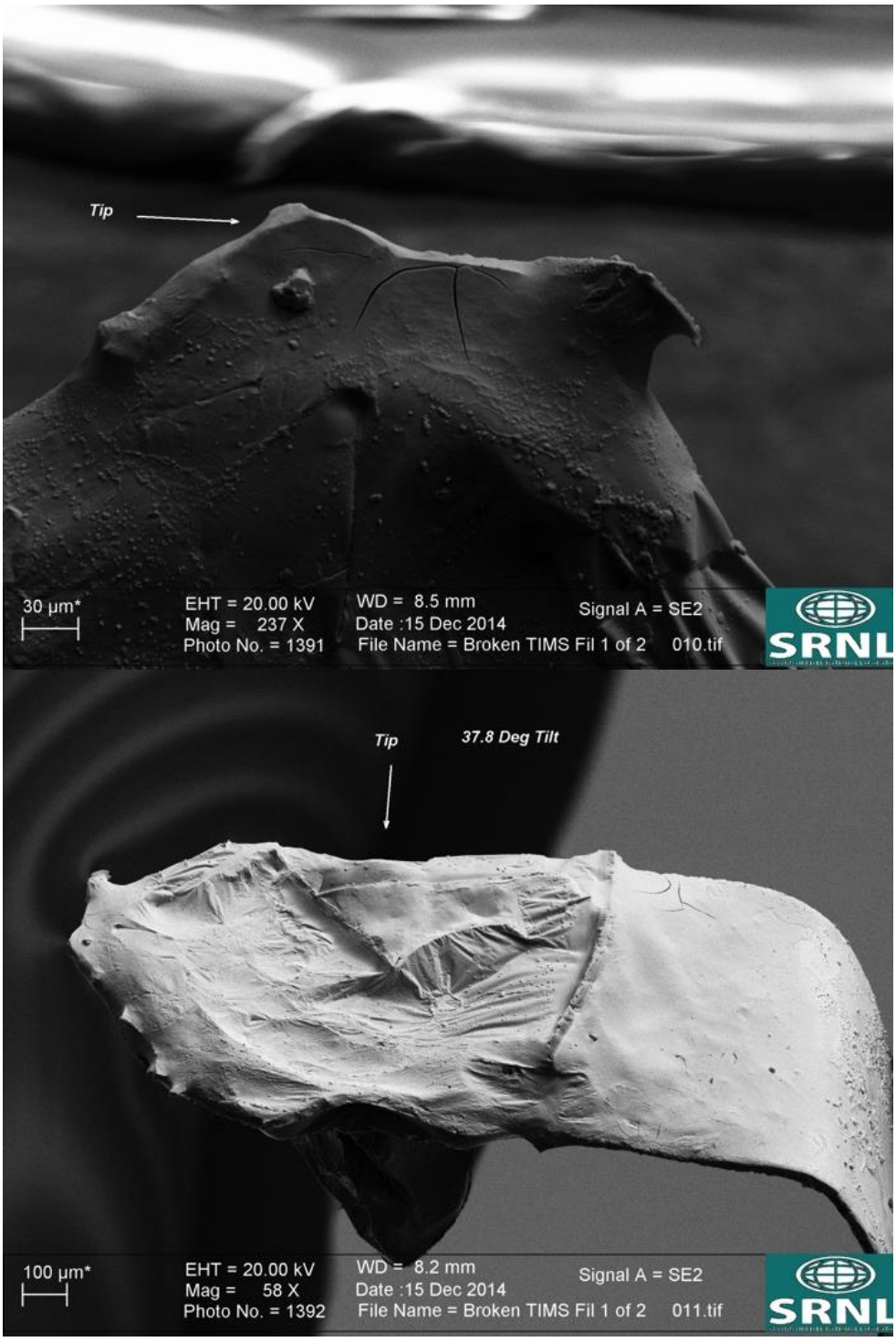

Figure 2.28 (Top) Rounded smooth termination indicates overheat-melt failure mode. (Bottom) Notice melted Re under filament.

Results shown in the secondary electron detector and Z contrast backscatter electron detector images (figure 2.29), elemental x-ray maps (figure 2.30), and EDS spectra (figure 2.31) all showed regions with elevated amounts of chlorine and carbon. In addition, figure 2.32 shows that Re had been vaporized and deposited onto the post, which is not to be expected given the high vaporization temperature of metallic rhenium (5630 °C). Based on this evidence, we hypothesized that chlorine from the polymer coating reacted with the Re filament to form ReClx compounds. Compared to Re, these ReClx compounds have much lower boiling points and decomposition temperatures (under 1000 °C). For example, $ReCl_5$ has been used in chemical vapor deposition chambers to form Re films. This may explain why Re was deposited on the posts and appeared to have melted.

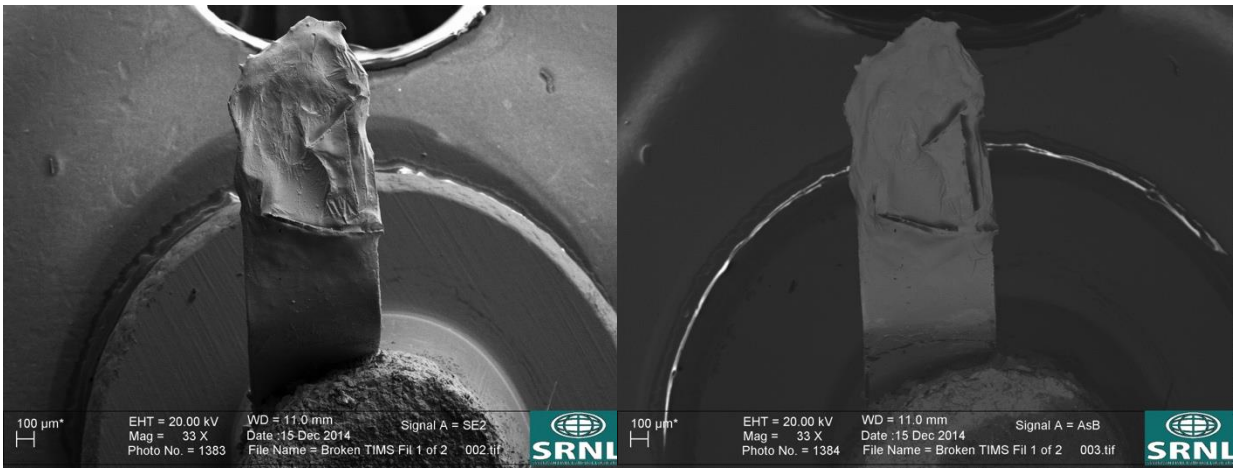

Figure 2.29 (Left) Secondary electron detector image. (Right) Z contrast backscatter electron detector image. The dark areas are related to low atomic weight species that produce lower levels of backscatter electrons. EDS analysis indicated these areas correlate with high levels of Cl and C.

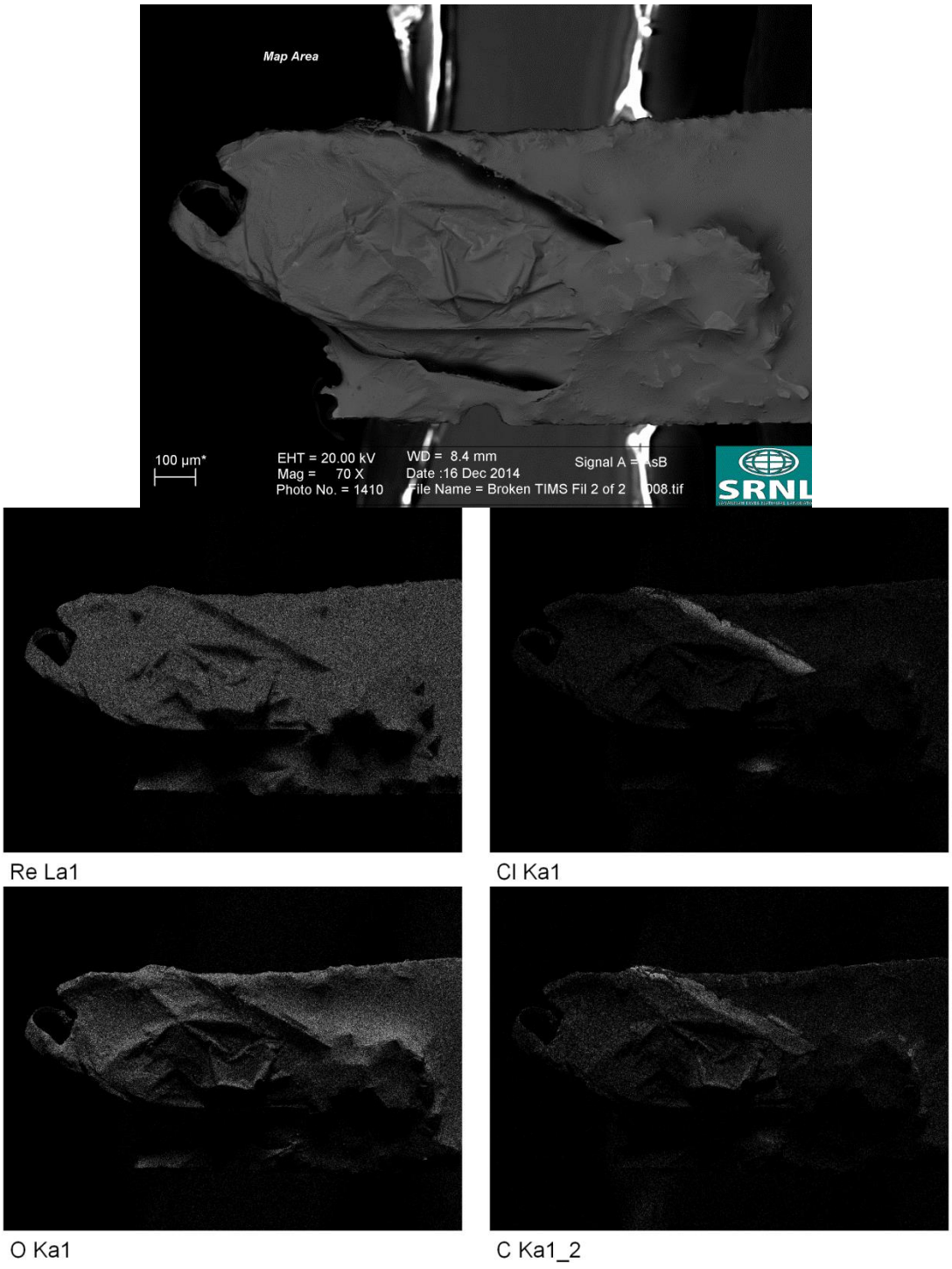

Figure 2.30 Elemental X-ray maps of fractured filaments.

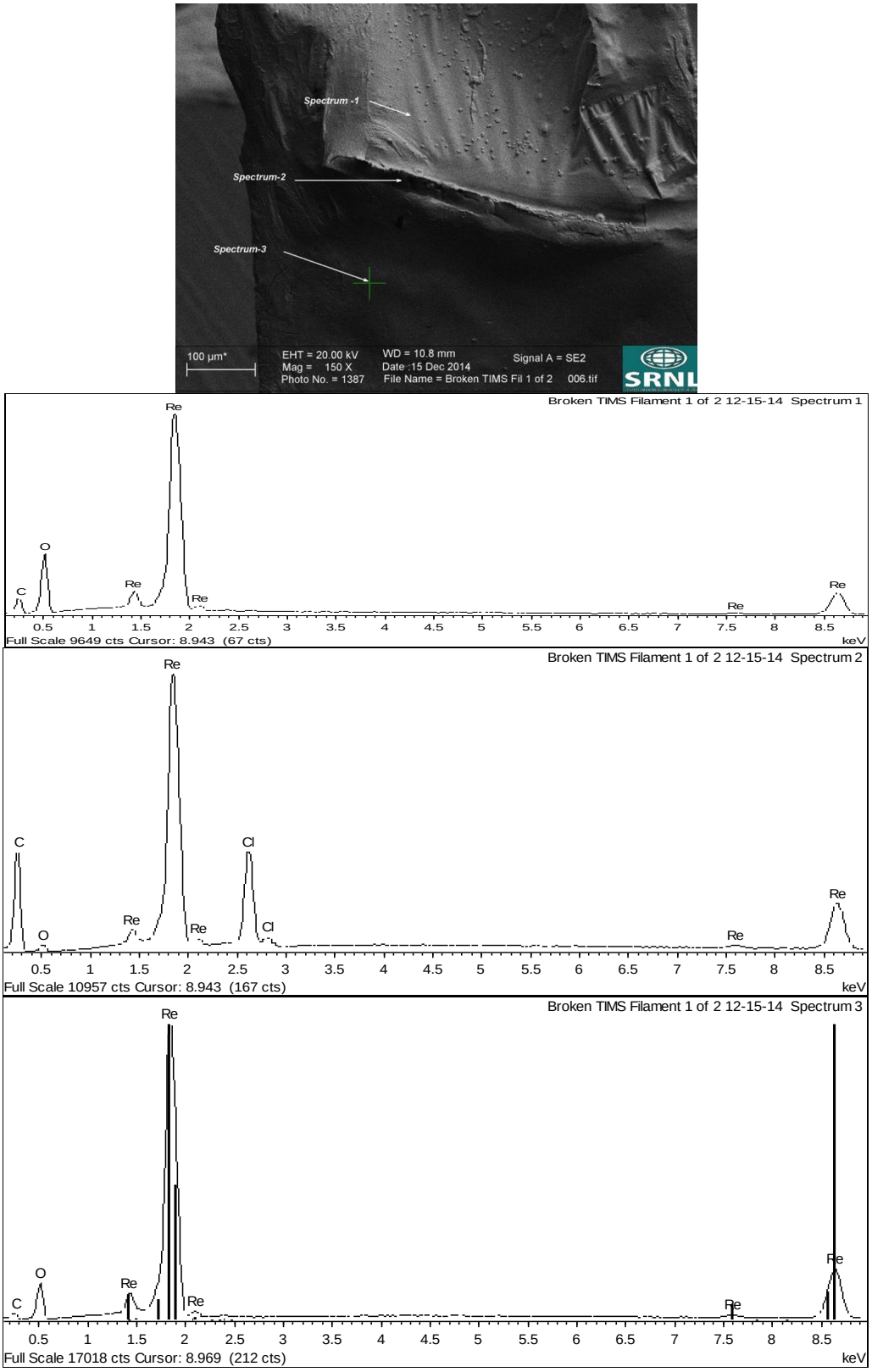

Figure 2.31 EDS spectra. Notice that spectrum-2 was taken in one of the backscatter dark areas and shows an elevated amount of Cl.

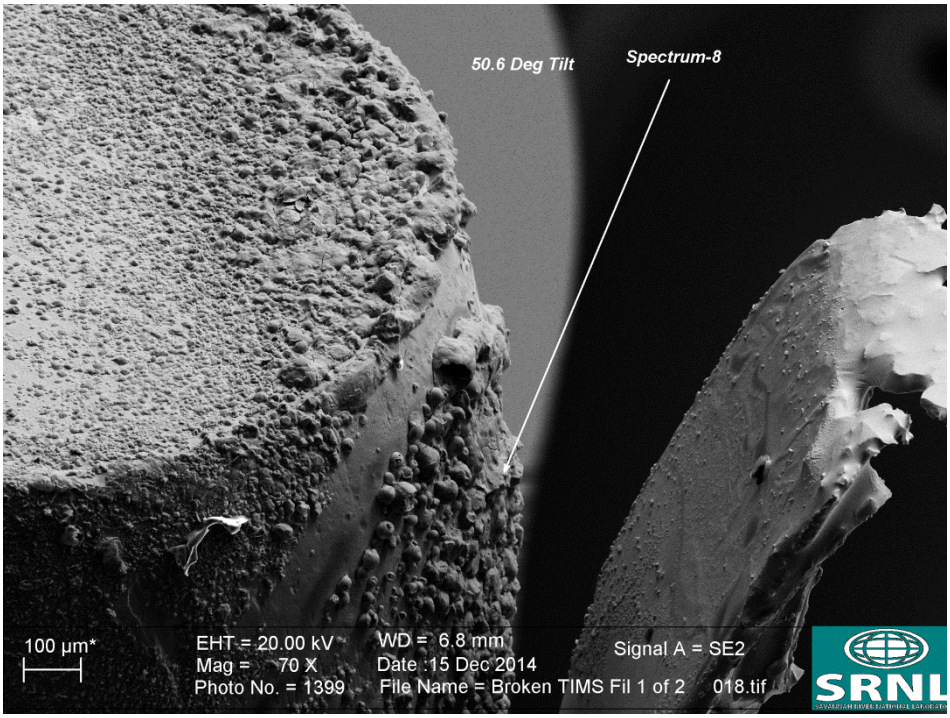

Figure 2.32 Image of post showing that Re was vaporized and deposited from the filament onto the post.

Based on these findings, it was hypothesized that reducing the amount of polymer (and thus chlorine) on the surface may reduce etching of the filament from formation, and subsequent melting/evaporation, of $ReCl_X$ species. In addition, as a precaution, from this point forward filaments were exchanged in person between Clemson and SRNL staff to prevent filament damage incurred during shipping. A method was also developed to investigate the efficacy of PVBC-DABCO-TEA polymer for TIMS sample loading and is described in section 2.3.9.

2.3.9 Development of the anion-exchange polymer fiber loading technique

The apparent detrimental interaction between PVBC-DABCO-TEA polymer and Re filaments (resulting in the formation of $ReCl_X$ species as described in section 2.3.8) led our group to develop a direct method to test the efficacy of this polymer chemistry for TIMS sample

loading by removing other potential variables. Although SEM and SEM-EDS analysis of failed filaments supported the hypothesis that $ReCl_X$ species were formed, resulting in melting and vaporization of the filament, it was unknown if the geometry of deposited spots promoted the creation of $ReCl_X$ species or resulted in other detrimental effects. It was hypothesized that the spotted filament design, placing the anion-exchange polymer in close proximity with filaments, would lead to greater interaction between the polymer and the filament surface than in the case of bead loading. This design was hypothesized to be beneficial, as more of the Pu sample would be in close proximity to the ionization surface than in the case of bead loading, providing greater opportunity for interaction with the ionization surface and, thus, leading to greater sample ionization. However, after discovery of the ubiquitous filament failure when using the toroidal polymer spot design, there was concern that this design may be flawed beyond $ReCl_X$ formation. Carbon forms a solid phase solution with rhenium at elevated temperatures and enbrittles the rhenium filaments. Rhenium filaments expand and sag when heated in the TIMS system, and there was concern that overly brittle filaments could break when heated due to stresses from expansion and sagging. Figure 2.33 shows an images of sagging filaments.

PVBC-DABCO-TEA fiber formation and sectioning, described in section 2.2.9, was seen as a simple means of producing anion-exchange material with physical dimensions similar, in part, to resin beads used in bead loading. By avoiding use of the needle method, and loading PVBC-DABCO-TEA in a method similar to that of beads, the effects of polymer chemistry could be isolated from geometric effects of the toroidal spots or potential damage incurred from deposition of the polymer. Additionally, fibers were created at Clemson and loaded onto filaments at SRNL, so shipping filaments was avoided. It was proposed that if PVBC-DABCO-

TEA fibers resulted in filament failure rates similar to when needle method spotting was used (section 2.3.7), then an alternative polymer would be investigated for sample loading.

Figure 2.33 Sagging filament assemblies imaged after heating to high temperatures (>1500 °C).

Fiber sections with a diameter of approximately 100 μm were selected for these analyses to maintain a concentrated ion source. Figure 2.10 shows an optical microscope image of a 100 μm diameter fiber (method of obtaining optical images of fibers is described in section 2.2.11). Fibers appeared non-porous at the magnifications studied and possessed a uniform diameter over lengths of several centimeters. Fibers were sectioned and loaded with 10 pg of Pu from 8 M nitric acid in a fashion that mimics the bead loading method used at SRNL (described in section 2.2.18 and 2.2.20). Pu uptake studies were conducted previously by our group using thin films

composed of TEA-quaternized-PVBC with the same level of DABCO cross-linking that was used in preparation of fibers [129] (also described in section 2.3.3). Figure 2.34 (left axis and solid bars) shows a comparison of ion production (total number of detected Pu atoms) between the standard SRNL bead loading method and the new fiber loading method. The average number of Pu counts detected using fibers was approximately 180% greater than the number of counts detected when using the standard bead loading method, given a 10 pg load of Pu in both cases. Figure 2.34 (right axis and round symbols) shows a comparison of average isotope ratios measured for NBL CRM Pu128 with fiber and bead loading. The average and standard deviation represent the values from six measurements for each loading technique. The standard deviation for isotope ratio measurements was decreased by 72% when fiber loading was used and the accuracy of the average measured isotope ratio was improved. An average deviation of 0.033% from the certified isotope ratio value of NBL CRM Pu128 was measured when fiber loading versus a deviation of 0.133% when bead loading. These findings are statistically significant. At a 99% confidence level (using a two-sample F-test, one-tail), the variance in measured isotopic ratio is larger when using bead loading versus fiber loading. At a 95% confidence level, the measured isotope ratios are unequal (using a two-sample t-test, two tails).

In addition to the accuracy of the isotope ratio measurement, the sample utilization performance also improved. At a 95% confidence level the average measured counts is greater using fiber loading versus bead loading with 10 pg of Pu (using a two-sample t-test, one-tail). The mechanism(s) leading to the observed improvements in ion production and the accuracy/precision of isotopic ratio measurements when using PVBC-DABCO-TEA fibers is not fully understood at this time, but we hypothesize that increased ionization efficiency is due to greater contact between the anion-exchange material and the ionization surface than is present in

the case of bead loading. These results are somewhat counterintuitive to the common notion within the TIMS community that ion sources must be "point-like", as fibers sections were 2.5 mm in length. The volume of fibers prepared and used in this study were approximately 0.02 mm^3. Bead diameters ranged from 150 to 300 µm (50 – 100 mesh), and 4 beads were loaded onto each filament relating to an overall resin volume of 0.007 to 0.057 mm^3 in the case of bead loading. The volume of fibers is within the range of resin loaded onto filaments; therefore, we do not believe increased ionization efficiency with fiber loading is related to the mass of carbonaceous material loaded onto filaments.

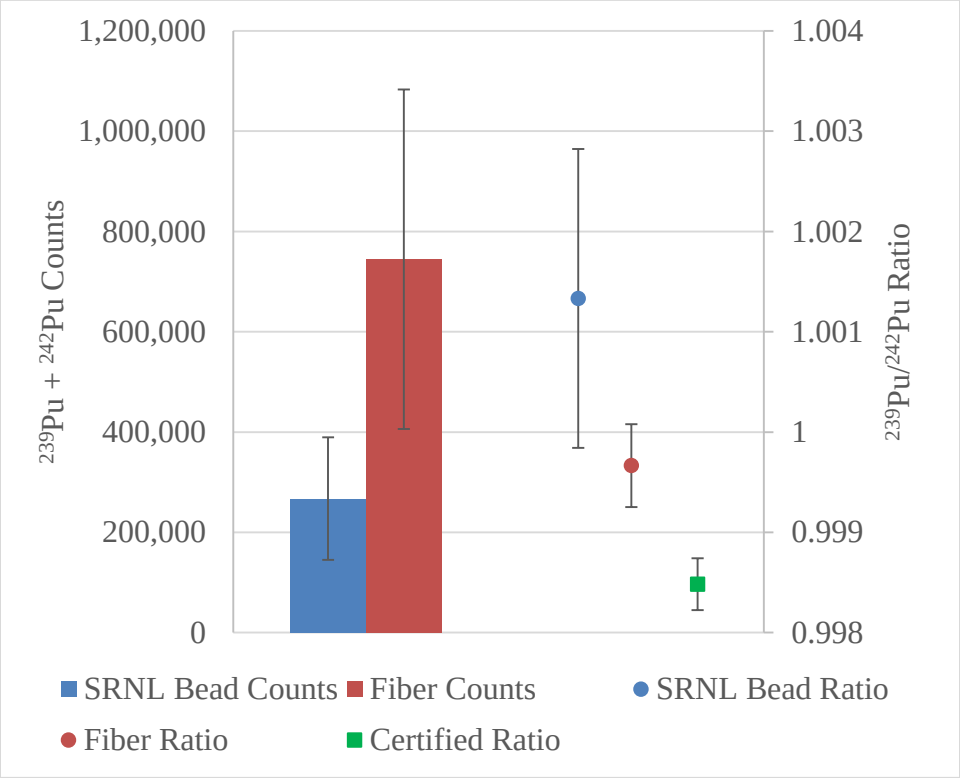

Figure 2.34 Comparison of the average ion yield and average isotope ratios obtained from the standard SRNL bead method and the fiber-based method using a 10 pg load of Pu. Average values are from six replicates and error bars represent 95% confidence intervals.

This study was undertaken, in part, to determine the efficacy of TEA-quaternized-PVBC as an ion-exchange material for TIMS loading. The method of fiber formation also has been applied successfully to quaternized- poly(2,2-dimethyl,1,4-phenylene oxide) and quaternized-poly(4-vinylpyridine). Fibers appear to be a versatile and simple platform for investigation of novel polymeric ion-exchange materials for TIMS sample loading. Delmore hypothesized that Pu must react chemically with carbon additives to effectively be converted to the carbide form.[96] If this hypothesis is true, then chemical properties of the polymer ligand, such as actinide binding energy or elemental content may have an effect on the propensity for carbide formation and hence ionization efficiency. The potential for fiber formation as a means to screen or design polymer chemistries for TIMS sample loading is discussed in the conclusions and recommendations section.

No filament failures occurred when loading fibers composed of PVBC-DABCO-TEA. This result suggested to our group that the high failure rate of toroidal polymer spots described in section 2.3.7 was likely to be associated with either the geometry of these spots or the method of depositing toroidal polymer spots. Although the PVBC-DABCO-TEA fiber loading technique was successful, surpassing the established bead loading method in terms of measurement sensitivity and the accuracy/precision of isotope ratio measurements, fiber loading does not improve TIMS sample loading in terms of difficulty. Fiber loading was actually viewed as being more difficult and time consuming than bead loading by the expert TIMS operator at SRNL. Fibers are difficult to handle and manipulate into place onto rhenium filaments. Additionally, fiber loading does not eliminate the need to manually handle anion-exchange materials loaded with radionuclides, as fibers were soaked in Pu bearing solutions before being manually glued into place on degassed rhenium filaments. Due to these drawbacks with fiber loading, our group

decided to reinvestigate the thin film loading strategy with the goals of creating a film on rhenium filaments that could be direct loaded by pipette and perform at a similar or better level than that of the bead loading method in terms of sensitivity and/or accuracy. These efforts are described in section 2.3.10.

2.3.10 Reinvestigation and refinement of the toroidal polymer spot loading technique

Positive results obtained through development of the anion-exchange polymer fiber loading technique suggested that successful sample loading with PVBC-DABCO-TEA could be achieved. It was concluded that the toroidal polymer spot architecture had contributed to the filament failures described in section 2.3.8, and that by manipulating the dimensions of toroidal polymer spots a direct-loadable film could be created that did not result in high rates of filament failure. This hypothesis was supported by observations made during the development of films with localized TEA-quaternization (described in section 2.3.6), where high rates of filament failure were encountered with thick films (~1 μm) but not with thin films (~120 nm). Similarly, it was hypothesized that the deposition of thinner spots, using the needle method, may reduce the rate of filament failure that was experienced with thicker spots (30–50 μm thick spots described in section 2.3.7 and 2.3.8).

Variable pressure 3D SEM and AFM were used to image and obtain height profiles of spots cast on PVBC-DABCO coated silicon and glass substrates respectively. Experimental methods for 3D-SEM analysis are described in section 2.2.12 and AFM analysis is described in section 2.2.13. The use of variable pressure SEM allowed the polymeric spots to be imaged without the addition of a conductive coating. AFM was used to image thinner spots (<7 μm in height due to limitations of the AFM) and determine spot thickness; however, complete imaging

of spots by AFM was not possible due to the small viewing window (100 × 100 μm) allowed by the AFM. Figure 2.23, acquired via SEM, showed that the deposited spots are toroidal in shape with a thick outer rim. This shape was found to be consistent with thinner spots as well; an image collected via AFM of the outer rim of a thin spot (~3 μm) can be seen in figure 2.35. Spot thickness was manipulated by altering the concentration of polymer in the aqueous deposition solution from 0.5 wt% to 15 wt% while maintaining a consistent droplet size. Figure 2.36 shows the relationship between polymer concentration and spot thickness acquired by AFM. The maximum height measureable by the AFM used in this study is 7 μm; therefore, thickness measurement of spots cast from >2.25 wt% polymer was not possible by AFM. The relationship shown in Figure 2.36 was used to estimate the thickness of spots with intermediate thicknesses (7–30 μm), which were difficult to profile by 3D SEM due to low levels of shading.

Rhenium filaments were degassed at SRNL and exchanged in person for toroidal PVBC-DABCO-TEA spot deposition at Clemson, followed by in person exchange back to SRNL staff. In-person filament exchanges were used as a precaution to avoid damage from shipping of delicate filaments. Spotted filaments were loaded with Pu by direct loading and analyzed on the TIMS system at SRNL. The first batch of spotted filaments tested on the SRNL TIMS system in this reinvestigation of the toroidal spot design was prepared by the needle method with a maximum rim height of 1.0–1.5 μm (deposited from an aqueous solution containing 0.5 wt% polymer). HNO_3 and an HCl were investigated as the direct loading matrix. Table 2.5 shows these data with comments from the SRNL TIMS expert. No filaments in this batch failed from breaking; however, 3 of the 5 filaments loaded from an HNO_3 matrix produced no Pu counts. It was theorized that the HNO_3 matrix corroded the rhenium filament, leading to toroidal spot detachment and sample loss. As was discussed in section 2.3.5, nitric acid aggressively corrodes

rhenium surfaces, even when these surfaces are coated with a hydrophobic PVBC-DABCO film. In contrast, Pu counts were measured from all samples loaded from an HCl matrix. An HCl direct loading matrix was used for all other investigations regarding the toroidal spot design.

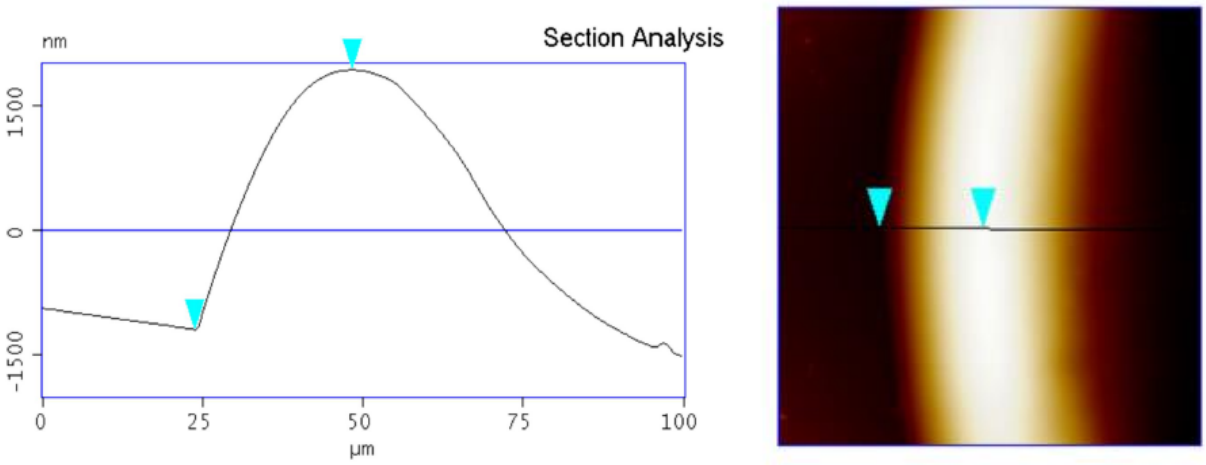

Figure 2.35 (left) AFM height profile and (right) height image (100 µm × 100 µm viewing window) of a toroidal PVBC-DABCO-TEA spot deposited on PVBC-DABCO coated glass with a maximum rim height of ~3 µm.

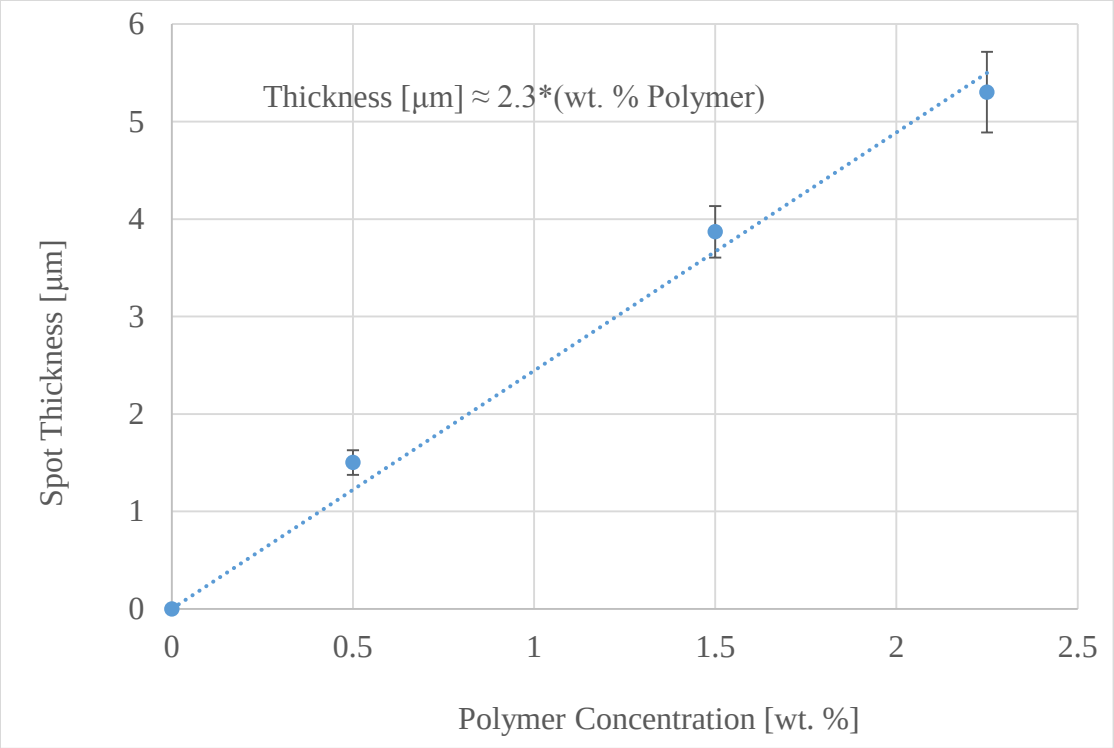

Figure 2.36 The relationship between polymer concentration in spotting solution and resulting polymer spot thickness (maximum); thicknesses determined by AFM measurements and the fitted relationship was used to estimate spot thickness for solutions with greater than 2.25 wt. % polymer.

Results from the first batch of filaments with toroidal spots confirmed our hypothesis that filament failure could be avoided with this design by reducing the quantity of polymer on the filament surface; however, filaments with 1.0–1.5 µm thick spots performed poorly in comparison to the bead loading method in terms of measurement sensitivity. These filaments only produced Pu ions for approximately 1 h, while beads produce ions for at least 4 h. Table 2.6 shows these data. It was proposed that slightly thicker toroidal spots might increase the duration of ion production and, therefore, measurement sensitivity, by extending the time for dissolution of the carbon into the rhenium filament.

Table 2.5 The performance of thin spots [1.0–1.5 μm] loaded from 8M HNO_3 and 9M HCl; sample losses experienced when loading from 8M HNO_3 led to the use of 9M HCl for all direct loading on thin film coated filaments. All filaments were loaded with 10 pg of NBL CRM Pu128.

Matrix	Total counts (Pu242 + Pu239)	Uncorrected Pu239/Pu242 ratio	Comments
8M HNO_3			No counts for Pu-242/Filament NOT BROKEN
8M HNO_3	18,550	1.002	Low counts but good agreement with certified value for Pu239/Pu242 ratio
8M HNO_3	46,140	0.993	Low counts but good agreement with certified value for Pu239/Pu242 ratio
8M HNO_3			No counts for Pu-242/Filament NOT BROKEN
8M HNO_3			No counts for Pu-242/Filament NOT BROKEN
9M HCl	44,400	0.998	Low counts but good agreement with certified value for Pu239/Pu242 ratio
9M HCl	8,132	1.012	Low counts but good agreement with certified value for Pu239/Pu242 ratio
9M HCl	73,580	1.001	Low counts but good agreement with certified value for Pu239/Pu242 ratio
9M HCl	842	0.987	Low counts but good agreement with certified value for Pu239/Pu242 ratio
9M HCl	249	0.742	Low counts and not good agreement with certified value for Pu239/Pu242 ratio

In an effort to increase the duration of ion production, the thickness of the toroidal anion-exchange spots was increased by 300% by increasing polymer concentration from 0.5 wt% to 1.5 wt% in the deposition solution and maintaining consistent volume of the deposited droplet. These thicker spots were found to produce ions for approximately 3 h on flat filaments, a proportional increase in duration of ion production; however, the total counts produced by these spots [3.0– .5 μm] was ~10 times that of the thinner spots [1.0–1.5 μm], reaching levels of ionization efficiency comparable to that of the resin bead method. These data are shown in table 2.6.

Up to this point in our investigations of toroidal spot design, all spots had been deposited on flat filaments. The efficacy of the dimpled filament geometry, described in use with the bead loading method in section 2.3.2, was explored in combinations with the toroidal spot design in an effort to further increase ionization efficiency. Toroidal anion-exchange polymer spots with a thickness of 3.0–4.5 μm were formed on dimpled filaments, resulting in a 25% increase in the duration of ion production (increased from 3 to 3.75 h) and a 43% increase in the average total counts compared to similar spots cast on flat filaments. Table 2.6 presents the results, which show that average sample utilization using dimpled filaments with 3.0–4.5 μm toroidal spots surpassed sample utilization afforded by the resin bead loading method. We submit that the increased ionization efficiency experienced with dimpled filaments is the result of a concave filament structure, similarly to that of the cavity sources. When the sample is loaded into the "pit" of a concave dimple, neutral gas atoms have opportunity to interact with the ionization surface after volatilization from the load region, resulting in higher ionization efficiencies. Dip-coating allowed for the formation of a thin polymer PVBC-DABCO underlayer on the complex geometry of dimpled filaments, a task that would not be possible with other film formation methods, such as spin-coating. Dimpled filaments also aid in direct sample loading as they allow for the sample to be placed in a cup-like substrate. In combination with the hydrophilic islands created by the bi-layer film design, direct loading an aqueous sample in a small region at the geometric center of a dimpled filament is much simpler and easier than other methods of direct loading. Due to the benefits of dimpled filaments they were used for the remainder of investigations within this study. In addition to improved measurement sensitivity, no filament failures were experienced over the course of analyzing 45 filaments with toroidal spots less than

4.5 µm thick, a significant improvement over the reported failure rate of ~25% with the bead loading method.

Table 2.6 A comparison of ion production from various toroidal spot designs and the established bead loading method given a 10 pg load of NBL CRM Pu128. Resin beads were loaded from an 8M HNO_3 matrix while all spotted filaments were direct loaded from a 9M HCl matrix.

	SRNL bead loading method	1.0 - 1.5 µm spots on flat filaments	3.0 - 4.5 µm spots on flat filaments	3.0 - 4.5 µm spots in dimpled filaments
	Total ^{239}Pu + ^{242}Pu Counts (Atoms) Detected			
Average	287,953	25,441	229,081	434,572
Standard Deviation	149,772	32,465	125,889	291,459
N trials	7	5	10	30
95% Confidence interval	110,952	28,457	78,027	104,297
Minimum Counts	45,125	249	51,342	58,650
Maximum Counts	452,711	73,580	428,100	1,179,000
Filament Failure Rate	1 of 8	0 of 5	0 of 10	0 of 30

In an effort to continue improving sample utilization provided by the toroidal spot design, anion-exchange spot thickness was increased by depositing with 2.25, 3.25, 5.0, and 10.0 wt% polymer solutions, relating to spot thicknesses of 4.5–6.8, 6.5 – 9.8, 10 – 15, and 20 – 30 µm respectively, in dimpled filaments. Figure 2.37 and table 2.7 shows TIMS data for these samples. Toroidal spots with a thickness of 20–30 µm provided the greatest levels of sample utilization, surpassing the sample utilization of the standard SRNL bead loading method by 175%. Additionally, no filament failures were experienced over the course of analyzing 65 filaments with toroidal spots.

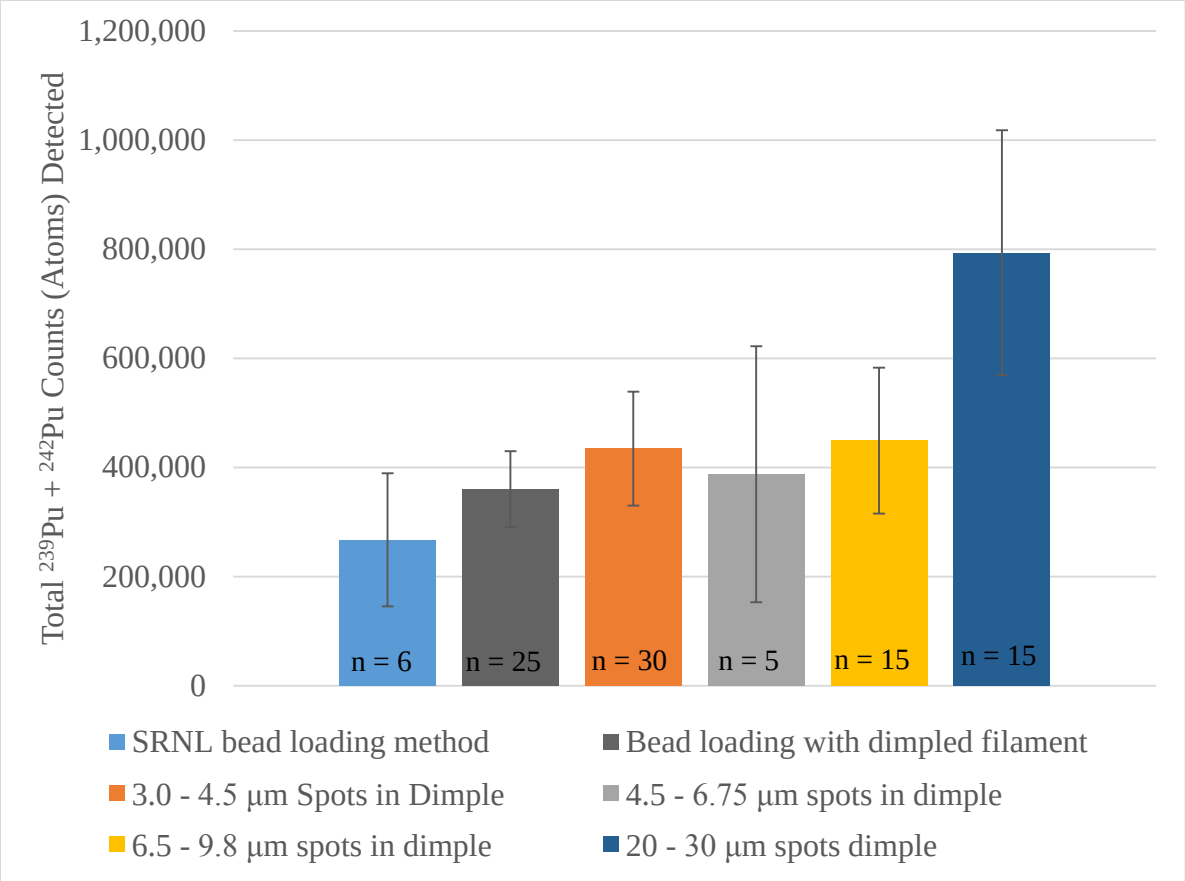

Figure 2.37 A comparison of the average sample utilization of various toroidal spot thicknesses in dimpled filaments and the established bead loading method (with V-Shaped filaments) given a 10 pg load of Pu; error bars represent 95% confidence intervals. Included is the sample utilization of the bead loading method with dimpled filaments. All spotted filaments were direct loaded from a 9M HCl matrix and beads were loaded with Pu from 8M HNO_3.

Figure 2.38 shows a comparison of uncorrected isotopic ratios obtained from thin film coated filaments and the established bead-loading method. All toroidal spotted filaments were within error of isotope ratios acquired using the standard bead loading method at 95% confidence level. These finding are in good agreement with the certified $^{239}Pu/^{242}Pu$ ratio for CRM Pu128 and indicate that the production of organic interferences is low for the toroidal spot loading

method with spot thicknesses below 30 µm. We believe that isotope ratios measured using the 4.5–6.8 µm thick toroidal spots deviated the greatest from the certified value of CRM Pu128 due to the low number of trials conducted at this spot thickness (5 trials).

Table 2.7 A comparison of the average sampled utilization of various toroidal spot thicknesses in dimpled filaments and the established bead loading method (with V-Shaped filaments) given a 10 pg load of Pu. Included is the sample utilization of the bead loading method with dimpled filaments. All spotted filaments were direct loaded from a 9M HCl matrix and beads were loaded with Pu from 8M HNO_3.

	SRNL bead loading method	Bead loading with dimpled filaments	3.0 - 4.5 µm Spots in Dimple	4.5 - 6.75 µm Spots in Dimple	6.5 - 9.8 µm Spots in Dimple	20 - 30 µm Spots in Dimple
	Total ^{239}Pu + ^{242}Pu Counts (Atoms) Detected					
Average	287,953	464,920	434,572	387,596	449,282	793,801
Standard Deviation	149,772	286,870	291,459	267,702	263,987	443,480
N Trials	7	20	30	5	15	15
95% Confidence Interval	110,952	125,726	104,297	234,651	133,596	224,432
Mininmum Counts	45,125	124,268	58,650	105,070	176,980	138,274
Maximum Counts	452,711	1,339,968	1,179,000	732,300	1,027,500	1,899,644
Failure Rate	1 of 8	0 of 20	0 of 30	0 of 5	0 of 15	0 of 15

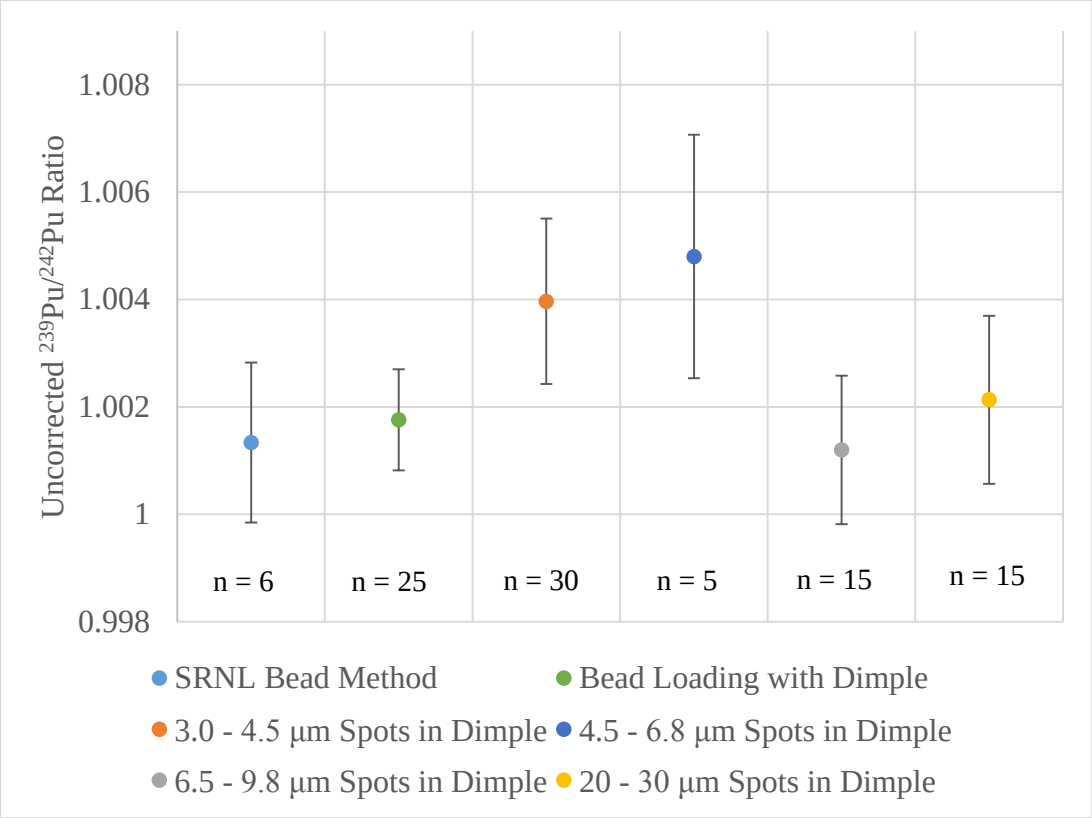

Figure 2.38 A comparison of isotopic ratios obtained from spotted filaments of various thicknesses with dimpled filaments and the SRNL bead method (with V-shaped filaments); error bars represent 95% confidence intervals. Also included is isotope ratio data obtained from the bead loading method with dimpled filament. The certified $^{239}Pu/^{242}Pu$ ratio for CRM Pu128 is 1.

The greater sample utilization achieved with the toroidal spot loading technique, compared to bead loading, may be due to increased transport and interaction with the ionization surface. Smith et al. [111] showed that a graphitic, actinide-bearing residue remains on filaments after heating beads, indicating that incomplete dissolution of the anion-exchange material into rhenium filaments occurs in the case of bead loading. Carbon is understood to be soluble in rhenium at elevated temperatures [108]. It was hypothesized within our group that more complete dissolution of anion-exchange material, and thus sample transport to the ionization

surface, could be achieved with a thin film design through optimization of film thickness. One reason for selecting an ion-exchange polymer is that Delmore [96] hypothesized, after work on the micro ion source program at Idaho National Laboratory, that the sample species must react chemically with carbon additives to effectively be converted to the carbide form. Conversion of the Pu sample to the carbide form is believed to increase ionization efficiency by stabilizing the sample on the ionization surface to higher temperatures, resulting in a greater proportion of ions being emitted from the surface upon volatilization [4]. We submit that increasing the thickness of toroidal spots to 20 -30 μm improved sample utilization by promoting the formation of Pu-carbides through higher Pu/C ratios. It is now evident that there must be a balance between minimizing carbon so that sample transport to the ionization surface can occur and maximizing carbon so that the formation of Pu-carbides is promoted. Therefore, an optimum spot thickness exists that balances these two competing phenomena. Additionally, the integrity of the filament must be maintained, as it appears there is a limit at which the filament fails due to either high carbon loading or reaction with species such as Cl. We would have continued to investigate the role of spot thickness in an effort to find this optimal value, but project funding ended. Future directions for this study are discussed in the conclusions and recommendations section.

2.4 Conclusions

Three improvements to sample loading procedures for TIMS analysis were achieved in this study. Firstly, a new filament geometry, the dimple, was developed and found to improve sample utilization when using the bead loading method. Additionally, sample loss was suppressed markedly through the use of dimpled filaments. Dimples facilitate sample loading by aiding in sample alignment and providing a well-like substrate to deposit samples. Finally, dimples limit the migration of beads on the filament surface, reducing the need for refocusing during analysis. Further investigation is needed to determine the influence of dimple dimensions on sample utilization.

Secondly, a general method for the formation of anion-exchange polymer fibers was developed using equipment found in most laboratories. Fibers composed of TEA-quaternized PVBC with DABCO cross-linking were found to outperform anion-exchange beads in terms of ion production and the accuracy/precision of isotope ratio measurements. Further investigation is needed to determine the mechanism(s) responsible for these improvements. Fiber formation can be applied to a variety of anion-exchange polymers, and offers a convenient and versatile platform to investigate novel polymer chemistries for TIMS sample loading.

Thirdly, a sample loading strategy based on polymer thin-film coatings was developed that surpasses ionization efficiencies afforded by the bead loading method. The coating simplifies sample loading by enabling direct loading in the geometric center of filaments. Coated filaments also eliminate sample loss, a problem often encountered when employing the bead loading strategy. Although preparation of coated filaments requires a two-step process, the thin film design allows for automated bulk production of pre-coated, analysis-ready filaments. This capability is a major advancement over the bead loading method and other methods that rely on

the material being submerged in the sample bearing solution before being individually manipulated and affixed to the filament. In addition, as will be shown in Chapter 3, applying a thin polymer underlayer coating is effective for preventing rhenium filament oxidation and increasing shelf-life.

A quaternary amine-bearing polymer was used in this study; however, the general methodology of polymer thin-film and spot production can be extended to other polymer and ligand systems. The level of improvement (over the bead loading method), in terms of sample utilization when fiber loading (180%) or thin film loading (175%), is greater than that reported for other methods of TIMS sample loading currently under development, such as the porous ion emitter (PIE) design (154%) [131]. This finding illuminates the importance of anion-exchange material design in the development of improved sample loading techniques for TIMS. We hypothesize that that PIE design is limited by poor transport of actinide species into the depth of the porous structure. Similarly to the shell theory mentioned previously, it is likely that small quantities of actinides are deposited near the outside of anion-exchange polymer filled pores.

CHAPTER THREE

CHARACTERIZATION OF RHENIUM IONIZATION FILAMENT SURFACE AGING AND EFFECTS OF OXIDATION

3.1 Introduction

Rhenium has been used widely as an ionization surface in thermal ionization mass spectrometry (TIMS) for isotopic analysis of Pu [125, 132]. Rhenium is the preferred material in these analyses for its high work function and melting point that is well above ionization temperatures for Pu [133]. Rhenium also has been employed as an ionization surface for a variety of other analytes [36, 54, 65, 66, 134]. The use of rhenium in other high-temperature applications has been limited by its oxidation characteristics [135]. It readily oxidizes above 600 °C when exposed to atmospheric oxygen and water vapor [136, 137]. High vacuum, thus low oxygen partial pressure, environments produced in TIMS systems are what enable the successful use of rhenium as a thermal ionization filament. Despite its susceptibility to oxidation and terrestrial scarcity, rhenium has remained an important material in the production of turbine blades[138], catalysts[139], and heating elements[140]; consequently, rhenium has been the subject of scientific investigations for many decades[141-149]. Despite these efforts, little is known about the chemical identities of species involved in catalytic[150] and surface ionization mechanisms[4, 110] due to the challenges associated with *in-situ* analysis.

Over decades of use in TIMS systems, various pretreatment methods for rhenium filaments have been developed to improve ionization efficiency [109, 134, 151, 152]. In cases of Pu analyses, these treatments can include carburization and degassing. Many reactions take place on the hot filament surface during these analyses. Reactions that promote the production of

atomic ions (Pu^+) are favored for ultra-low-level isotopic measurements of Pu, while those that promote the creation of oxide species (PuO^+ and PuO_2^+) are undesired due to the introduction of error based on the isotopic composition of natural oxygen.

Carburization of rhenium filaments has been shown to increase overall efficiency (atoms detected to atoms loaded, a.k.a. sample utilization) for Pu by up to an order of magnitude, and involves the dissolution of carbon into filaments through exposure to a carbon source, such as benzene vapor, at high temperatures [106]. Carburization is believed to positively impact Pu sample utilization (i.e., generation of Pu^+) by increasing the work function of rhenium [125] and acting as a reducing agent, suppressing the formation of oxide species [106]. The presence of carbon may also lead to the formation of actinide-carbides [106] that have a decreased propensity for oxidation [134] and stabilize the sample on the filament surface to higher temperatures, improving ionization efficiency upon dissociation to atomic ions [4]. Pu oxidation can occur when the C/Pu ratio is low [103] or when oxygen containing species are present on the filament [153].

The most common filament pretreatment method is referred to as “degassing” or “outgassing” and is performed prior to sample loading and analysis. Degassing involves resistively heating the filaments under high vacuum for a specified duration of time. Degassing generally is performed to reduce isobaric interferences and background signals that arise from contaminants within the rhenium filaments [127, 154]. Filament contaminants, such as hydrocarbons, uranium [155], and alkali elements [156], are volatilized or decomposed during the degassing process due to the high temperature and ultralow pressure. Studies have sought to optimize this process by monitoring the background signals of particular contaminants produced by blank rhenium filaments after various degassing conditions[155]. Degassing also volatilizes

rhenium-oxides that may be present on filament surfaces and alters surface features, such as grain boundaries [126] and grain sizes, as recrystallization of rhenium occurs around 1400-1600 °C [157].

The oxidation behavior of polycrystalline rhenium surfaces is complex due in part to the large number of oxidation states exhibited by rhenium[158], shifts in O-Re binding energy arising from non-local interactions with neighboring oxides[159, 160], and the propensity for high energy anisotropic planes of the hexagonal close packed surface to undergo oxygen-induced meta-stable morphological transformations[161, 162]. The binary oxides of rhenium at near ambient pressures are ReO_4, Re_2O_7, ReO_3, and ReO_2 containing rhenium in the VIII, VII, VI, and IV oxidation states. The vaporization temperatures of these oxides are reported to be 220, 362, 614, and 1362°C. [163] ReO_3 is reported to undergo disproportionation to ReO_2 and Re_2O_7 between 400 and 537°C, and ReO_2 disproportionates to Re metal and Re_2O_7 between 850 and 1077°C[164]. Filament currents used for resistive heating during degassing are often similar to those used during analysis to ensure that volatile compounds released at sample ionization temperatures are driven from the filaments prior to sample loading. In the case of Pu analyses, it can be expected that filament temperatures reached during degassing are >1500°C[99, 106, 154].

The motivation for this work was to determine a “shelf life” for degassed rhenium filaments. Excessive filament aging post-degassing has been observed anecdotally by SRNL staff to reduce sample utilization of Pu and decrease the precision of isotopic measurements. Protocols have been developed to avoid the use of overly aged filaments; however, studies regarding the effects of aging on filament conditions, and the ramifications on TIMS performance, are sparse in the literature. Although the viewpoint that filament aging negatively impacts TIMS analyses was anecdotal, the consistency and frequency of this observation across the TIMS community

suggested to our group that it warranted further investigation. Additionally, methods and storage conditions that may limit the effects of atmospheric aging were investigated in an effort to extend the "shelf life" of degassed filaments. It is well known that TIMS sample preparations are generally difficult, time-consuming, and costly[109]. Extending the shelf-life of rhenium filaments post-degassing could reduce the time associated with TIMS analysis by enabling bulk production of degassed rhenium filaments, thus, improving sample throughput and expanding the general utility and feasibility of TIMS analyses. The effects and mechanisms involved in long-term aging of polycrystalline rhenium surfaces must be understood to achieve these goals rationally.

3.2 Experimental

3.2.1 Materials

The following materials were obtained from Sigma-Aldrich and used as-received: chloroform (Reagent Plus® ≥ 99.8% with 0.5-1.0% ethanol as stabilizer, CAS# 67-66-3) and poly(vinylbenzyl chloride) (PVBC), 60/40 mixture of 3- and 4- isomers (CAS# 121961-20-4). Desiccant (t.h.e. ® desiccant 8 mesh non-indicating silica gel, CAS# 63231-67-4), high vacuum grease (Dow Corning, silicone compound), and sodium chloride (BDH VWR analytical ACS, CAS# 7647-14-5) were used as received from VWR. Nitric acid (Optima® grade for ultra-trace elemental analysis, CAS# 7697-37-2, 7732-18-5) and xylenes (histological grade, CAS# 1330-20-7, 100-41-4) were obtained from Fisher Scientific and used as received. Anion-exchange resin beads were obtained from Bio-Rad (AG® 1-X2 Anion-exchange Resin, analytical grade, 50–100 mesh, chloride form). Collodion solution (flexible, CAS# 60-29-7, 9004-70-0, 8001-79-4, 76-22-2, 64-17-5) was purchased from J.T. Baker. Pu solutions were prepared from a dilution of a primary standard containing New Brunswick Laboratory (NBL) certified reference material (CRM) 128 with a 1:1 atom ratio for $^{239}Pu/^{242}Pu$. Rhenium ribbons were zone-refined rhenium (minimum of 4 zone-refinement passes; 99.999% Re purity) from H. Cross Company (0.762 mm × 0.030 mm). Deionized (DI) water with a resistance of 18.2 MΩ was prepared in-house from distilled water that was passed through a Milli-Q water purification system (EMD-Millipore).

3.2.2 Degassing and carburization of rhenium filaments

Rhenium strips were cut (0.762 mm × 0.030 mm × 15.9 mm) and spot-welded onto posts for electrical heating at SRNL. Degassing was performed in a vacuum chamber at a pressure of around 10^{-5} Pa. Section 2.2.2 describes the filament degassing procedure used when no

carburization was performed. In cases where carburization was performed, filaments were incrementally heated to 2.8 Amps following the same heating regime as degassed filaments, with the exception of a final 2.5 to 2.8 Amp step increase. After two 15 min heating periods at 2.8 Amps, the turbo pump gate valve was closed and xylene vapor was introduced to the vacuum system until a pressure of ~60 Pa was reached inside the degassing chamber. Filaments were then subjected to a 15 min heating cycle at 2.8 Amps in the presence of xylene vapor. After exposure to xylene, the chamber was roughed out (with a roughening pump) before the turbo pump gate valve was reopened. Carburized filaments were allowed to cool under vacuum at 0 Amps for at least 2 h. Pyrometry was used to approximate filament temperatures at the conditions used for degassing and carburization. 2.8 and 3.0 Amps of filament current were found to correspond to filament temperatures of approximately 1360 and 1455 °C. In cases where bead loading was performed, filaments were crimped into "dimple" geometries before degassing to aid in sample loading. Flat filaments were used for SEM investigations involving aging under dry and humid conditions.

3.2.3 Filament aging under atmospheric conditions

Degassed (no carburization) and carburized filaments were prepared at SRNL and delivered to Clemson approximately 1 week after removal from high vacuum (filaments were sent by mail). After removing ribbons from mounts and securing to SEM grids, ribbons were allowed to age in covered polystyrene petri dishes under atmospheric conditions for up to 3 months after preparation. Samples were covered to prevent dust build-up.

3.2.4 Filament aging under controlled conditions

Degassed (no carburization) and carburized filaments were prepared at SRNL and delivered to Clemson on the same day of removal from high vacuum. After removing ribbons from mounts and securing to SEM grids with carbon tape, filaments were stored under dry and humid conditions and monitored intermittently by SEM for up to 79 days. Dry conditions were maintained by storing filaments in a 2.4 L glass desiccator filled with 250 g of silica gel desiccant (~13% relative humidity measured with an Extech 445814 hygro-thermometer), and humid conditions were maintained by storing filaments in a desiccator filled with saturated aqueous NaCl solution (relative humidity of ~75% [165]); both desiccators were sealed with high vacuum grease.

3.2.5 Thin polymer film formation

After degassing, filament assemblies were dip-coated from solutions of PVBC in chloroform. Film thickness depends on polymer concentration and withdrawal rate[123]. To produce a film with a thickness of approximately 120 nm, the substrate was withdrawn from a 2 wt% PVBC solution at a withdrawal rate of 340 mm/min using a Qualtecs Product Industry QPI-128 dip coater. Nominal film thicknesses were determined with multi-angle ellipsometry using silicon substrates as surrogate substrates for rhenium filaments.

3.2.6 Determination of film thicknesses

Film thicknesses were measured by multi-angle, single wavelength ellipsometry (Beaglehole Instruments, Picometer) as described in section 2.2.10.

3.2.7 Atomic force microscopy

Atomic force microscopy (AFM) images were obtained using a Bioscope AFM (Bruker, Inc.) with NanoScope III A controller as described in section 2.2.13.

3.2.8 SEM/SEM-Raman/SEM-Energy Dispersive X-ray Spectroscopy/Electron Back-Scatter Diffraction

SEM imaging performed on a Hitachi S4800 High Resolution SEM at Clemson University. Ribbons were removed from mounts used for degassing and secured to SEM grids with carbon tape. SEM-Raman and SEM energy dispersive X-ray spectroscopy (SEM/EDS) were performed at SRNL. A 785 nm laser and 30 s acquisition time were used for Raman analysis. SEM/EDS also was performed at Clemson University on a Hitachi SU6600 Variable Pressure SEM under high vacuum. Electron back-scatter diffraction (EBSD) mapping was performed at Clemson University on a nanoDUE'T double beam microscope NB5000.

3.2.9 SEM imaging for surface coverage determination and image processing

A Hitachi SU-6600 SEM was used for this study and a consistent magnification of 600x was used for all processed images. Crystallites with areas less than 0.1 μm^2 were excluded from counting to prevent the misidentification of stray pixels as crystallites. Images were processed with ImageJ version 1.50i to determine the average particle size, particle count, and percent surface coverage of crystallites. Image processing was performed by first converting images to black and white based on a brightness threshold. Crystallites generally appeared as bright spots under SEM illumination. Images were further processed individually to decrease the brightness of non-crystallite features, as occasionally grain boundaries and defect sites were similar in

brightness to crystallites. Finally, the ImageJ *Analyze Particles* tool was used with the following settings: size [μm^2] of 0.1 – infinity and circularity of 0.00 – 1.00.

3.2.10 TIMS analyses

A batch of 17 filaments was degassed and aged prior to sample loading using the methods described in sections 3.2.2 and 3.2.4. Fourteen of the filaments were sent to SRNL for TIMS measurements and three were kept at Clemson University for characterization. Quantification of the level of oxide growth (as described in section 3.2.9) was performed on the three Re filaments at Clemson University within 1 week of the TIMS analyses performed using the 14 filaments that were sent to SRNL. The bead loading method was used for these analyses. Briefly, four anion-exchange resin beads were contacted in 50 μL of 8 M HNO_3 containing 10 pg of NBL CRM Pu-128. Beads were submerged in solution and agitated using a Tekmar VSR-S10 shaker for a minimum of 4 h before being removed and glued to filaments using 10 μL flexible collodion solution. Analyses using freshly degassed filaments followed the same sample loading procedure and instrument methodology as analyses using aged filaments. After degassing, "fresh filaments" were stored under vacuum until directly prior to sample loading and analysis.

3.3 Results and discussion

3.3.1 AFM analysis of degassed filaments aged under atmospheric conditions

Zone-refined flat rhenium ribbon was cut and spot-welded onto posts for electrical resistance heating at SRNL. In this study, degassing parameters are based upon those used at SRNL for the isotopic analysis of ultra-low-level samples of Pu. Figure 3.1 shows images collected by AFM of a polycrystalline rhenium surface before and shortly after degassing. Prior to degassing, rhenium surfaces were found to be rough and possessed a variety of morphological features including surface ridges, mounds, and ill-defined grain boundaries, seen in figure 3.1a. The extent of atmospheric exposure experienced by these samples prior to degassing is unknown. Figure 1b shows the rhenium surface shortly after degassing (within 2 days of degassing). Morphological features witnessed prior to degassing (figure 3.1a) were absent; surfaces had comparatively smooth grain surfaces and clearly defined, well-formed grain boundaries. These surfaces were monitored intermittently over the course of 1 month of aging under atmospheric conditions after degassing, during which the in-growth of surface protrusions was detected via AFM (figure 3.2). The size and coverage of the protrusions were found to be grain dependent, making direct measurements of temporal growth by AFM difficult.

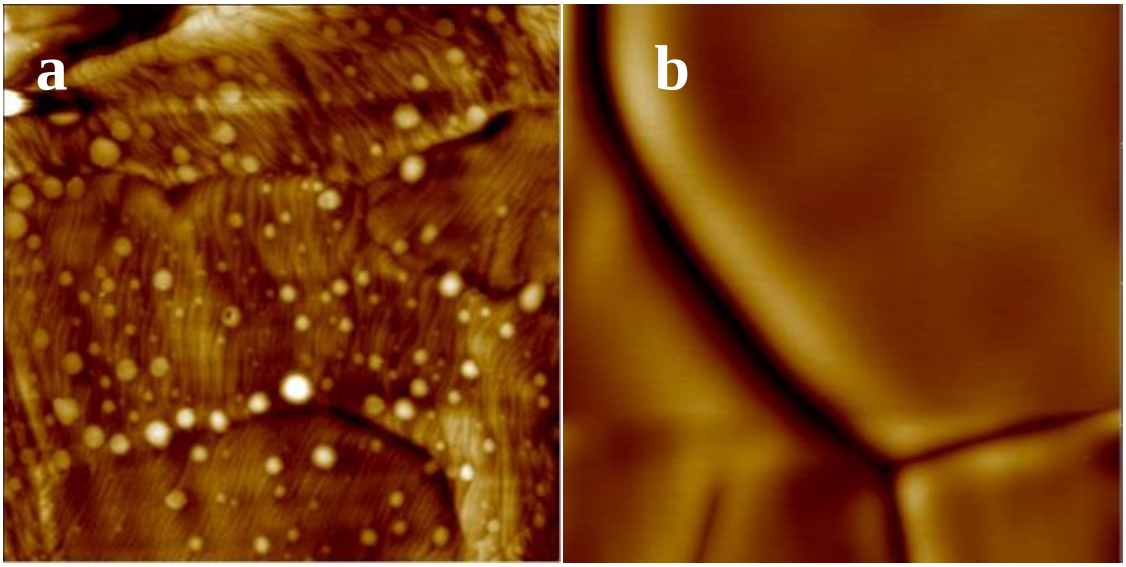

Figure 3.1. AFM images of rhenium surface (a) before degassing and (b) after degassing (<1 week atmospheric exposure). Scale is 10 μm × 10 μm. Height scale is 200 nm for image (a) and 250 nm for image (b).

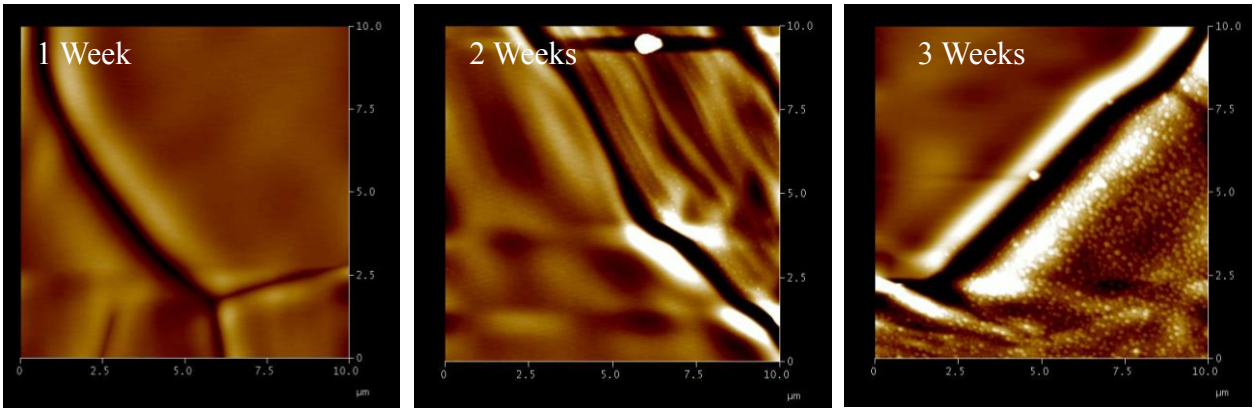

Figure 3.2 Ingrowth of surface protrusions detected by AFM over the course of 1 month of atmospheric exposure. Notice the grain dependency of surface protrusions. Scale is 10 μm × 10 μm. Height scale is 250 nm for all images.

3.3.2 SEM imaging of rhenium filaments aged under atmospheric conditions

Grain dependent growth of surface protrusions was supported with observations made by SEM and can be seen in figure 3.3a. After approximately 2 weeks of atmospheric exposure, densely covered grains were found that were surrounded by relatively bare, protrusion-free grains. Upon closer inspection with SEM, these surface protrusions, which appeared as lumps or mounds on the AFM due to broadening from probe artifacts, were found to be crystallites (figure 3.3b).

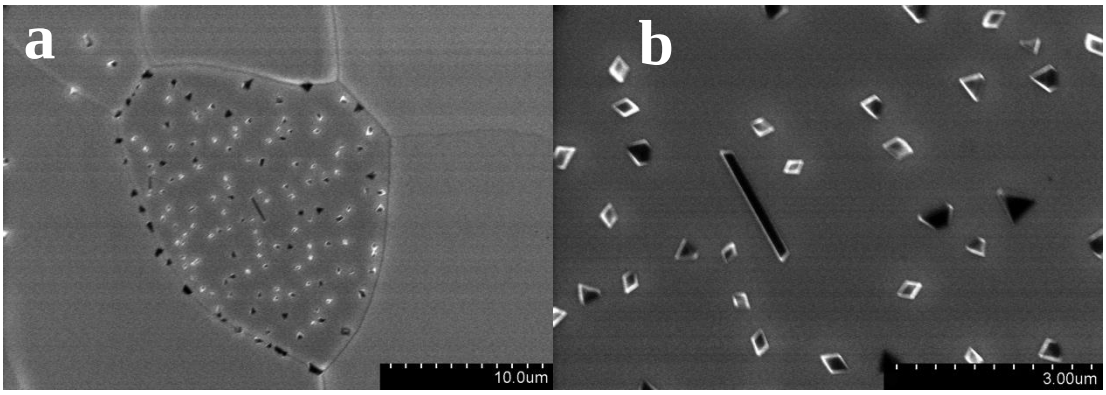

Figure 3.3 SEM images of polycrystalline rhenium filament surface after approximately 2 weeks of atmospheric exposure: (a) In-growth of surface protrusions was found to be grain dependent. (b) Surface protrusions were found to be crystallites.

After longer periods of atmospheric exposure (approximately 5 weeks), significant crystallite growth was found on most surface grains; however, crystallite nucleation density and average crystallite size varied and appeared to be grain dependent (shown in figure 3.4). These initial studies performed at Clemson University were confirmed by similar analyses on an

independent set of aged rhenium filament samples at SRNL. Measurements made after approximately 1 month of atmospheric exposure indicated that crystallite sizes ranged from <100 nm up to several microns (long axis).

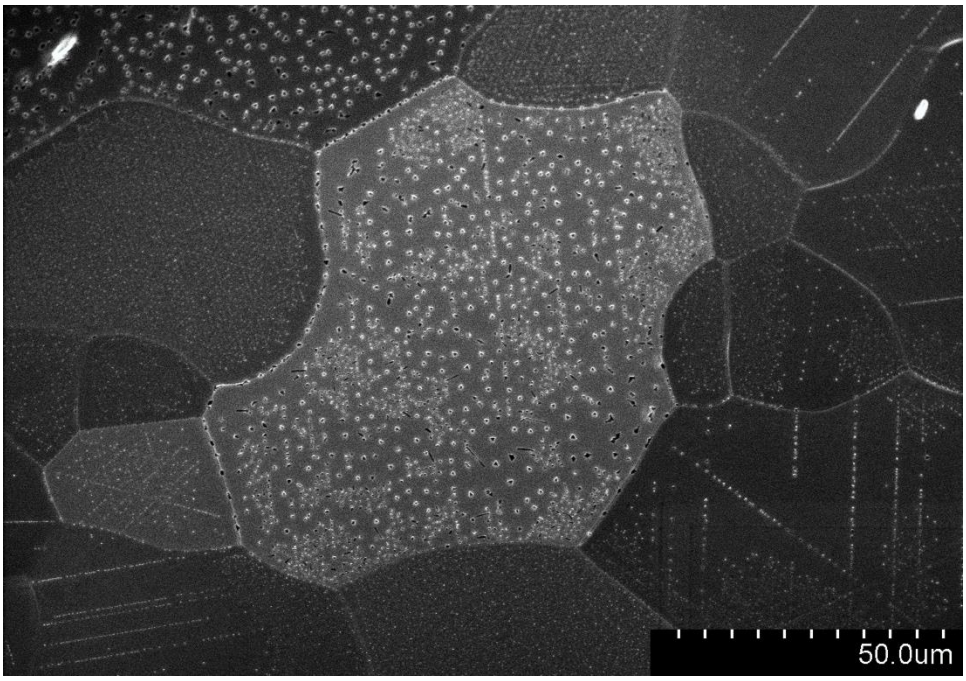

Figure 3.4 SEM image of rhenium filament surface after approximately 1 month of atmospheric exposure. Crystallites were found to be present on most grains; though, inter-granular differences were noted including crystallite size, abundance, and growth patterns.

3.3.3 SEM-EDS analysis of rhenium filaments aged under atmospheric conditions

Elemental mapping of these surfaces by SEM/EDS demonstrated a clear correlation between crystallite location and elevated concentrations of oxygen, seen in figure 3.5. Rhenium, carbon, and nitrogen spectral mappings showed substantially less correlation with the location of crystallites than that of oxygen; though, some correlation can be noted in spectral mapping of nitrogen.

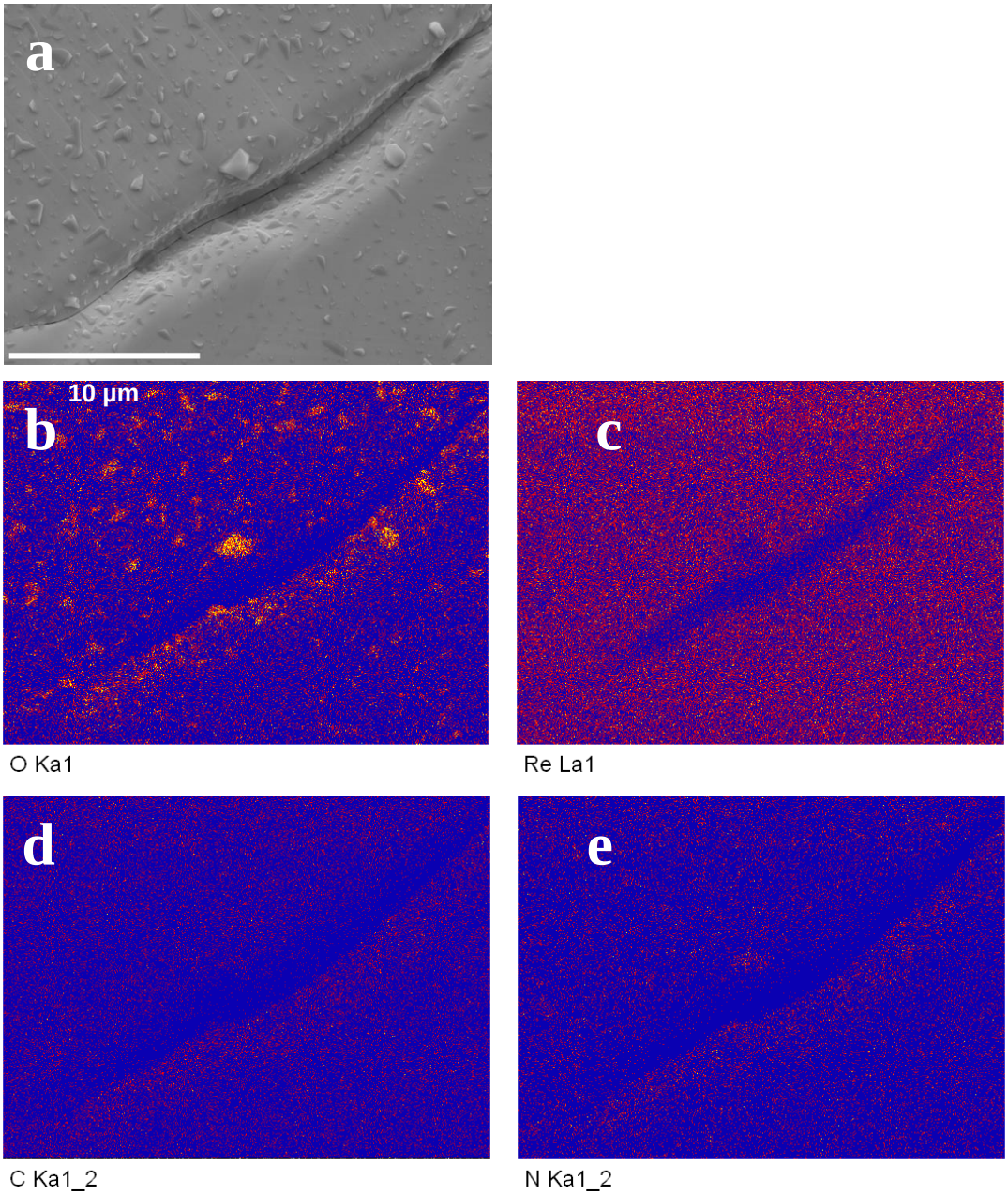

Figure 3.5 SEM/EDS mapping of polycrystalline Re surface demonstrates correlation between crystallite locations and elevated oxygen. Colors in b – e indicate elemental abundance on a blue - yellow scale representing low and high abundance respectively. (a) original SEM image of interrogated region of filament surface. (b) mapping of oxygen showing highest level of correlation with crystallite locations, (c) rhenium, (d) carbon, and (e) nitrogen.

3.3.4 SEM Raman analyses of crystallites on rhenium filaments aged under atmospheric conditions

Identification of the oxo-rhenium species present in the crystallites was attempted through SEM-Raman analysis. Measurements on small crystallites were difficult due to sublimation; however, spectra were collected successfully from crystallites larger than ~1 µm. These spectra were compared with those reported for binary rhenium oxide species and were found to correlate with Re_2O_7 [166] (figure 3.6). The spectra were then compared with those for perrhenic compounds, as perrhenic acid is the hydration product of Re_2O_7, and strong correlation was found with those reported for perrhenic acid [167, 168]; a comparison of Raman shifts for crystallites and those reported in literature for perrhenic acid can be seen in table 3.1. Differences in spectra collected from surface crystallites and bulk samples from the literature can be attributed to surface effects, crystal orientation, and weak signal intensity.

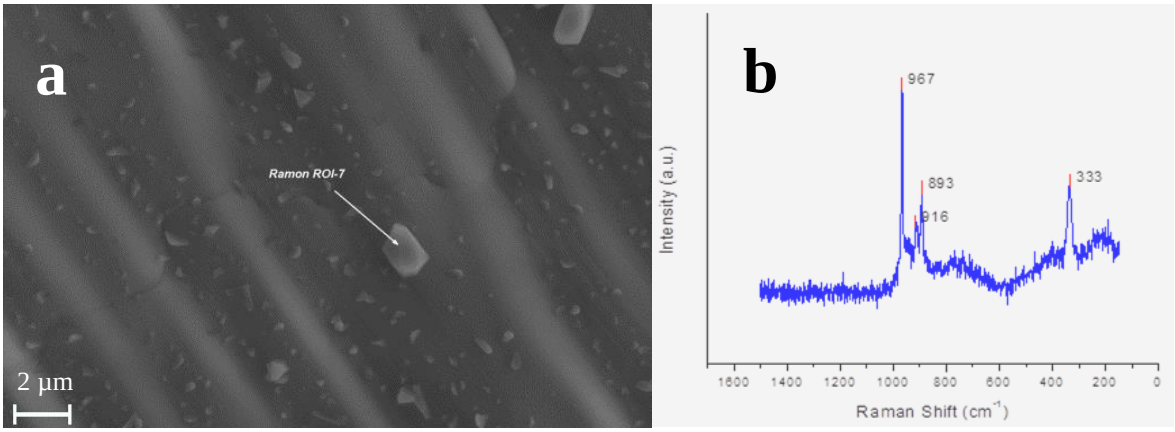

Figure 3.6 SEM-Raman spectra collected from micron sized crystallites that grow on the Re surface: (a) relatively large crystallite (>1 µm) selected for analysis due to issues with sublimation of small crystallites (b) Raman spectrum from an individual crystallite.

Table 3.1 Raman shifts for crystallites and those reported in literature for perrhenic acid.

Crystallites (this study)	Perrhenic acid with assignment [168]	
967 (s)	961 (s)	$\upsilon 1_s$ Re-O
916 (m)	928 (w)	$\upsilon 3_{as}$ Re-O
893 (m)	891 (m)	$\upsilon 3_{as}$ Re-O
	375 (w)	$\upsilon 4$ O-Re-O
		υ O-Re-O
333 (b/s)	337 (w)	$\upsilon 2$ O-Re-O

3.3.5 Analysis of crystalline form

Tetragonal crystalline forms were common among crystallites observed by SEM, seen in figure 3.7. Re_2O_7 is reported to crystallize in the orthorhombic crystalline form [169]; whereas perrhenic acid has been shown to crystalize in the tetragonal system [170, 171], further supporting SEM-Raman identification of the crystallites as perrhenic in nature.

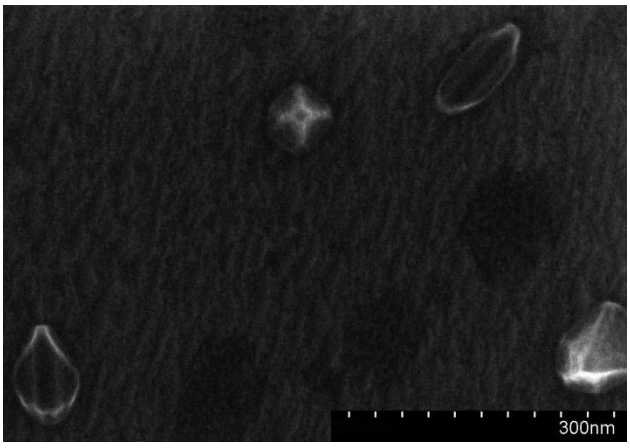

Figure 3.7 Crystallites appear to be predominately tetragonal in form, and 4-fold axis and 2-fold tetragonal dipyramidal axes of symmetry can be seen directed outward from the surface.

3.3.6 EBSD mapping of rhenium filament surfaces to determine grain orientations and phases

It was theorized that the preferential oxidation of certain grains might be due to grain orientation at the surface with some particular orientations possessing a greater propensity for ambient oxidation. EBSD mapping images were collected 2 and 7 weeks after degassing rhenium samples to understand the orientation of grains and monitor the in-growth of rhenium oxide phases. The data indicate that shortly after degassing, the surfaces are composed primarily of Re metal phase with some occurrences of a ReC phase (figure 3.8a). Measurements of crystalline orientation indicate that the surfaces are dominated by the [0001] basal plane with minimal differences among grains with respect to the measured z-component of the Euler angle (figure 3.8b). Isolated grains were imaged that deviated from this basal surface orientation (figure 3.8c); however, these misoriented grains account for a small fraction of the overall surface. These low-occurrence non-basally oriented grains, highlighted in figure 3.9, cannot fully account for the heterogeneity witnessed across these surfaces at more mature levels of crystallite growth (figure 3.4), but may account for the isolated grains that were found to be highly oxidized compared to neighboring grains and the surface as a whole.

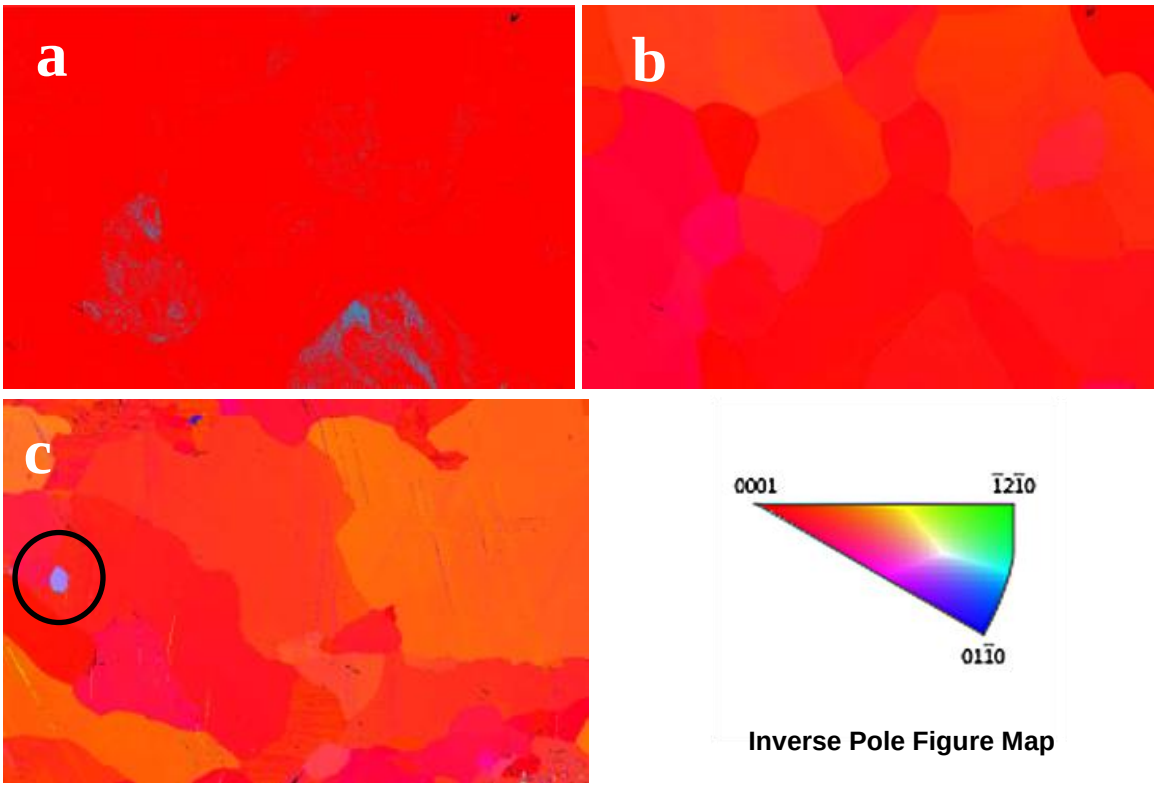

Figure 3.8 EBSD mapping of polycrystalline rhenium surface: (a) Phase mapping with red indicating metallic rhenium and blue indicating rhenium-carbide (of note: these filaments were not intentionally carburized and the source of carbon is unknown at this time.) (b) z-component of Euler angle for basally oriented region. Colors relate to crystalline orientation outlined by inverse pole figure map above with the basal [0001] orientation in red. (c) z-component of Euler angle for region possessing an isolated misaligned grain seen in blue (circled in black to highlight this grain). Colors relate to crystalline orientation outlined by inverse pole figure map.

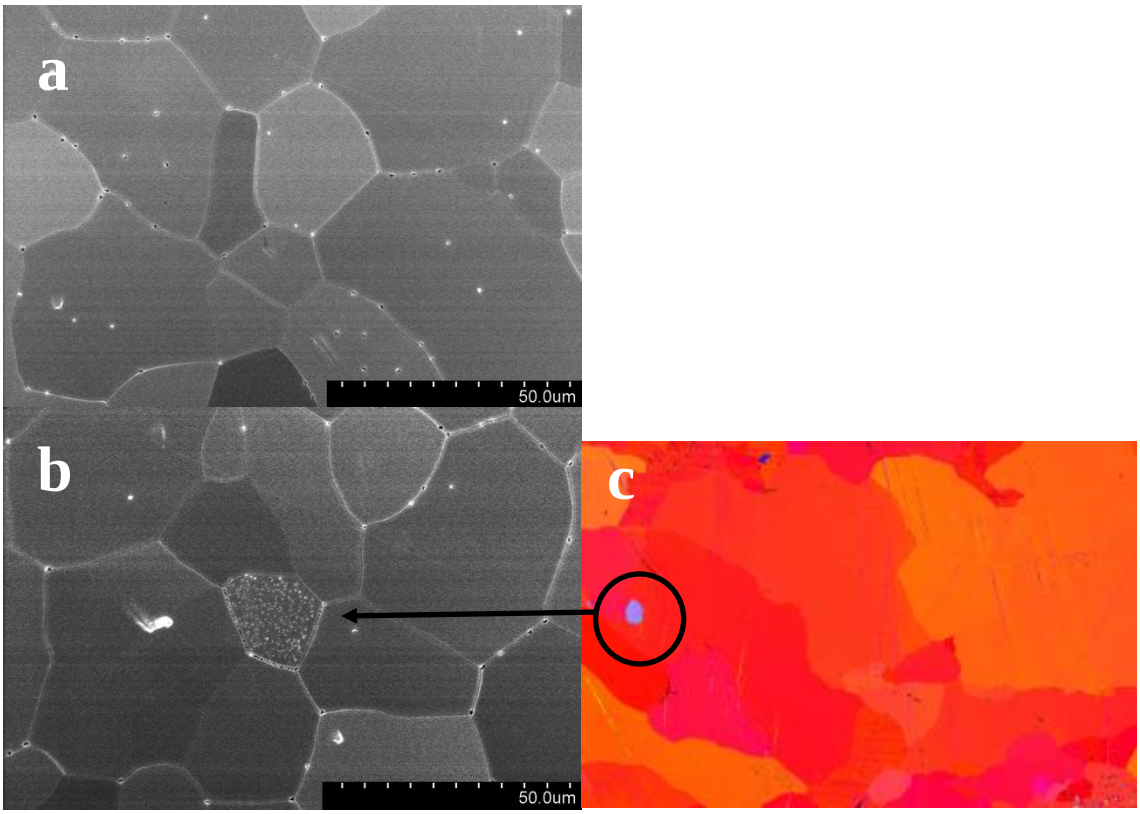

Figure 3.9. (a) Basally oriented region displaying predominately growth along grain boundaries after ~2 weeks of atmospheric exposure. (b) Isolated grain found to be covered in a high density of crystallites after ~2 weeks of atmospheric exposure surrounded by relative barren grains. (c) EBSD mapping of polycrystalline surface where an isolated non-basal grain was discovered. (Of note: (b) and (c) are not the same region of the surface, these figures are intended to demonstrate a possible correlation.)

3.3.7 Identification of region specific mode of crystallite growth

Four region-specific modes of crystallite growth were identified by SEM and AFM examination of these polycrystalline rhenium surfaces: 1) growth along grain boundaries, 2) growth along linear surface dislocations, 3) random growth within relatively flat and seemingly defect-free planes, and 4) growth upon defect sites or faceted regions. The first three modes of

crystallite growth can be seen in figure 3.10a, defect growth can be seen in figure 3.10b, and growth upon a faceted grain can be seen in figure 3.10c. It is unclear at this time whether crystallites migrate or diffuse from their point of nucleation. Crystallite growth along linear surface dislocations was found to be common and results in the formation of crystallite lines, seen in figure 3.10a. Within a grain these crystallite lines often are parallel; however, misalignment with crystallite lines on neighboring grains (figure 3.10b) indicates these linear surface dislocations are not a direct artifact of tooling.

Among intra-granular modes of growth, crystallite formation along linear surface dislocations appears to be the inceptive mode of growth for many of the observed grains. The result can be seen within multiple grains in figure 3.4, where parallel lines of crystallites traverse otherwise barren intra-granular regions. This inceptive growth along dislocations may catalyze or further nucleate crystallite growth within smooth intra-granular regions of the surface, although this hypothesis has not been tested. Growth within flat intra-granular regions was found to be the slowest mode of growth for most grains. The relative rate of growth on faceted grains and defect sites was difficult to determine due to the low occurrence of these features on degassed samples; however, it can be inferred that growth at these sites would likely be more rapid than growth within flat intra-granular regions as was witnessed with growth along grain boundaries and linear surface dislocations. Thus, the overall rate of crystallite growth on a given surface should depend in part upon the relative abundance of these non-planar features. Processes that reduce the roughness of filament surfaces are therefore expected to reduce the rate of oxide growth upon these surfaces. The use of higher degassing temperatures leading to greater filament annealing may be a relatively simple means to acquire smoother surfaces and slow oxidation.

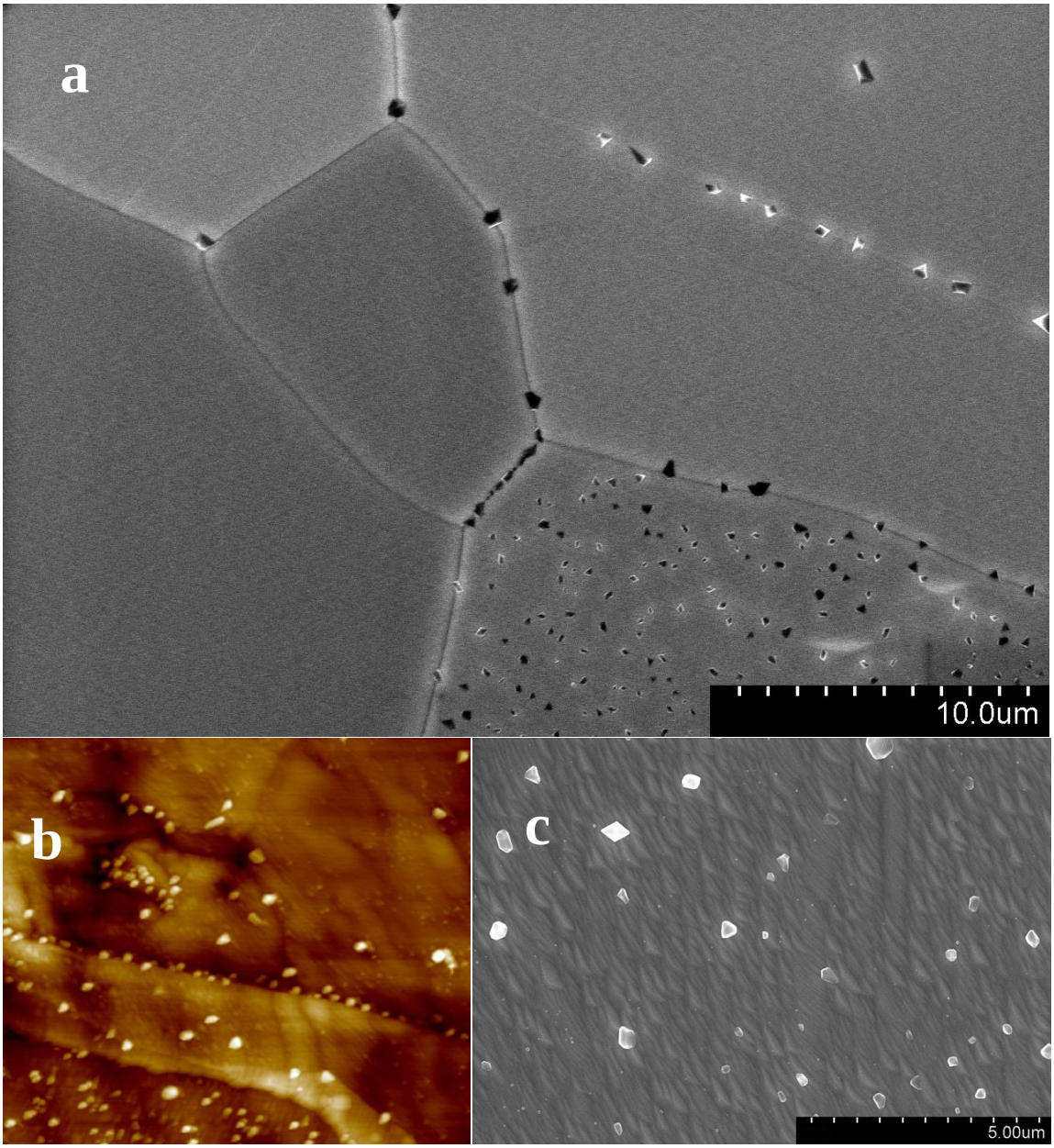

Figure 3.10 (a) SEM image of surface region displaying (1) growth along grain boundaries, (2) growth along a linear surface dislocation. (3) growth within a flat plane. (b) AFM image displaying growth at defect sites (and other modes) [scale is 5 μm × 5 μm, height scale is 100 nm]. (c) SEM image of crystallite growth upon a faceted plane.

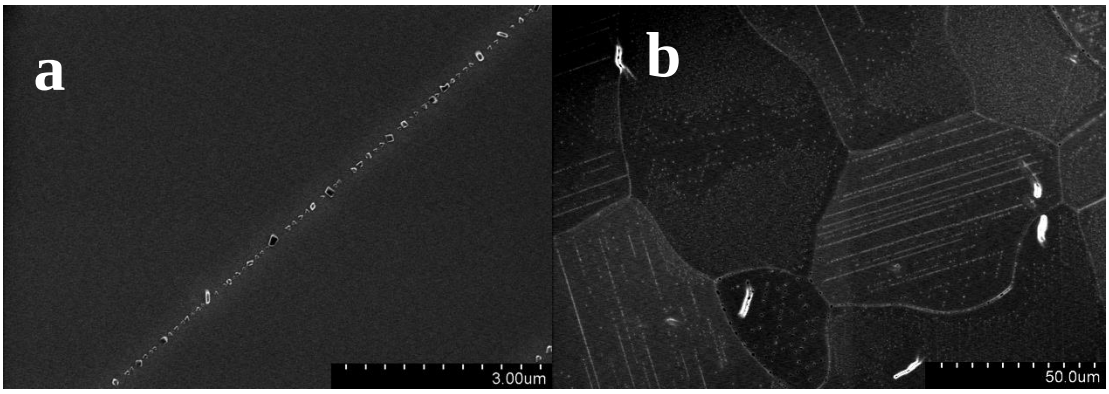

Figure 3.11 SEM images of (a) crystallite growth along a linear surface dislocation and (b) collection of grains exhibiting growth along parallel linear surface dislocation (of note: growth lines are parallel within a grain but not among neighboring grains).

Due to varying growth rates and differences in the potential extent of growth among the regions, the dominant mode of growth (in terms of surface coverage) transitions over time. Crystallite growth along grain boundaries was found to be a dominant mode for degassed samples after intermediate (1-2 weeks) levels of atmospheric exposure (figure 3.9a). After longer exposure times (4-5 weeks) crystallite growth at grain boundaries is a minor contributor to overall crystallite surface coverage (figure 3.4). Determination of a dominant mode of growth at a given point in time is thus dependent upon the average grain size of the polycrystalline surface. Temporal growth of these crystallites is evident, indicating that some transfer of material occurs between the surface and crystallites. The mechanism involved in the transfer of material from the surface is not clear at this point.

We hypothesize that the grain dependent growth seen at mature levels of oxidation (figure 3.4) is largely due to intragranular differences in the abundance and nature of defect regions within these grains. H. Cross Company states that rhenium ribbons are manufactured by powder metallurgy, where rhenium powder is pressed and then sintered. We hypothesize that this

method of manufacture will result in heterogeneous stresses amongst grains due to differences in geometry, size, and localized packing, resulting in intragranular differences in the abundance and type of defects introduced by this method of manufacture.

3.3.8 Examination of filaments aged under atmospheric conditions for years

Figure 3.12 shows SEM images of filaments exposed to atmosphere for years (exact duration unknown) in covered containers. The images suggest that after long periods of ambient atmospheric exposure, the surface crystallites grow in size and eventually begin to fuse creating a confluent coating. This theory is supported by the discovery of fused crystallites on samples exposed to atmospheric conditions for only 1 month, seen in figure 3.12b and 3.12c. In some regions of the highly aged samples (multiple years of atmospheric exposure), the confluent coating appeared to have flaked off revealing a relatively smoother subsurface (images not shown). It is unclear if this loss of portions of the oxide over-layer is due to spallation or another cause.

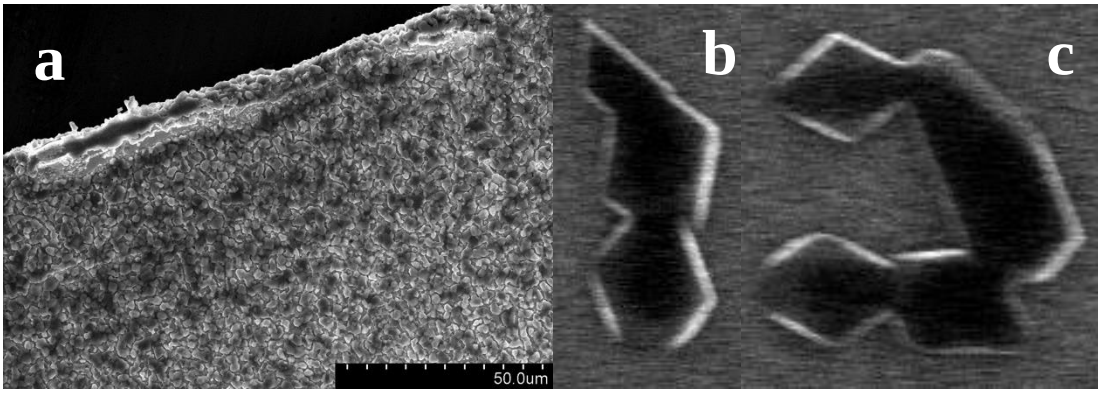

Figure 3.12 (a) Highly aged sample (multiple years of atmospheric exposure) showing that the crystals continue to grow and merge to entirely cover the rhenium surface. (b, c) fused crystallites found on surface after approximately 1 month of atmospheric exposure (crystallites shown in b & c are approximately 300 nm in width).

3.3.9 Effects of carburization on filament morphology and oxidation under atmospheric conditions

The oxidation characteristics of carburized (a.k.a. carbonized) filaments also were investigated. Carburization procedures are incorporated into some TIMS sample preparations and involve resistance heating of the filaments under high vacuum in the presence of a carbon source. In this study, xylene vapor was injected into a custom-built degassing chamber. Carburized filaments were exposed to ambient conditions alongside filaments that had undergone no carburization process during degassing. Figure 3.13 compares 120° three-point grain intersections found on carbonized and non-carbonized filaments after approximately 1 month of atmospheric exposure. Numerous differences can be noted: (1) Carbonized ribbons possess generally more defects near the grain boundaries than non-carbonized ribbons. (2) Average crystallite sizes were smaller on carbonized ribbons than non-carbonized ribbons. (3) Small gray, non-crystalline spots can be seen on carbonized ribbons that appear to be concentrated on particular grains. SEM-Raman suggests that these non-crystalline spots are carbonaceous deposits indicated by broad peaks near 1350 and 1550 cm^{-1} that were detected in these regions (figure 3.14).

The incorporation of carbon through carburization procedures has been shown to increase the effective work function of polycrystalline rhenium [106, 125, 172], and changes in the effective work function of metallic surfaces can be related to changes in the redox potential of surfaces [173]. Qualitative observations by SEM suggest that at a given level of atmospheric exposure the average crystallite size is significantly smaller on rhenium surfaces that were subjected to carburization procedures than those that were degassed in the absence of a carbon source (figure 3.13). Carburization of filaments (or simply carbon incorporation) has been

credited with benefiting TIMS analysis by: 1) facilitating formation of actinide carbides that stabilize actinide analytes on filament surfaces to high temperatures, increasing ionization efficiency; 2) maintaining a reducing environment on the surface of the filament, promoting the production of metallic ions and suppressing analyte-oxide formation; and 3) increasing the work function of the filaments, which increases ionization efficiency. Findings within this study suggest that carburization also increases the "shelf life" of filaments used in TIMS analysis. Section 3.3.12 discusses the reinvestigation of this theory. We hypothesize that the observed passivation afforded by carburization is due to an increase in the work function of these surfaces, which increases the activation barrier for oxidation.

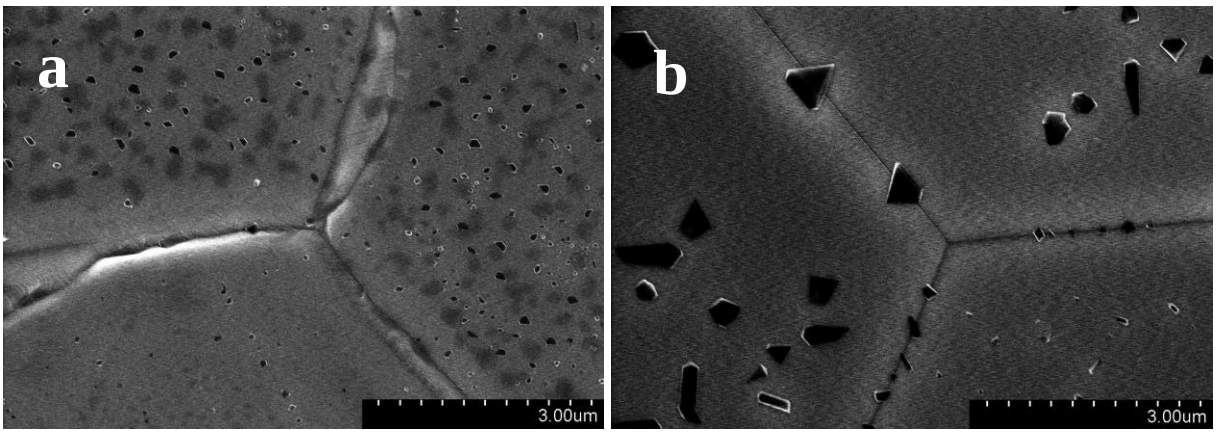

Figure 3.13 Comparison of carbonized rhenium ribbons (a) and non-carbonized rhenium ribbons (b). Carbonized ribbons have a rougher surface with more defects near the grain boundaries than non-carbonized ribbons. Crystallites generally are smaller on carbonized ribbons than non-carbonized ribbons at equivalent durations of atmospheric exposure. Graphitic deposits seen as small dark spots appear on carbonized ribbons and are concentrated on particular crystalline planes.

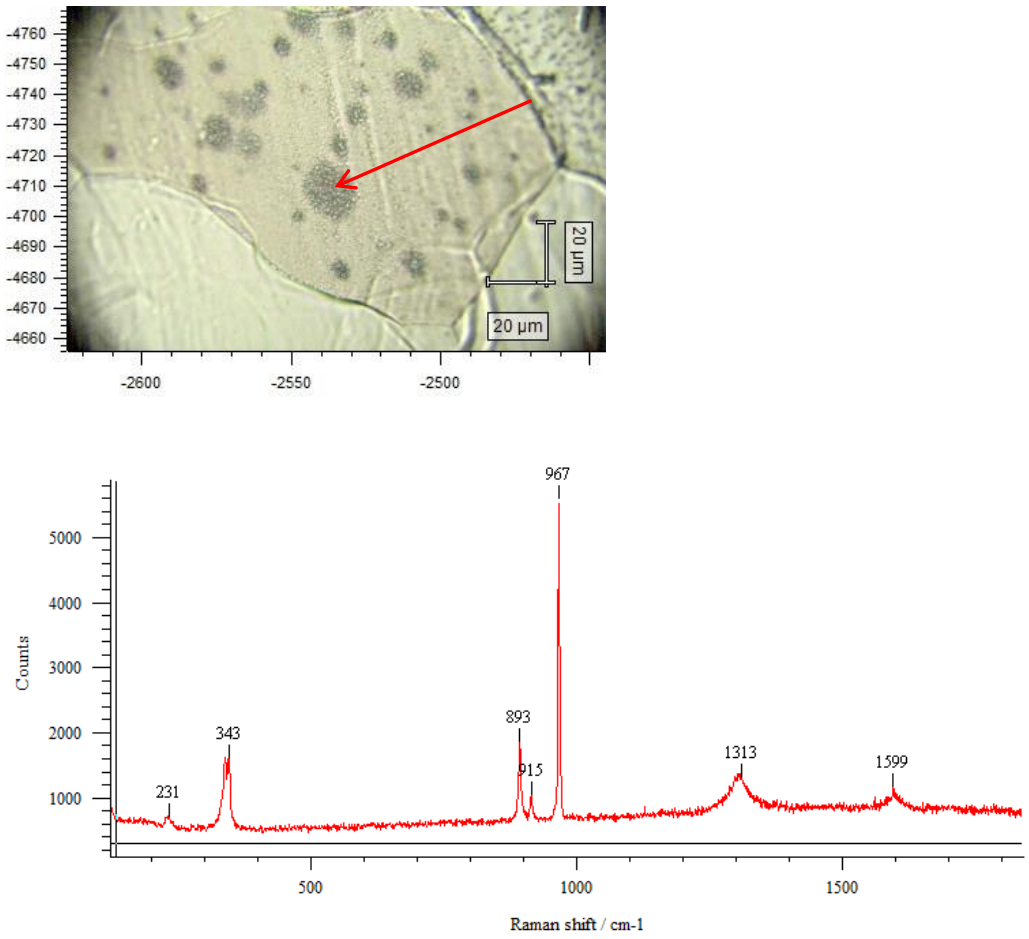

Figure 3.14 SEM-Raman analysis of dark spots witnessed on carbonized ribbons (top image with arrow to indicate the spot which was analyzed) that were found to correspond with broad carbonaceous peaks near 1350 and 1550 cm^{-1} (bottom Raman spectrum).

3.3.10 Hydrophobic polymer films as a means to slow oxidation under atmospheric conditions

The efficacy of hydrophobic thin polymer films as a means of passivating filament surfaces was investigated. Within 1 week of degassing, rhenium filaments were coated with a ~120 nm film of PVBC by dip-coating. These coated filaments were then exposed to atmospheric conditions for 3 months, during which the in-growth of crystallites was absent.

AFM was used for these analyses rather than SEM to prevent degradation of the thin polymer coating. Figure 3.15a shows a coated filament surface after 3 months of atmospheric aging. To ensure that the polymer coating was not obscuring the visualization of any crystallites, filaments aged for 1 month in atmosphere were coated with a thicker (~500 nm) layer of polymer and imaged via AFM. It was known that these filament surfaces possessed a significant coverage of crystallites at the time of coating. Crystallites under the 500 nm film were clearly visible through AFM imaging, appearing as mounds, and can be seen in figure 12b. This control experiment validates the observation that thin polymer films passivate the surface to oxidation.

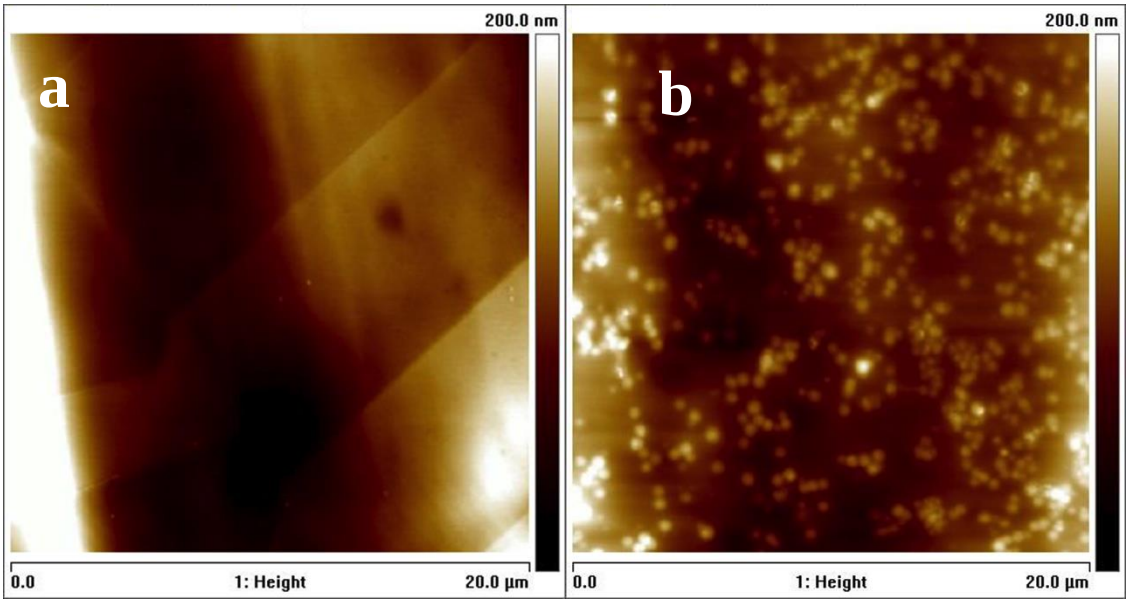

Figure 3.15 AFM images of thin polymer film coated filaments. (a) Re filament coated with 180 nm film after ~1 week oxidation in atmosphere, then exposed to atmosphere for more than 3 months. (b) Re filament oxidized in atmosphere for 1 month and then coated with 500 nm film.

PVBC was selected as the coating material in this study for its chemical similarity to Dowex anion-exchange resins, commonly used in bead loading methods, and its hydrophobicity. It is unclear at this point if passivation of these coated surfaces is due to reduced oxygen diffusion, reduced exposure to water, or a combination thereof. Dip-coating was selected as the film formation method for its simplicity and applicability to complex substrate geometries, such as filament assemblies. In work reported in chapter 2, it was found that thin films of PVBC (on the order of 120 nm) are non-interfering with TIMS analysis of Pu, behaving similarly to bare rhenium filaments.

3.3.11 The effects of humidity on the growth of perrhenic acid crystallites

The ingrowth of oxo-rhenium crystallites on degassed filaments was reported by our group [126]. Crystallites were identified as $Re_2O_7(H_2O)_2$, the hydration product of Re_2O_7, based on SEM-EDS, SEM-Raman, and crystalline form. Three hypotheses arose during this initial study: 1) The formation of $Re_2O_7(H_2O)_2$ crystallites is dependent upon relative humidity of storage conditions. 2) Filament carburization slows the formation of $Re_2O_7(H_2O)_2$. 3) The build-up of surface oxides is, at least in part, the cause of decreased performance (in terms of sample utilization (Pu^+) and/or the precision of isotopic ratio measurements), which has been reported anecdotally in the TIMS community when using excessively aged rhenium filaments for ultra-low-level measurements of Pu. We undertook a second study, detailed in sections 3.3.11, 3.3.12, and 3.3.13, to test these hypotheses.

At 79 days of aging (where degassing was done on day 0), crystallite surface coverage on degassed, non-carburized filaments stored under humid conditions (statically controlled with a saturated NaCl salt bath at ~75% relative humidity [165]; water activity of ~0.7528 [174]) was

34 times greater than crystallite surface coverage on filaments stored under dry conditions (~13% relative humidity). Crystallites were approximately 12 times larger on filaments stored under humid conditions (based on projected area). Approximately 100 to 500 crystallites were captured for analysis in each image. Figure 3.16 compares humid versus dry crystallite growth rates on degassed filaments, in terms of percent surface coverage. Crystallites grew steadily on filaments aged under humid conditions, reaching approximately 2.3% surface coverage at 79 days of aging. No crystallite growth, beyond the initial population of crystallites, was observed on filaments stored under dry conditions. In other metal systems, such as magnesium, the rate of atmospheric corrosion is highly dependent upon the relative humidity of the environment. At 9.5% relative humidity, neither pure magnesium nor any of its alloys exhibit evidence of surface corrosion after 18 months. At 30% relative humidity, only minor corrosion may occur. At 80% humidity, the surface may exhibit considerable corrosion [175]. The lack of crystallite growth under dry conditions supports the hypothesis that the atmospheric corrosion of rhenium is sensitive to relative humidity. Other means of reducing the availability of water in the storage environment, such as storing under vacuum or inert atmosphere, may also suppress the corrosion of rhenium surfaces.

Average equivalent circular diameters (ECD) of crystallites were calculated from projected areas provided by ImageJ particle analysis. Figure 3.17 compares the size distribution of crystallites for a) humid and b) dry conditions at 9 and 79 days of aging. Crystallites grown under humid conditions reached an average ECD of approximately 2 μm after 79 days, while no quantifiable increase in crystallite size was observed on degassed filaments stored under dry conditions. The presence of an initial population of crystallites at the first point of interrogation by SEM (2 days after degassing) and of lack growth under dry conditions may indicate that this

initial population of crystallites formed in the degassing chamber. This hypothesis has not been tested; however, the lognormal crystal size distribution seen in figure 3.17a is consistent with decaying-rate nucleation accompanied by surface-controlled crystal growth (growth with an essentially unlimited supply of nutrients) that occurs in other crystalline systems [176, 177].

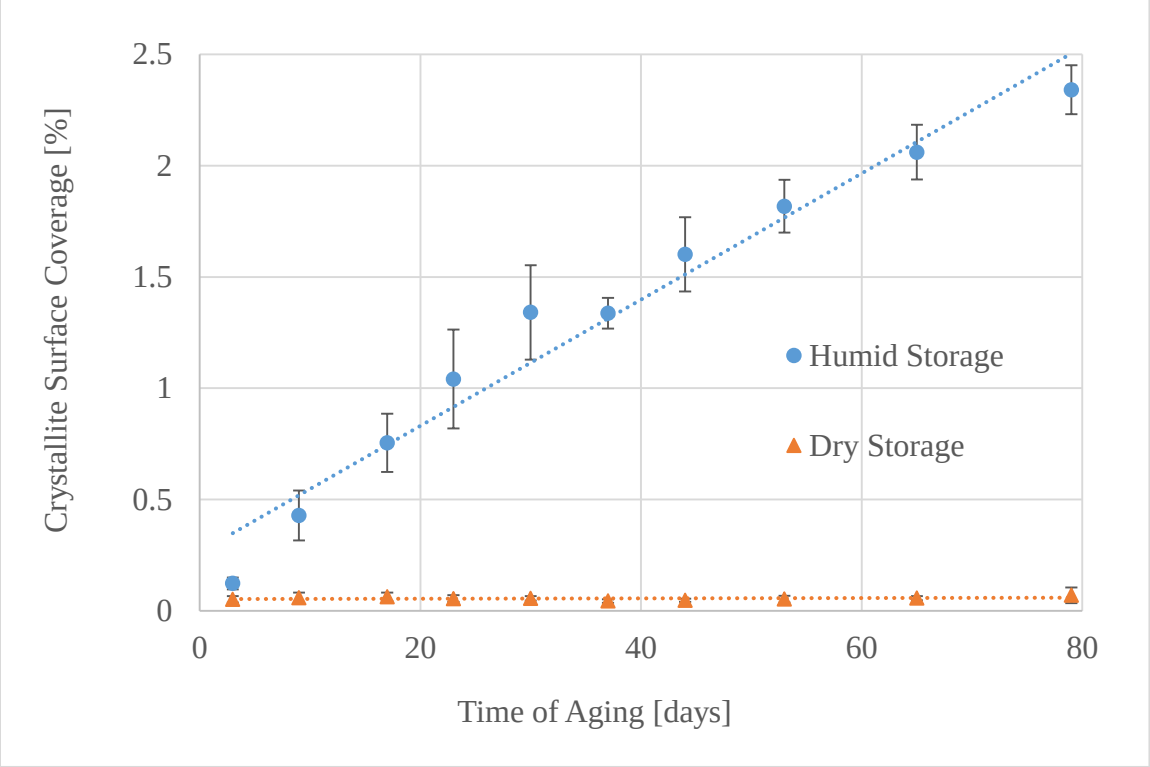

Figure 3.16 Comparison of crystallite surface coverage for degassed filaments stored under humid and dry conditions over the course of aging for 79 days. Error bars represent a 95% confidence interval based on the various images processed at each time step.

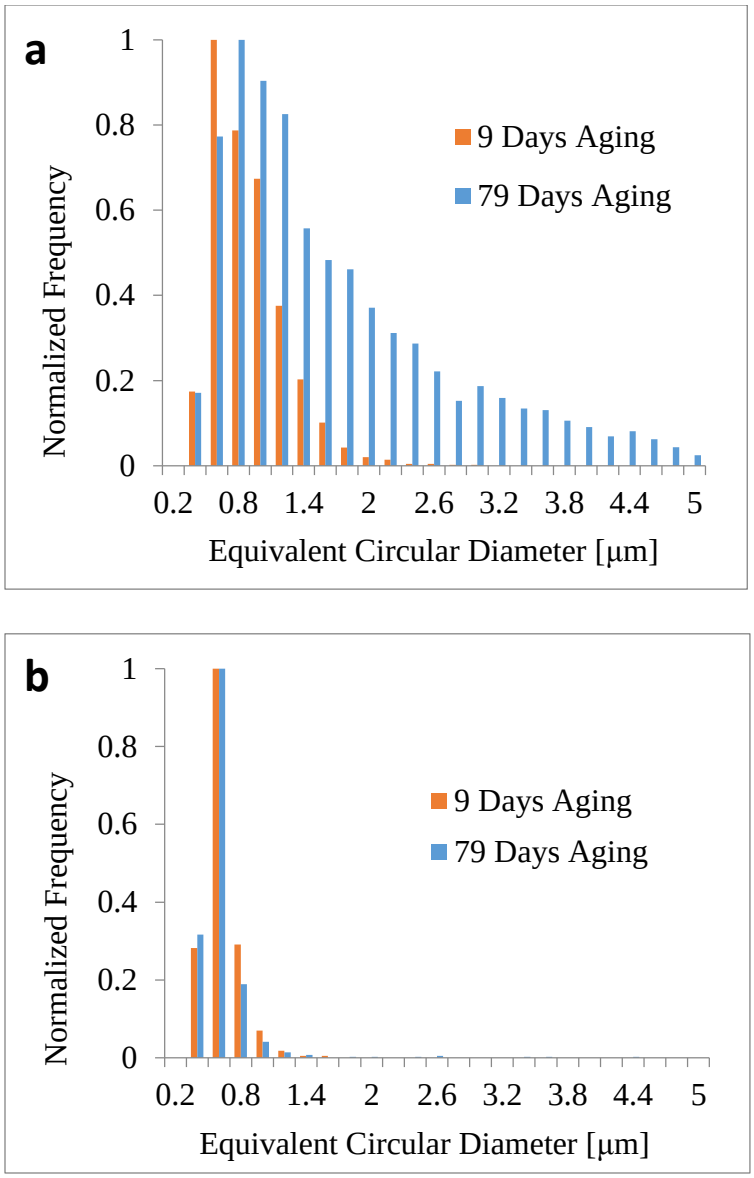

Figure 3.17 A comparison of crystallite size distribution (based on equivalent circular diameter) on degassed filaments aged under a) humid and b) dry conditions at 9 and 79 days of aging.

Figure 3.18 shows a highly oxidized grain that was imaged repeatedly at 44, 65, and 79 days of aging. The growth of crystallites is apparent in figure 3.18; however, the number of crystallites remained constant. This finding is consistent with other areas that were imaged repeatedly over the course of aging. The lack of new crystallite nucleation supports the

hypothesis that crystallite seeding occurs at some point during the degassing process, prior to our SEM investigation. Additionally, crystallite growth appears to be non-uniform and weighted towards certain regions of the surface. As seen in figure 3.18, crystallites located at or near grain boundaries tend to grow more rapidly than those located in intragranular regions.

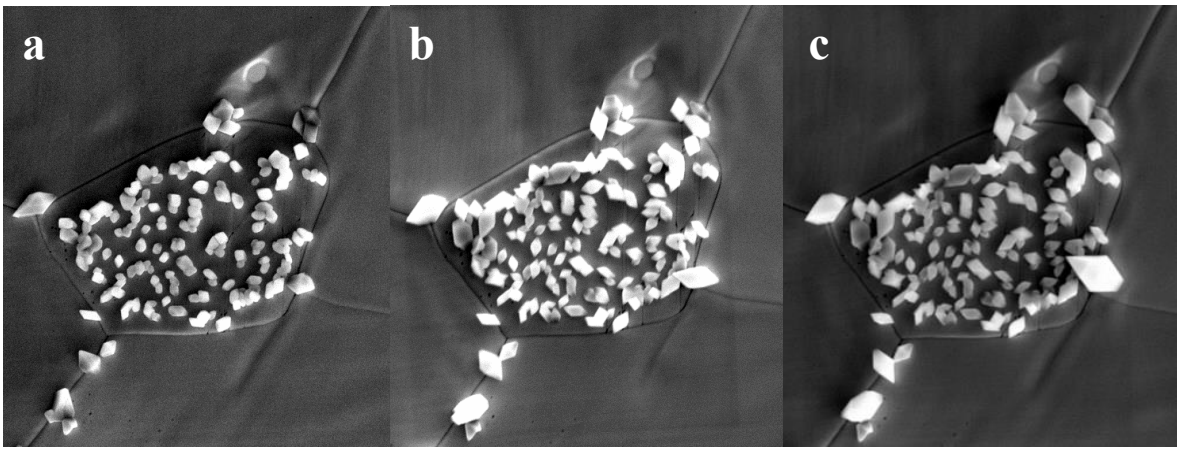

Figure 3.18 A highly oxidized grain imaged at (a) 44 days, (b) 65 days and (c) 79 days of aging under humid conditions (image scale is approximately 28 μm x 32 μm). Filament was degassed only (no carburization). Number of crystallites in the image remains constant over this time span, but their growth is apparent, particularly for crystallites located on or near grain boundaries.

3.3.12 Effect of filament carburization on the growth of perrhenic acid crystallites under humid and dry conditions

Very few crystallites were observed on carburized filaments over the course of 79 days of aging in both humid and dry conditions. At 65 days of aging, some crystallites were found on carburized filaments stored under humid conditions; however, at the moderate magnifications (600x) used for imaging, the crystallites were too small to quantify. No crystallites were observed on carburized filaments stored in dry conditions during the 79 day aging period.

Carburization greatly suppresses the growth of crystallites, either through alteration of the surface redox potential or by interfering with their nucleation. Figure 3.19 shows a comparison of each filament treatment under the four conditions investigated in this study.

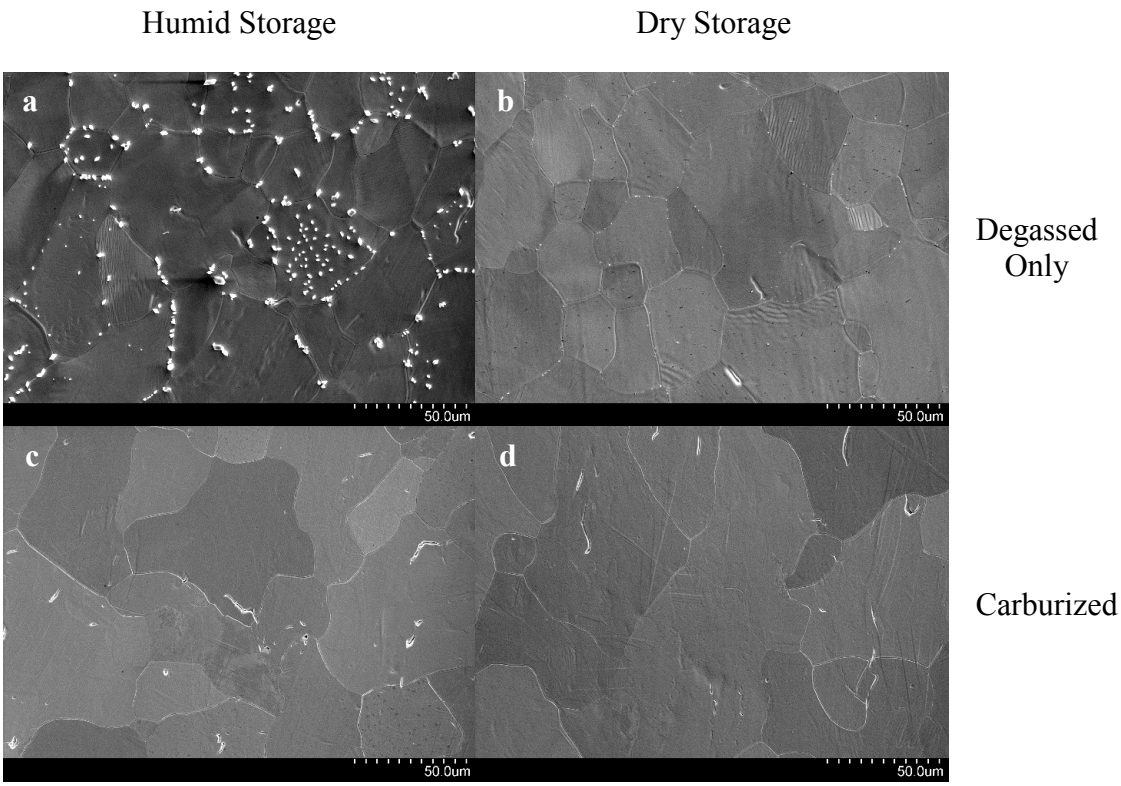

Figure 3.19 SEM images of filaments aged for 65 days under various conditions: a) degassed filament stored under humid conditions (~75% relative humidity), b) degassed filament stored under dry conditions, c) carburized filament stored under humid conditions (~75% relative humidity), d) carburized filaments stored under dry conditions. Bright spots most clearly seen in image a) are crystallite locations.

3.3.13 Effect of filament oxidation on the sensitivity and accuracy of TIMS measurements of Pu

Atomic ion production (as determined by total detected ^{239}Pu + ^{242}Pu ion counts) and isotopic ratio measurements were made using filaments with 1.0% oxide surface coverage and were compared to those made using freshly degassed filaments. Table 3.2 shows a summary of these data. The standard deviation of isotope ratio measurements increased by 170% when using aged filaments and the average isotopic ratio had 60% greater deviation from the certified value for NBL CRM Pu128. Furthermore, average atomic ion production (Pu^+) was approximately 20% lower with a 40% higher standard deviation when oxidized filaments were used. These findings are statistically significant: at a 99% confidence level (using a two-sample F-test, one-tail), the variance in measured isotopic ratio is larger for aged than fresh filaments, and at a 95% confidence level, the measured isotope ratios are unequal (using a two-sample t-test, two tails). In regard to signal loss, at a 90% confidence level the variance in the measured counts is greater for aged filaments than fresh filaments (using a two-sample F-test, one-tail), and at a 78% confidence level the average measured counts is greater for fresh filaments than aged filaments (using a two-sample t-test, one-tail). No runs could be removed as outliers based on low counts using the modified Thompson tau technique ($\alpha = 0.05$).

As was found in our previous study on the atmospheric oxidation of rhenium filaments, the distribution of oxide crystallites is grain dependent [126]. If the interaction of oxides with the sample occurs on a local level, then, due to the small size of resin beads used for loading (150–300 μm diameter), the level of interaction may depend on the proximity to highly oxidized grains. Samples loaded onto relatively barren regions of aged filaments (with regard to oxide crystallites) may be impacted negligibly, while beads located on or near highly oxidized grains

may interact significantly with oxides. Given longer aging periods in an oxidation-promoting environment, as these surfaces become more uniformly covered by oxide crystallites (as was observed in our previous study [126]), we hypothesize the impact of oxidation will become more significant and uniform across sample sets.

Based on the findings, we submit that oxides are, at least in part, the cause of decreased performance that has been observed with aged filaments; moreover, we theorize that suppressed atomic ion production is due to the formation of Pu-oxides.

Table 3.2 Comparison of TIMS analytical performance, using the bead loading method and dimpled filament geometries, for freshly degassed filaments and filaments with 1.0% surface coverage of oxides.

Filament Condition	Fresh Filaments	1.0% Oxide Surface Coverage
Average Detected Pu Counts	360,394	301,196
Standard Deviation in Pu Counts (RSD)	176,908 (49%)	243,212 (81%)
$^{239}Pu/^{242}Pu$ Ratio	1.0018	0.9971
Standard Deviation in Isotope Ratio Measurements	0.0024	0.0065
Number of Measurements	25	14

3.4 Conclusion

The long-term exposure of polycrystalline rhenium surfaces to ambient air was investigated and preferential ingrowth of oxo-rhenium crystallites was observed. Crystalline form, SEM-Raman vibrational spectroscopy, and SEM-EDS support identification of these crystallites as perrhenic acid, the product of Re_2O_7 hydration. Identification of crystallites as $Re_2O_7(H_2O)_2$ is consistent with the observed absence of growth under dry conditions and accelerated growth under humid conditions. More investigation is needed to determine if crystallite nucleation originates during some stage of degassing and to identify the surface conditions that lead to crystallite nucleation. Factors known to influence the rate of crystallite ingrowth include (1) average grain size due to preferential growth at grain boundaries, (2) grain orientation, (3) relative abundance of defect sites, (4) length of exposure, (5) relative humidity of the environment, and (6) carbon incorporation through carburization. Controlling these factors may increase shelf lives of degassed rhenium filaments used in TIMS analyses. In addition, polymer coatings appear to slow oxidation to a greater degree than carburization, though, the magnitude of this difference is yet to be quantified.

Further investigation is needed to fully elucidate the mechanism(s) that result in decreased ionization efficiency when Pu samples are loaded onto aged filaments, but filament aging resulting in even low levels of oxide surface coverage (1%) was found to markedly reduce atomic ion production and the accuracy and precision of isotopic ratio measurements. Strategies such as carburization, storage under dry conditions, or polymer coating that limit oxide growth are recommended for storage of filaments prior to TIMS analyses.

Variance in atmospheric humidity may, in part, account for inter-laboratory discrepancies in the shelf life of TIMS filaments. Due to the influence of humidity it is not possible to simply

equate equivalent durations of aging. Future studies on the impact of filament oxidation therefore must account for the actual quantity of surface oxides present at the time of analysis, not simply the duration of filament aging.

CHAPTER FOUR

ALPHA SPECTROSCOPY SUBSTRATES BASED ON THIN POLYMER FILMS

4.1 Introduction

The ability to rapidly and efficiently produce samples capable of quantifying actinide concentrations and isotope ratios by alpha spectroscopy has applications in water monitoring, emergency response, nuclear materials processing, nuclear forensics, and nuclear safeguards. For example, knowing the isotope ratio of U or Pu bearing samples can help to understand the source and/or intent of the material [178]. In many cases within both nuclear security and environmental applications, the ability to measure ultra-trace level (pg) quantities of actinide elements is necessary to nuclear security applications. Oftentimes, such sensitivity can only be achieved using mass spectrometric techniques. Alpha spectroscopy can be a simpler and cheaper alternative to mass spectrometry if samples can be prepared with sufficient resolution and capture efficiency. However, preparation of high quality alpha spectroscopy samples is a difficult task because the high linear energy transfer of alpha particles limits the distance an alpha particle can travel through virtually any media. Thus, high quality alpha spectroscopy substrates must be 1) flat, 2) stable, and 3) have a means of chemically or physically sequestering the radionuclides on the surface.

There are several currently employed techniques to prepare alpha spectroscopy samples to avoid self-absorption of the alpha particles, which can have deleterious effects on the resolution of the alpha spectrum. Self-absorption occurs when alpha-emitting isotopes must pass through a portion of the solid source material, which causes energy loss of the particle and leads to a broadening of the spectrum. The result is low energy tailing in the spectrum that makes

isotope discrimination more difficult if not impossible. This phenomenon rules out most porous materials, including many crystalline metal oxides, as sorbents since they would produce spectra with excessive tailing. Rapid methods, such as lanthanum fluoride microprecipitation, can produce samples with high alpha energy resolution but require hazardous chemicals (i.e. hydrofluoric acid), which is not ideal for field application. Electrodeposition can produce good samples but requires specialized equipment and adds another time-consuming step to sample preparation. Thus, a primary objective of this work was to develop a new method based on thin polymer films for the rapid, inexpensive, and efficient preparation of alpha spectroscopy samples that retains the high resolution of those prepared by electrodeposition or microprecipitation.

Organic films recently have been studied as a potential platform for the development of robust alpha spectroscopy substrates capable of rapid field deployment [179]. A variety of film formation techniques have been employed, including common techniques such as spin-coating and solvent casting, and less common methods such as fixing crushed anion-exchange resin beads to a surface [180]. A chemical strategy has been the use of polymer-ligand films [181] or polymer inclusion membranes [182] where a ligand is dispersed with a polymer in solution and co-deposited on the substrate surface. In concept and in preparation, polymer-ligand films are simple, but they present a number of engineering challenges for use as substrates for alpha spectroscopy. The ligands in these films are not bound covalently to the polymer matrix and, thus, are susceptible to leaching. To prevent excessive leaching of the ligand, the polymer matrix must have a low degree of swelling under aqueous loading conditions, which leads to slow uptake kinetics due to the high resistance for transport of aqueous ions into the polymer matrix. In these systems, a significant fraction of bound ions is likely to be deposited below the film-

fluid interface, within the polymer matrix, contributing to energy tailing seen in spectra produced from thicker (2-3 μm) polymer-ligand films [183].

In this work, we prepared and tested a novel substrate for the rapid concentration of actinides and simultaneous sample preparation for high-resolution alpha spectroscopy analysis. The substrate comprises an ultra-thin (10-180 nm), lightly cross-linked polymer film with *covalently* bound quaternary ammonium chloride pendant groups for actinide anion exchange. A thickness of 10-180 nm minimizes tailing due to energy deposition in the film while providing adequate mass of anion-exchange material to complex measurable quantities of actinides. The functionalized films are hydrophilic and readily swell in aqueous systems, eliminating the need for plasticizers to aid in ion transport within the film. Dip-coating was selected as the film formation method for these studies over solvent casting or spin coating. It offers a high degree of reproducibility and control over film thicknesses in the range of 10-1000 nm, produces highly uniform and smooth films apart from edge effects, is more easily scalable than comparable methods, and can be applied to a variety of substrate geometries. The dip-coating film formation procedure can be applied to virtually any polymer system and provides a simple, rapid, and inexpensive means for preparing large batches of ready-to-use substrates for alpha spectroscopy.

Quaternary amine resins and polymers have a long history of use in the production and purification of actinides. The characteristics of actinide-lanthanide binding with quaternary amine bearing resins has been well characterized and found to be non-selective with complexation generally occurring at elevated acid concentrations. This is due to the formation of anionic complexes such as $Pu(NO_3)_6^{2-}$ or $Pu(Cl)_6^{2-}$ at high acid concentrations which undergo anion-exchange with the resin. As such, to promote actinide uptake upon quaternary amine bearing polymer films, actinide samples must be dissolved in concentrated acid solutions. The

necessity of sample acidification combined with the non-selectivity of complexation limits the potential field deployability of quaternary amine based substrates; loading upon quaternary-amine based anion-exchange polymer films from complex environmental samples will likely require purification procedures to prevent degradation of spectral quality from matrix interferences. A simpler loading scheme may be achieved through the use of more selective ligands; however, quaternary amine based films present versatile platform from which to explore the influences of various film parameters under ideal loading conditions. The effects of film properties such as thickness, cross-linking content, and active site distribution upon resulting alpha spectral quality are largely unexplored. Quaternary amine polymer films provide an adaptable base wherein these parameters can be readily modified. Additionally, the non-selectivity of these polymers provides a near universal substrate to explore mass loading effects from various actinide species. Elucidation of these characteristics will guide future efforts in the development of polymer thin-film alpha spectroscopy substrates possessing more selective ligand chemistries that can operate under a wider range of loading conditions.

4.2 Experimental

4.2.1 Materials

The following materials were obtained from Sigma-Aldrich and used as-received: chloroform (Reagent Plus® ≥ 99.8% with 0.5-1.0% ethanol as stabilizer, CAS# 67-66-3); 1,4-diazabicyclo[2.2.2]octane (DABCO, Reagent Plus® ≥99%, CAS# 280-57-9); hydrogen peroxide solution containing inhibitor (30 wt% in water, CAS# 7722-84-1); poly(vinylbenzyl chloride) (PVBC), 60/40 mixture of 3- and 4- isomers (CAS# 121961-20-4); sulfuric acid (95-98%, ACS reagent grade, CAS# 7664-93-9). Triethylamine (TEA, 99%, reagent grade, CAS# 121-44-8) was obtained from Fisher Scientific. Syringe filters were 17 mm 0.45 μm glass/PTFE filters from Maine Manufacturing, LLC. Silicon substrates were acquired from Nova Electronic Materials as 4" N/Ph <100> 1-10 Ohm-CM 500-550 μm SSP prime grade Si wafers diced to 1 cm × 3 cm pieces. Deionized (DI) water with a resistance of 18.2 MΩ was prepared in-house from distilled water that was passed through a Milli-Q water purification system (EMD-Millipore).

4.2.2 Substrate preparation for coating

Silicon and glass substrates were prepared according to the procedure given in section 2.2.3.

4.2.3 Dip-coating

After cleaning, substrates were dip-coated from solutions of PVBC in chloroform. To produce a film with a thickness of approximately 10 nm, the substrate was withdrawn from a 0.5 wt% PVBC solution at a withdrawal rate of 100 mm/min using a Qualtecs Product Industry QPI-128 dip coater. Film thickness increases with increasing polymer concentration and withdrawal

rate [123]; film thicknesses up to approximately 120 nm were produced by increasing polymer concentration to 2 wt% PVBC and withdrawal rate of 340 mm/min. Polymer solutions were filtered using 0.45 µm glass/PTFE syringe filters before dip-coating or the addition of DABCO cross-linker. Film thicknesses were determined with multi-angle ellipsometry (described in section 2.2.10). Immediately before dip-coating, DABCO was spiked into the solution to serve as a cross-linker. The molar amount of DABCO added was limited by stoichiometry based on a 1:2 reaction of DABCO to chloride sites along the PVBC chains, as depicted in figure 4.1. It was determined that to prevent dissolution of the polymer film in chloroform during the subsequent functionalization step, a minimum of 5% cross-linking was needed. A ratio of 18.4 mg DABCO:1 g PVBC was used to prepare films with 5% cross-linking. Films with 50% cross-linking also were prepared. After casting, films were heated in an oven at 80°C for at least 24 h to complete cross-linking.

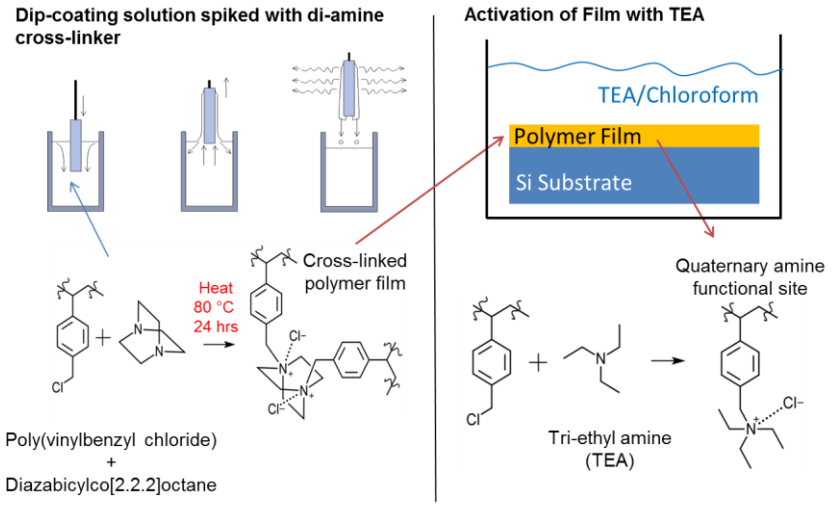

Figure 4.1 Synthetic methods developed to produce chemically stable hydrophilic films with quaternary amine functionality

4.2.4 Functionalization of Polymer Thin-films

Substrates coated by the cross-linked polymer films were submerged in a 5 wt% solution of TEA in chloroform for 24 h at room temperature. After functionalization, the substrates were removed from solution and dried with compressed air. Film thicknesses were measured by ellipsometry before and after TEA functionalization. Film thickness increased from 120 nm to ~180 nm from the TEA functionalization process.

4.2.5 Atomic force microscopy

Atomic force microscopy images were obtained using a Bioscope AFM (Bruker, Inc.) with NanoScope III A controller as described in section 2.2.13.

4.2.6 Stability Analysis of Polymer Films

Loading conditions for actinides on quaternary amine functional groups require high acid concentrations that can produce anionic actinide complexes (such as $PuCl_6^{-2}$ in 9 M HCl). Therefore, to ensure that these conditions do not destabilize the polymer ion-exchange coatings on the substrates, experiments were performed to investigate stability in HCl. Films were prepared without cross-linking and with 5% cross-linking by DABCO. Prior to testing, the films were washed thoroughly and soaked in water for 24 h to remove any residual TEA. The film-coated substrates were suspended in 25 mL of 9 M hydrochloric acid for up to 3 days. Films were removed from solution and allowed to dry in a hood before analysis. Film thicknesses before and after the acid challenge were measured by multi-angle ellipsometry.

4.2.7 Actinide Loading and Alpha Spectroscopy

To demonstrate environmental applicability, uranium uptake studies used a groundwater sample collected from a well at Roundhouse point on Lake Jocasee in South Carolina on August 27, 2013. The water contains naturally occurring uranium at relatively high levels (166.5 ± 2.1 μg/L (ppb) ^{238}U) as determined by direct analysis of the groundwater solution using ICP-MS after acidification to 2 wt% HNO_3. A NIST traceable uranium calibration solution was obtained from High Purity Standards (Charleston, SC) to determine the aqueous U concentration using ICPMS. The uranium bearing groundwater samples were acidified to 3 M, 5 M, and 9 M HCl for uptake studies. Aliquots of each acid stock solution were placed in a petri dish to give the equivalent of 2.5 mL groundwater prior to dilution with the acid (i.e. to maintain a fixed uranium mass in each sample). A glass slide with a 5% cross-linked, TEA functionalized film was submerged in each solution with no agitation. The solution was allowed to air dry completely and the bound uranium was quantified by alpha spectroscopy using an EG&G ORTEC Octête PC Alpha Spectrometer bank with phosphorous doped silicon detectors. A calibration standard for counting efficiency determination was prepared by spotting five 10 μL drops of a 2966 dpm/mL ^{238}Pu solution across a 5% cross-linked, TEA functionalized film that was carefully "smeared" using a pipette tip to cover the area of the film. Films from batch uptake studies were allowed to air dry prior to analysis. Each detector was energy calibrated using a NIST traceable^{238}Pu, ^{241}Am, ^{235}U, and ^{238}U bearing source electroplated on a 25mm diameter steel planchet. Due to the different geometry, this source could not be used as an efficiency standard.

Pu uptakes onto the 10 nm thick functionalized films were measured in the same manner as the uranium uptake experiments. However, to utilize a Pu source with higher specific activity, a 10 μCi/mL ^{238}Pu stock solution was obtained from Eckert and Zeigler Isotope Products

(Valencia, CA). Two ^{238}Pu(IV) working solutions were prepared at ~1000 dpm/mL (1.1×10^{-10} mol/L ^{238}Pu) and ~100 dpm/mL (1.1×10^{-11} mol/L ^{238}Pu) in 9 M HCl using the same method described above for the uranium bearing samples. Separate films were submerged in 5 mL of each solution and allowed to air dry completely, and then the amount of ^{238}Pu on the film was quantified using alpha spectroscopy.

4.2.8 Pu Loading onto 180 nm Films

Certified Reference Material 130 (New Brunswick Laboratory) was used as a Pu source and contains mostly ^{242}Pu by mass but also has measurable concentrations of ^{238}Pu, ^{239}Pu, and ^{240}Pu. The Pu stock solution in 4 M HNO_3 was evaporated to incipient dryness then reconstituted in 9 M HCl to produce a 4.3×10^{-6} M ^{242}Pu stock. To maintain Pu in tetravalent state, $NaNO_2$ was added to reach a concentration of 1 mM. The final oxidation state of Pu in the working solution was verified as Pu(IV) using solvent extraction and coprecipitation. The working solution was spiked into ~100 mL of 9 M HCl to produce a 4.3×10^{-8} M (1 μg/L) dilution. This solution was mixed with a magnetic stir bar and the substrates were submerged and supported with a Teflon jig to avoid contact between the magnetic stir bar and the substrate. Substrates were allowed to contact solution for 2 h. After contact the sample was removed from solution and blotted to remove excess loading solution before allowing the substrate to air dry. This source was selected for these studies because higher mass loading was desired for the thicker films.

4.2.9 Preparation of electrodeposited substrates

Preparation of electrodeposition solutions: for each sample, 1 mL of 1000 dpm/mL Pu^{238} in 9 M HCl solution containing sodium nitrate was diluted with 9 mL of DI water. Methyl yellow

(2-3 drops) was then added to solution and mixed by shaking. Sodium hydroxide solution (2 M) was added dropwise while shaking until a peach color was achieved indicating a pH of 3.2-3.8. This pH was confirmed with litmus paper.

Electrodeposition of Pu^{238}: four stainless steel planchets were prepared by first removing the protective coatings. The planchets were then loaded into four separate fluoropolymer electrodeposition cells that were mounted to a fluoropolymer bracket. Electrodeposition solution was added to each cell (10 mL per cell), and a platinum anode was submerged below the surface of the solution and mounted in place. Care was taken to ensure the platinum anode was not in contact with the stainless steel planchets. The cathode was then attached to the planchet and the power supply was tuned to 2 A (0.5 A/cell). Covers were placed over the cells to reduce evaporation of the electrodeposition solution while under current load. Current was applied for 2 h to complete the electrodeposition. Prior to turning off the power supply, approximately 1 mL of 2 M NaOH was added to the cell to prevent re-dissolution of deposited Pu once the current was removed. The cells were removed from their mounts and the deposition solution was poured out of each cell. The planchets were dried in air before placing within the alpha spectrometer.

4.3 Results and Discussion

4.3.1 AFM imaging of thin films

PVBC-DABCO films produced through dip-coating and activated with TEA were smooth apart from edge effects at all thicknesses upon inspection with AFM (figure 4.2). Excess cross-linker was found to induce porosity within the film; however, films with 0-95% cross-linking with DABCO remain smooth and non-porous.

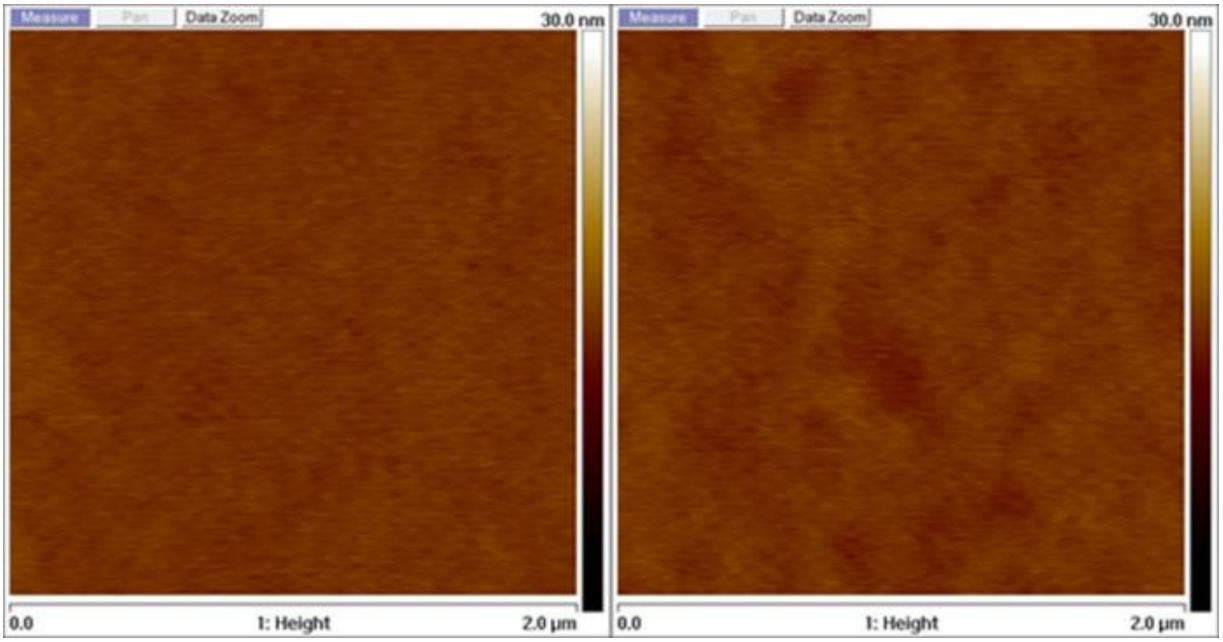

Figure 4.2 AFM images of smooth PVBC films on silicon substrates after cross-linking and TEA activation. Left image is film with 5% cross-linking with DABCO; right image is film with 95% crosslinking with DABCO. Images are 2 μm × 2 μm with a 30 nm height scale. Note: these films are smoother than those shown in figure 2.19; we hypothesize this is due to filtering the polymer solutions which was not done in the preparation of films shown in figure 2.19.

4.3.2 Acid stability testing of thin films

TEA activated films with 5% cross-linking were found to be stable in 9 M HCl. Stability was determined by measuring film thickness before and after acid exposure. Film thicknesses measured by multi-angle ellipsometry for stability testing are provided in table 4.1. Thicker films (~180 nm) were used for these studies so that small changes in thickness would be more evident. Film thicknesses remained the same within measurement uncertainties after soaking in 9 M HCl for 3 days. Delamination of the films was found to occur after multiple weeks of acid exposure; however, it was determined that contact times longer than 3 d were far longer than the time that is required to reach equilibrium in batch uptake studies (described in section 2.3.3).

Table 4.1 Results of film stability testing in 9 M HCl; uncertainties represent 95% confidence intervals based on five measurements.

Film Description	Original film thickness	Thickness after HCl exposure	Treatment
	[nm]	[nm]	
5% CL PVBC/TEA modified	184.3 ± 3.7	180.3 ± 8.0	Aged for 1 month in atmosphere with no acid treatment
5% CL PVBC/TEA modified	178.1 ± 2.9	174.9 ± 2.0	9 M HCl – 1 h
5% CL PVBC/TEA modified	177.2 ± 4.7	176.6 ± 6.7	9 M HCl – 17 h
5% CL PVBC/TEA modified	183.2 ± 5.9	178.4 ± 5.5	9 M HCl – 3 day

4.3.3 Quantification of Pu uptake onto PVBC-DABCO-TEA films

A maximal uptake of approximately 12% was measured when loading from 1000-100 dpm/mL solutions of ^{238}Pu(IV) and was achieved within 30 min of contact. These samples were

loaded by simply submerging the substrate in actinide bearing acid solution for a given allotment of time and these data are shown in table 4.2.

Table 4.2 Pu (IV) sorption onto ~180 nm 5% cross-linked PVBC-DABCO-TEA films.

Sample	Mass Loading of ^{238}Pu (pg)	Percent Uptake (%)
Loading from 5mL of 1000 dpm/mL ^{238}Pu(IV) working solution	31.4 ± 4.65	12.1 ± 1.79
Loading from 5mL of 100 dpm/mL ^{238}Pu(IV) working solution	3.21 ± 0.76	12.2 ± 2.88

4.3.4 Alpha spectroscopy with Pu loaded thin films and comparison to electrodeposited substrates

Despite low uptake on 5% cross-linked PVBC-DABCO-TEA films, the resulting alpha spectra have a resolution of 25-30 keV, which is comparable to electrodeposition (Figure 4.3). The high resolution provided by these substrates resolved the shoulder of the ^{238}Pu alpha peak, which represents different alpha energies from the alpha decay: 5.499 MeV (70.91%) and 5.457 MeV (28.98%).

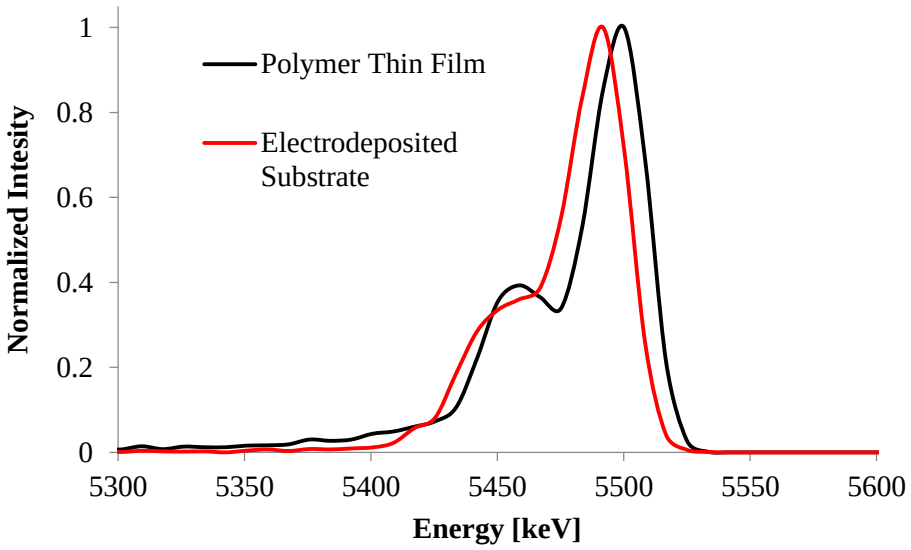

Figure 4.3 Uptake of Pu(IV) out of 9M HCl onto a 180 nm 5% cross-linked, TEA activated PVBC substrate coated on silicon substrates; data determined by alpha spectroscopy (450 mm^2 detector) after: 22 h (thin film substrate) and 24 h (electrodeposited substrate).

4.3.5 Effect of acid concentration on U uptake with PVBC-DABCO-TEA films

Figure 4.3 demonstrates that the HCl concentration strongly affects the uranium uptake onto the film. This result was expected as anion exchange within the polymer film occurs with the $PuCl_6^{-2}$ or $UO_2Cl_4^{-2}$ anionic species, which becomes the dominant aqueous species for Pu and uranium at high acid concentrations. The chloride:actinide ratio increases with increasing HCl concentration owing to formation of $AnCl_x^{4-x}$ and $AnO_2Cl_x^{2-x}$ complexes [8]. Due to the low specific activity of natural uranium, efforts were made to maximize the amount of uranium loaded onto these films by allowing the loading solutions to fully dry while in contact with the substrates. During drying the liquid phase abundance approaches zero, which drives the complexation equilibrium towards the solid phase resulting in near complete uptake under certain conditions (figure 4.4).

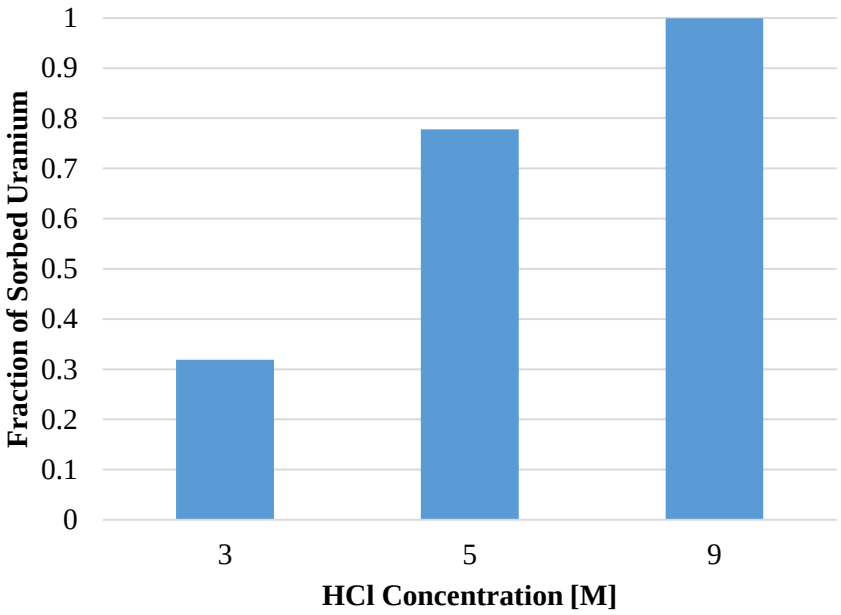

Figure 4.4 Fraction of sorbed uranium on 10 nm 5% cross-linked, TEA activated PVBC film after total evaporation of uranium solution; data determined from alpha spectroscopy after: 240 h (9 M), 300 h (5 M), and 435 h (3 M) of count time.

Although the alpha peaks for uranium were clearly evident (figure 4.5), the spectra showed considerable peak broadening especially at low acid concentration. Energy resolutions for the ^{238}U peaks at 4.2 MeV were 35 keV (9 M), 32 keV (5 M), and 54 keV (3 M). The relatively poor-quality uranium spectra are attributed to several factors. While although the mass loading of uranium is high, the specific activity of its naturally occurring isotopes is low, and so several days of counting is necessary. The high mass loading also results in a large degree of self-attenuation of the alpha particles, causing tailing of the alpha peaks and subsequently decreased resolution. In addition, the uranium daughter products can be observed in the spectrum. These daughters can overlap with uranium peaks. For example, ^{226}Ra has an alpha

peak at 4.870 MeV that overlaps with the ^{234}U peak at 4.859 MeV and hampers isotopic analysis without effectively purifying the solution prior to uptake.

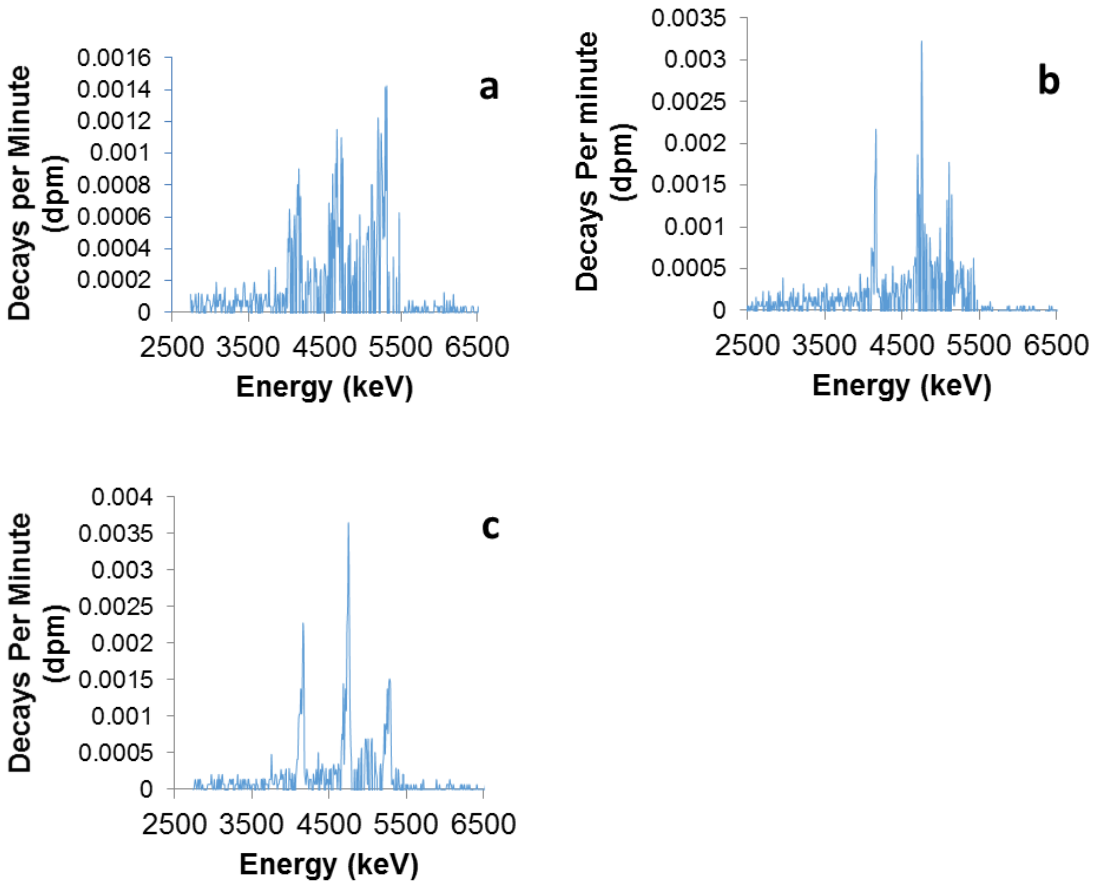

Fig. 4.5 Alpha spectra of uranium from natural well water loaded onto 10 nm 5% cross-linked, TEA activated PVBC substrate in 3 M HCl (a), 5 M HCl (b), and 9 M HCl (c); data determined from alpha spectroscopy after: 240 h (a), 300 h (b), and 435 h (c) of count time.

4.3.6 Effect of mass loading on spectral resolution obtained with PVBC-DABCO-TEA films

To examine the influence of uranium mass loading on the sample, one film was initially loaded by submerging in a "clean" solution containing $^{238}Pu(IV)$ and the alpha spectrum was collected. Then the same film was returned to a petri dish and loaded with natural uranium by

allowing the natural uranium bearing solution to fully evaporate onto the substrate. Figure 4.6 shows the spectra for the films after each uptake period. The ^{238}Pu prior to addition of uranium shows 25-30 keV resolution and relatively little tailing (though it is exaggerated on the logarithmic y-axis of figure 4.6). After loading the same substrate with natural uranium, the Pu peak shows a substantially reduced count rate (by about an order of magnitude) at the max peak energy, as well as extensive tailing. The tailing arises from attenuation of the Pu alpha particles due to the large mass loading of precipitates covering the Pu. Well water used in this study was not purified prior to loading and thus contained an abundance of natural salts that were deposited during drying. Due to the low specific activity of natural uranium isotopes, the uranium does not have sufficient activity to be observed above the substantial tailing of the ^{238}Pu peak.

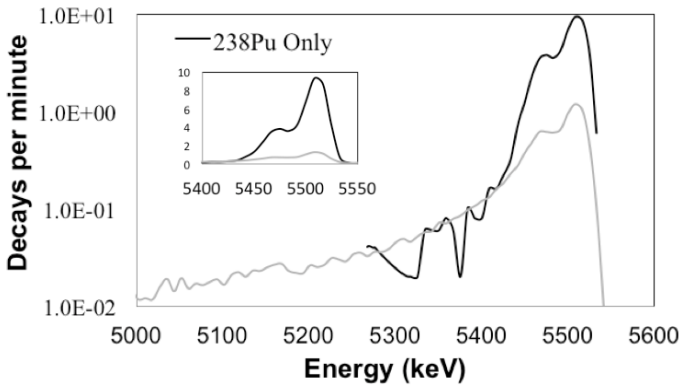

Figure 4.6 Alpha spectroscopy of ^{238}Pu on 10 nm 50% cross-linked, TEA activated PVBC substrate loaded from 9 M HCl (black line) and spectrum after film was re-submerged in 5 mL of well water in 9 M HCl (grey line). The data for ^{238}Pu only below 5300 keV are equivalent to background so the data cannot be plotted on the log y-axis. Original Pu alpha spectrum was collected over a 50 min acquisition time; after uranium exposure a 90 h acquisition time was used to collect the alpha spectrum.

4.4 Conclusions

Thin-film polymer substrates yielded alpha spectra for Pu (IV) with high resolution that is comparable to electrodeposition under ideal loading conditions. High acid concentrations were needed to drive uptake of actinides into the films, requiring special considerations if these are to be used in a field deployable method; however, this is a limitation of the selected polymer chemistry. Substrates loaded with uranium sorbed from natural well waters performed poorly when compared to thin film substrates loaded from "clean" Pu solutions. Removing or preventing deposition of precipitates on the surface of the films and purification of the uranium solution to remove daughter products is needed to improve analyses for samples loaded from natural waters. Complete drying of natural samples upon the substrates exacerbated problems associated with complex sample matrices and should be avoided as a loading method.

The influence of film thickness and active site distribution on substrate performance needs further elucidation. Plasma cleaning of the substrates can be used as an alternative method to piranha washing to minimize hazards associate with the substrate fabrication method. Extending this general method of alpha spectroscopy substrate preparation to other polymer/ligand systems may allow to actinide loading in less acid conditions, making the method better suited for field deployment.

CHAPTER FIVE

CONCLUSIONS AND RECCOMENDATIONS

Three improvements to sample loading procedures for TIMS analysis were achieved in this study including a new filament geometry and two sample loading techniques. The dimpled filament geometry improved measurement sensitivity when bead loading and employing the toroidal spot loading technique. Unfortunately, the dimpled filament geometry was not used with the anion-exchange fiber loading technique due to time and budget constraints. Due to the improvements when employing dimpled filaments with other sample loading strategies, I recommend the investigation of dimpled filaments in conjunction with the fiber loading technique. The trough-like geometry of dimpled filaments may compliment the geometry of fibers and aid in positioning fibers at the geometric center of filaments. Additionally, the influence of dimple dimensions on the resulting measurement sensitivity were not investigated. Preparation of filaments with "deeper" dimples may better mimic the geometry of the cavity source and provide greater opportunity for neutral gas atoms to interact with the ionization surface. The preparation of dimpled filaments is similar in difficulty to that of V-shaped filaments that commonly are employed in some labs, and so the only barrier to adoption of this filament geometry is the lack of commercially available crimping devices to create the dimpled geometry. Improvements in terms of sample losses may be adequate impetus for investment in the construction of custom-made crimping devices.

The fiber loading method was found to markedly improve the sensitivity, accuracy, and precision of Pu isotope ratio measurements by TIMS over that of the bead loading method. The average number of detected Pu+ counts was 180% greater and there was a 72% reduction in

standard deviation of ratio measurements when using fiber loading. An average deviation of 0.0012 (0.117%) from the certified isotope ratio value of NBL CRM Pu128 was measured when fiber loading versus a deviation of 0.0028 (0.284%) when bead loading. Similarly to the dimpled filament geometry, the influence of fiber dimensions was not explored in this study due to budget constraints and instrument availability. Investigation into the thin film loading strategy indicate that the quantity of exchange polymer on the filament effects measurement sensitivity to a large degree. I hypothesize that measurement sensitivity when fiber loading will be affected in the same way by the quantity of polymer loaded onto filaments. This hypothesis could be tested by either altering the diameter or length of fibers used in sample loading. I hypothesize that increasing the length of loaded fiber sections may reduce sensitivity of analysis due to the creations of a more dispersed ion origin. The fiber formation method may serve as a convenient platform to study the influence of complexing polymer chemistry on measurement sensitivity. The fiber formation method is simple and applicable to other polymer chemistries. In addition to the fibers described in chapter 2, fibers were prepared composed of N,N-dimethylhexylamine quaternized poly(2,6-dimethyl phenylene oxide) and iodohexane quaternized poly(4-vinylpyridine). Unfortunately, due to budget and time constraints these fibers were used in sample loading for TIMS.

As was stated previously, it has been hypothesized that Pu-carbides are beneficial intermediate species in thermal ionization of Pu [4, 103], as the carbide form stabilizes Pu on the ionization surface to higher temperatures, increasing ionization efficiency upon carbide decomposition. It has been hypothesized further that actinides must be chemically associated with carbonaceous material to be converted to the carbide form effectively [96]. A study was carried out to better understand thermal ionization mechanisms for U in the presence of carbon

[112]. The formation of uranium-carbides was supported by this study; however, the investigated carbon sources were all graphitic in nature and no difference in the propensity for carbide formation was observed among the different non-complexing graphitic carbon sources. No known study has been reported that investigates the effect(s) of carbon source chemistry (complexing polymer versus non-complexing) on the effectiveness of actinide-carbide formation despite the hypothesized importance of this process in TIMS. Furthermore, knowledge of the impact(s) of complexing polymer properties, such as actinide binding energy or elemental composition, on ionization efficiency is lacking. Actinides form nitrides [184-187], phosphides [188, 189], sulfides [188, 189], carbonitrides [190], oxycarbides [190], and nitridehalides [191] at high temperatures. Thus nitrogen, phosphorous, sulfur, oxygen, or halides in complexing polymers may promote the formation of these phases and impact thermal ionization behavior. We suspect that in the case of bead loading with quaternary amine bearing polymers, the formation of Pu-nitride intermediate may contribute to improved ionization efficiencies, as the thermal degradation of Pu-nitrides occurs near 1700 – 1900 °C [187], consistent with the peak ionization temperatures of 1600 – 1900 °C [8] for Pu in TIMS. Formation of Pu-carbides may be more or less desirable than Pu-nitride, as PuC has a lower vaporization temperature (1550 °C) than Pu-nitride; whereas Pu_2C_3 may have similar or greater thermal stability (vaporization T >1800 °C) [192]. Lower vaporization temperatures of Pu-phosphide (~1400 °C) and Pu-sulfide (~1500 °C) [188] suggests that the formation of these phases would suppress ionization in comparison to cases where Pu-carbides or Pu-nitride are formed; therefore, the use of phosphorous or sulfur bearing exchange resins may be undesirable for TIMS sample loading. Commercial porous carbon fibers could be used as non-complexing control fibers. Polymer fibers with quaternary amine and trialkylphosphite chemistries could be used as complexing

polymers. Additionally, porous carbon fibers with strong anion-exchange groups [20] could be compared to porous carbon fibers with no Pu-extractive ligands. Aqueous Pu samples would be dried onto fibers to ensure equivalent Pu loading in all cases.

Despite the productive collaboration with researchers at SRNL, TIMS instrument time was limited and sample turnaround time was on the order of 2 months. In addition, the instrument was down for maintenance for long periods during the project. In an effort to expedite the development of a thin film loading strategy, a thermal ionization source was constructed at Clemson University, which is shown in figure 5.1. This ion source was originally designed and constructed to aid in screening thin film designs; however, we began to receive positive results from SRNL near the time of its completion and it was not used for this study. The instrument is capable of recreating conditions found in TIMS ion sources and comprises a filament power supply (capable of providing 0 – 5 A of filament current), an alpha spectroscopy planchet holder, and pumps that attain pressures down to 10^{-5} Pa. The alpha spectroscopy planchet is located orthogonal to the ion beam and is floated to a negative electric potential to attract positive ions towards the plate. Ionization efficiencies can be determined by alpha counting the planchets after runs.

The thermal ion source constructed at Clemson has been tested by loading an acidic solution of Pu onto a rhenium ionization filament and alpha counting the planchet after 4 h of heating at 3.5 A of filament current. Pu was successfully transferred to the planchet during this trial. This thermal ionization instrument has various ports where analytical instruments (e.g. Raman and/or IR probes) can be used for *in situ* measurements of filament conditions or sample chemistry. Ionization efficiencies can be compared between complexing and non-complexing fibers using this instrument. Additionally, investigation into the effects of filament or dimple

geometries could be carried out using the instrument. Finally, great strides in our understanding of thermal ionization mechanism(s) could be made through direct interrogation of chemistries present on filaments under different loading conditions.

Figure 5.1 Thermal ion source created at Clemson University.

A successful thin-film loading strategy was developed during this work that increases TIMS sensitivity for Pu and greatly simplifies sample loading; however, the method was not fully optimized during this study. I believe sensitivity may be increased further through the creation of thicker toroidal spots. We avoided creating spots with thicknesses above 50 µm as this had originally resulted in ubiquitous filament failure. However, these original investigations

were carried out on flat rhenium filaments. Our collaborator at SRNL has hypothesized that the use of dimpled filaments stabilizes the filament through some unknown mechanism. I believe toroidal spots with thicknesses greater than 50 μm should be reinvestigated with dimpled filaments to determine if this hypothesis is true, and determine if measurement sensitivity can be increased further through the use of thicker toroidal spots. Additionally, if the thin film design is to be used for bulk production of analysis-ready filaments, a replacement for the hand-spotting technique described in chapter 2 must be developed. A piezo-electric nanodropper was acquired from Biofluidix (PipeJet P9 nanodispenser) for this purpose. These nanodroppers can be installed in automated arrays that could be used to prepare large batches of filaments. Additionally, I hypothesize that the reproducibility of the method could be improved by better controlling the quantity of polymer deposited onto filaments. The nanodropper has been assembled and tested using 3D SEM to ensure that toroidal spots prepared with the nanodropper are similar in dimensions to those prepared by hand. A batch of filaments was prepared using the nanodropper and delivered to SRNL for testing.

An unreported form of rhenium surface oxidation was discovered during this work. TIMS measurements support the theory that this oxidation detrimentally impacts the performance of Pu isotopic analysis by TIMS with the bead loading method. Our theory that grain dependent growth of oxides is due to local grain morphology and defects needs to be interrogated more deeply to support or refute this theory. Defect sites could be examined with methods such as scanning tunneling microscopy or transmission electron microscopy before and after dosed exposure to oxygen and water vapor to better understand the affinity of these reagents to various defect sites. This sort of investigation is outside the scope or expertise of our group, and we hope

that members of the scientific community with such expertise undertake these endeavors to better understand this phenomenon.

A new method of sample preparation for alpha spectroscopy was developed based on thin films originally intended for use in TIMS. High resolution alpha spectra were collected using these films; however, their use as a field deployable substrate is limited by the need to acidify samples to promote actinide complexation with quaternary amine sites within the films. The general methodology and design of creating cross-linked ultra-thin films could be extended to other polymer-ligand systems with better actinide complexation characteristics at near-neutral pH values. Additionally, methods of covalently attaching films to substrate surfaces could be explored to reduce the occurrence of film delamination during prolonged exposure to acidic solutions. Finally, the influence of factors such as film thickness and levels of cross-linking on the resulting resolution of alpha spectra could be explored to optimize these systems. I hypothesize that highly cross-linked films may suppress diffusion into films, resulting in sample deposition near the film surface. This may be advantageous to improve spectral resolution, but would likely result in lower overall levels of sample uptake. This work provides a foundation for future exploration of ultra-thin film based alpha spectroscopy substrates that may one day be field-deployable and a useful tool in nuclear safeguards and environmental monitoring applications.

Appendix

Approval Letter from David Locklair

CLEMSON UNIVERSITY

Joseph Mannion <jmannio@g.clemson.edu>

Master's Thesis

David Locklair <oswald154@yahoo.com> Tue, Jun 27, 2017 at 8:18 AM
Reply-To: David Locklair <oswald154@yahoo.com>
To: Joseph Mannion <jmannio@g.clemson.edu>

Joe,

Whats going on man good to hear from you. I saw on FB you got married, congratulations! How's married life treating you and how's everything going up there? I was thinking you already graduated. How's the project going?

Feel free to use any data/figures you need for your dissertation. If you need me to locate or send you any other file or documents just let me know. I have to dig them out from my old computer but shouldn't be a problem.

Good hearing from ya man!

Best,

David
[Quoted text hidden]

REFERENCES

1. Aggarwal, S.K., *Thermal ionisation mass spectrometry (TIMS) in nuclear science and technology - a review.* Analytical Methods, 2016. **8**(5): p. 942-957.
2. Bürger, S., et al., *Isotope ratio analysis of actinides, fission products, and geolocators by high-efficiency multi-collector thermal ionization mass spectrometry.* International Journal of Mass Spectrometry, 2009. **286**(2–3): p. 70-82.
3. Kurosaki, H., D. Chang, and K.G.W. Inn, *In search of higher sensitivity: Pu isotopic analysis.* Journal of Radioanalytical and Nuclear Chemistry, 2006. **269**(2): p. 279-281.
4. Watrous, M.G. and J.E. Delmore, *Metal dicarbides as intermediate species in thermal ion formation mechanisms.* International Journal of Mass Spectrometry, 2009. **286**(1): p. 7-10.
5. Schaltegger, U., A. Schmitt, and M. Horstwood, *U–Th–Pb zircon geochronology by ID-TIMS, SIMS, and laser ablation ICP-MS: recipes, interpretations, and opportunities.* Chemical Geology, 2015. **402**: p. 89-110.
6. Quitté, G., et al., *High Precision Hf-W Isotopic Measurements in Meteoritic Material Using Negative Thermal Ionisation Mass Spectrometry (NTIMS).* Geostandards and Geoanalytical Research, 2002. **26**(2): p. 149-160.
7. Trinquier, A., J.-L. Birck, and C.J. Allegre, *High-precision analysis of chromium isotopes in terrestrial and meteorite samples by thermal ionization mass spectrometry.* Journal of Analytical Atomic Spectrometry, 2008. **23**(12): p. 1565-1574.
8. Boulyga, S., et al., *Mass spectrometric analysis for nuclear safeguards.* Journal of Analytical Atomic Spectrometry, 2015. **30**(7): p. 1469-1489.
9. Donohue, D.L., *Strengthening IAEA safeguards through environmental sampling and analysis.* Journal of Alloys and Compounds, 1998. **271–273**: p. 11-18.
10. Chan, L.H., *Lithium isotope analysis by thermal ionization mass spectrometry of lithium tetraborate.* Analytical Chemistry, 1987. **59**(22): p. 2662-2665.
11. Sahoo, S.K. and A. Masuda, *Simultaneous measurement of lithium and boron isotopes as lithium tetraborate ion by thermal ionization mass spectrometry.* Analyst, 1995. **120**(2): p. 335-339.
12. Hoefs, J. and M. Sywall, *Lithium isotope composition of quaternary and tertiary biogene carbonates and a global lithium isotope balance.* Geochimica et Cosmochimica Acta, 1997. **61**(13): p. 2679-2690.
13. Moriguti, T. and E. Nakamura, *Precise Lithium Isotopic Analysis by Thermal Ionization Mass Spectrometry Using Lithium Phosphate as an Ion Source Material.* Proceedings of the Japan Academy, Series B, 1993. **69**(6): p. 123-128.
14. Sahoo, S.K. and A. Masuda, *High precision isotopic measurement of lithium by thermal ionization mass spectrometry.* International Journal of Mass Spectrometry and Ion Processes, 1995. **151**(2): p. 189-196.
15. You, C.-F. and L.-H. Chan, *Precise determination of lithium isotopic composition in low concentration natural samples.* Geochimica et Cosmochimica Acta, 1996. **60**(5): p. 909-915.

16. Moriguti, T. and E. Nakamura, *High-yield lithium separation and the precise isotopic analysis for natural rock and aqueous samples.* Chemical Geology, 1998. **145**(1): p. 91-104.
17. Sahoo, S.K. and A. Masuda, *Precise determination of lithium isotopic composition by thermal ionization mass spectrometry in natural samples such as seawater.* Analytica Chimica Acta, 1998. **370**(2–3): p. 215-220.
18. James, R.H. and M.R. Palmer, *The lithium isotope composition of international rock standards.* Chemical Geology, 2000. **166**(3–4): p. 319-326.
19. Spivack, A.J. and J.M. Edmond, *Determination of boron isotope ratios by thermal ionization mass spectrometry of the dicesium metaborate cation.* Analytical Chemistry, 1986. **58**(1): p. 31-35.
20. Wei, H., et al., *Effective elimination of isobaric ions interference and precise thermal ionization mass spectrometer analysis for boron isotope.* International Journal of Mass Spectrometry, 2004. **235**(2): p. 187-195.
21. He, M., et al., *Effective elimination of organic matter interference in boron isotopic analysis by thermal ionization mass spectrometry of coral/foraminifera: micro-sublimation technology combined with ion exchange.* Rapid Communications in Mass Spectrometry, 2011. **25**(6): p. 743-749.
22. Ishikawa, T. and K. Nagaishi, *High-precision isotopic analysis of boron by positive thermal ionization mass spectrometry with sample preheating.* Journal of Analytical Atomic Spectrometry, 2011. **26**(2): p. 359-365.
23. Wu, H.-P., et al., *An experimental study of organic matters that cause isobaric ions interference for boron isotopic measurement by thermal ionization mass spectrometry.* International Journal of Mass Spectrometry, 2012. **328–329**: p. 67-77.
24. He, M.-y., et al., *Accurate and Precise Determination of Boron Isotopic Ratios at Low Concentration by Positive Thermal Ionization Mass Spectrometry Using Static Multicollection of Cs2BO2+ Ions.* Analytical Chemistry, 2013. **85**(13): p. 6248-6253.
25. Wei, H.-Z., et al., *An improved procedure for separation/purification of boron from complex matrices and high-precision measurement of boron isotopes by positive thermal ionization and multicollector inductively coupled plasma mass spectrometry.* Talanta, 2014. **123**: p. 151-160.
26. Rao, R.M., et al., *High precision isotope ratio measurements on boron by thermal ionization mass spectrometry using Rb2BO2+ ion.* Analytical Methods, 2011. **3**(2): p. 322-327.
27. Foster, G.L., et al., *Accurate and precise isotopic measurement of sub-nanogram sized samples of foraminiferal hosted boron by total evaporation NTIMS.* Chemical Geology, 2006. **230**(1–2): p. 161-174.
28. Paulsen, P.J. and W.R. Kelly, *Determination of sulfur as arsenic monosulfide ion by isotope dilution thermal ionization mass spectrometry.* Analytical Chemistry, 1984. **56**(4): p. 708-713.
29. Kelly, W.R., et al., *Determination of Sulfur in Fossil Fuels by Isotope Dilution Thermal Ionization Mass Spectrometry.* Analytical Chemistry, 1994. **66**(15): p. 2505-2513.
30. Mann, J.L. and W.R. Kelly, *Measurement of sulfur isotope composition (δ34S) by multiple-collector thermal ionization mass spectrometry using a 33S-36S double spike.* Rapid Communications in Mass Spectrometry, 2005. **19**(23): p. 3429-3441.

31. Rosenbaum, J.M., R.A. Cliff, and M.L. Coleman, *Chlorine Stable Isotopes: A Comparison of Dual Inlet and Thermal Ionization Mass Spectrometric Measurements.* Analytical Chemistry, 2000. **72**(10): p. 2261-2264.
32. Holmstrand, H., P. Andersson, and Ö. Gustafsson, *Chlorine Isotope Analysis of Submicromole Organochlorine Samples by Sealed Tube Combustion and Thermal Ionization Mass Spectrometry.* Analytical Chemistry, 2004. **76**(8): p. 2336-2342.
33. Wei, H.-Z., et al., *Precise Determination of the Absolute Isotopic Abundance Ratio and the Atomic Weight of Chlorine in Three International Reference Materials by the Positive Thermal Ionization Mass Spectrometer-Cs2Cl+-Graphite Method.* Analytical Chemistry, 2012. **84**(23): p. 10350-10358.
34. Sun, A., et al., *Separation and analysis of chlorine isotopes in higher plants.* Chemical Geology, 2014. **381**: p. 21-25.
35. Doyle, A., et al., *Spectrometric methods for the determination of chlorine in crude oil and petroleum derivatives — A review.* Spectrochimica Acta Part B: Atomic Spectroscopy, 2013. **86**: p. 102-107.
36. Wielandt, D. and M. Bizzarro, *A TIMS-based method for the high precision measurements of the three-isotope potassium composition of small samples.* Journal of Analytical Atomic Spectrometry, 2011. **26**(2): p. 366-377.
37. Schmitt, A.-D., et al., *The Calcium Isotope Composition of Modern Seawater Determined by Thermal Ionisation Mass Spectrometry.* Geostandards Newsletter, 2001. **25**(2-3): p. 267-275.
38. Heuser, A., et al., *Measurement of calcium isotopes (δ44Ca) using a multicollector TIMS technique.* International Journal of Mass Spectrometry, 2002. **220**(3): p. 385-397.
39. Moore, L.J. and L.A. Machlan, *High-accuracy determination of calcium in blood serum by isotope dilution mass spectrometry.* Analytical Chemistry, 1972. **44**(14): p. 2291-2296.
40. Fassett, J.D. and H.M. Kingston, *Determination of nanogram quantities of vanadium in biological material by isotope dilution thermal ionization mass spectrometry with ion counting detection.* Analytical Chemistry, 1985. **57**(13): p. 2474-2478.
41. Fujii, T., et al., *Application of the total evaporation technique to chromium isotope ratio measurement by thermal ionization mass spectrometry.* Talanta, 2006. **69**(1): p. 32-36.
42. Walczyk, T., et al., *Stable isotope labels as a tool to determine the iron absorption by Peruvian school children from a breakfast meal.* Fresenius' Journal of Analytical Chemistry, 1997. **359**(4): p. 445-449.
43. Davidsson, L., et al., *Influence of ascorbic acid on iron absorption from an iron-fortified, chocolate-flavored milk drink in Jamaican children.* The American journal of clinical nutrition, 1998. **67**(5): p. 873-877.
44. Beard, B.L. and C.M. Johnson, *High precision iron isotope measurements of terrestrial and lunar materials.* Geochimica et Cosmochimica Acta, 1999. **63**(11–12): p. 1653-1660.
45. Johnson, C.M. and B.L. Beard, *Correction of instrumentally produced mass fractionation during isotopic analysis of fe by thermal ionization mass spectrometry.* International Journal of Mass Spectrometry, 1999. **193**(1): p. 87-99.
46. Brantley, S.L., L. Liermann, and T.D. Bullen, *Fractionation of Fe isotopes by soil microbes and organic acids.* Geology, 2001. **29**(6): p. 535-538.

47. Gramlich, J., et al., *Absolute isotopic abundance ratios and atomic weight of a reference sample of nickel.* Journal of Research of the National Institute of Standards and Technology, 1989. **94**(6): p. 347-356.
48. Ghidan, O.Y. and R.D. Loss, *Zinc isotope fractionation analyses by thermal ionization mass spectrometry and a double spiking technique.* International Journal of Mass Spectrometry, 2012. **309**: p. 79-87.
49. Gautier, E., et al., *Isotopic analysis of germanium by thermal ionization mass spectrometry.* Journal of Analytical Atomic Spectrometry, 2012. **27**(5): p. 881-883.
50. Catanzaro, E., et al., *Absolute isotopic abundance ratio and atomic weight of terrestrial rubidium.* J. Res. Natl. Bur. Stand. A, 1969. **73**: p. 511-516.
51. Li, C.-F., et al., *Direct High-Precision Measurements of the 87Sr/86Sr Isotope Ratio in Natural Water without Chemical Separation Using Thermal Ionization Mass Spectrometry Equipped with 1012 Ω Resistors.* Analytical Chemistry, 2015. **87**(14): p. 7426-7432.
52. Li, C.-F., et al., *Rapid and precise determination of Sr and Nd isotopic ratios in geological samples from the same filament loading by thermal ionization mass spectrometry employing a single-step separation scheme.* Analytica Chimica Acta, 2012. **727**: p. 54-60.
53. Quemet, A., C. Maillard, and A. Ruas, *Determination of zirconium isotope composition and concentration for nuclear sample analysis using Thermal Ionization Mass Spectrometry.* International Journal of Mass Spectrometry, 2015. **392**: p. 34-40.
54. Anderson, T.J. and R.L. Walker, *Determination of picogram amounts of technetium-99 by resin bead mass spectrometric isotope dilution.* Analytical Chemistry, 1980. **52**(4): p. 709-713.
55. Rokop, D.J., N.C. Schroeder, and K. Wolfsberg, *Mass spectrometry of technetium at the subpicogram level.* Analytical Chemistry, 1990. **62**(13): p. 1271-1274.
56. Fukami, Y. and T. Yokoyama, *Precise tellurium isotope analysis by negative thermal ionization mass spectrometry (N-TIMS).* Journal of Analytical Atomic Spectrometry, 2014. **29**(3): p. 520-528.
57. Delmore, J.E., et al., *Cesium isotope ratios as indicators of nuclear power plant operations.* Journal of Environmental Radioactivity, 2011. **102**(11): p. 1008-1011.
58. Snow, M.S., et al., *Method for ultra-trace cesium isotope ratio measurements from environmental samples using thermal ionization mass spectrometry.* International Journal of Mass Spectrometry, 2015. **381–382**: p. 17-24.
59. Wakaki, S., S.-N. Shibata, and T. Tanaka, *Isotope ratio measurements of trace Nd by the total evaporation normalization (TEN) method in thermal ionization mass spectrometry.* International Journal of Mass Spectrometry, 2007. **264**(2–3): p. 157-163.
60. Upadhyay, D., E.E. Scherer, and K. Mezger, *Fractionation and mixing of Nd isotopes during thermal ionization mass spectrometry: implications for high precision 142Nd/144Nd analyses.* Journal of Analytical Atomic Spectrometry, 2008. **23**(4): p. 561-568.
61. Andreasen, R. and M. Sharma, *Fractionation and mixing in a thermal ionization mass spectrometer source: Implications and limitations for high-precision Nd isotope analyses.* International Journal of Mass Spectrometry, 2009. **285**(1–2): p. 49-57.

62. Li, C.-f., et al., *Directly determining 143Nd/144Nd isotope ratios using thermal ionization mass spectrometry for geological samples without separation of Sm-Nd.* Journal of Analytical Atomic Spectrometry, 2011. **26**(10): p. 2012-2022.
63. Li, C.-F., et al., *Simultaneous Determination of 143Nd/144Nd and 147Sm/144Nd Ratios and Sm–Nd Contents from the Same Filament Loaded with Purified Sm–Nd Aliquot from Geological Samples by Isotope Dilution Thermal Ionization Mass Spectrometry.* Analytical Chemistry, 2012. **84**(14): p. 6040-6047.
64. Hirahara, Y., et al., *Precise Nd isotope analysis of igneous rocks using cation exchange chromatography and thermal ionization mass spectrometry (TIMS).* JAMSTEC Report of Research and Development, 2009. **2009**: p. 65-71.
65. Mialle, S., et al., *The use of total evaporation method using Channeltron electron multipliers by thermal ionization mass spectrometry for europium isotope ratio measurements on picogram sample amounts.* International Journal of Mass Spectrometry, 2012. **309**: p. 141-147.
66. Touboul, M. and R.J. Walker, *High precision tungsten isotope measurement by thermal ionization mass spectrometry.* International Journal of Mass Spectrometry, 2012. **309**: p. 109-117.
67. Reisberg, L. and T. Meisel, *The Re-Os Isotopic System: A Review of Analytical Techniques.* Geostandards Newsletter, 2002. **26**(3): p. 249-267.
68. Gerstenberger, H. and G. Haase, *A highly effective emitter substance for mass spectrometric Pb isotope ratio determinations.* Chemical Geology, 1997. **136**(3–4): p. 309-312.
69. Thirlwall, M.F., *Inter-laboratory and other errors in Pb isotope analyses investigated using a 207Pb–204Pb double spike.* Chemical Geology, 2000. **163**(1–4): p. 299-322.
70. Huyskens, M.H., T. Iizuka, and Y. Amelin, *Evaluation of colloidal silicagels for lead isotopic measurements using thermal ionisation mass spectrometry.* Journal of Analytical Atomic Spectrometry, 2012. **27**(9): p. 1439-1446.
71. Klaver, M., et al., *Pb isotope analysis of ng size samples by TIMS equipped with a 1013 [capital Omega] resistor using a 207Pb-204Pb double spike.* Journal of Analytical Atomic Spectrometry, 2015.
72. Taylor, R.N., et al., *Evaluating the precision of Pb isotope measurement by mass spectrometry.* Journal of Analytical Atomic Spectrometry, 2015. **30**(1): p. 198-213.
73. Paul, M., et al., *High-precision measurements of seawater Pb isotope compositions by double spike thermal ionization mass spectrometry.* Analytica Chimica Acta, 2015. **863**: p. 59-69.
74. Andersson, P.S. and H. Schöberg, *Determination of 232Th and 230Th in seawater using a chemical separation procedure and thermal ionization mass spectrometry.* Limnology and Oceanography: Methods, 2012. **10**(5): p. 296-303.
75. Rubin, K.H., *Analysis of 232Th/230Th in volcanic rocks: a comparison of thermal ionization mass spectrometry and other methodologies.* Chemical Geology, 2001. **175**(3–4): p. 723-750.
76. Shen, C.-C., et al., *Measurement of Attogram Quantities of 231Pa in Dissolved and Particulate Fractions of Seawater by Isotope Dilution Thermal Ionization Mass Spectroscopy.* Analytical Chemistry, 2003. **75**(5): p. 1075-1079.
77. Skipperud, L., et al., *Plutonium isotope ratios in the Yenisey and Ob estuaries.* Applied Radiation and Isotopes, 2004. **60**(2): p. 589-593.

78. Salbu, B., O. Lind, and L. Skipperud, *Radionuclide speciation and its relevance in environmental impact assessments.* Journal of Environmental Radioactivity, 2004. **74**(1): p. 233-242.
79. Gauthier-Lafaye, F., et al., *Radioisotope contaminations from releases of the Tomsk–Seversk nuclear facility (Siberia, Russia).* Journal of Environmental Radioactivity, 2008. **99**(4): p. 680-693.
80. Bürger, S., et al., *Uranium and plutonium analysis of nuclear material samples by multi-collector thermal ionisation mass spectrometry: Quality control, measurement uncertainty, and metrological traceability.* International Journal of Mass Spectrometry, 2012. **311**: p. 40-50.
81. Martin, P. and G. Hancock, *Routine analysis of naturally occurring radionuclides in environmental samples by alpha-particle spectrometry*. 2004: Supervising scientist.
82. Vajda, N. and C.-K. Kim, *Determination of Pu isotopes by alpha spectrometry: a review of analytical methodology.* Journal of radioanalytical and nuclear chemistry, 2010. **283**(1): p. 203-223.
83. Elliot, L.N., et al., *Determination of femtogram quantities of 239Pu and 240Pu in bioassay samples by thermal ionization mass spectrometry.* Journal of Radioanalytical and Nuclear Chemistry, 2006. **267**(3): p. 637-650.
84. Watrous, M.G., J.E. Delmore, and M.L. Stone, *Porous ion emitters—A new type of thermal ion emitter.* International Journal of Mass Spectrometry, 2010. **296**(1–3): p. 21-24.
85. Watrous, M.G. and J.E. Delmore, *Measurement of trace uranium isotopes using a porous ion emitter.* International Journal of Mass Spectrometry, 2011. **303**(1): p. 1-5.
86. Bu, W., et al., *Mass spectrometry for the determination of fission products 135 Cs, 137 Cs and 90 Sr: a review of methodology and applications.* Spectrochimica Acta Part B: Atomic Spectroscopy, 2016. **119**: p. 65-75.
87. Warneke, T., *High-precision isotope ratio measurements of uranium and plutonium in the environment*. 2002, University of Southampton, Faculty of Science.
88. Janda, J., P. Sládek, and D. Sas, *Electrodeposition of selected alpha-emitting radionuclides from oxalate-ammonium sulfate electrolyte and measured by means of solid-state alpha spectrometry.* Journal of radioanalytical and nuclear chemistry, 2010. **286**(3): p. 687-691.
89. Rokop, D.J., et al., *Thermal ionization mass spectrometry of uranium with electrodeposition as a loading technique.* Analytical Chemistry, 1982. **54**(6): p. 957-960.
90. Kuruc, J., et al., *Alpha spectrometry and secondary ion mass spectrometry of electrodeposited uranium films.* Journal of Radioanalytical and Nuclear Chemistry, 2011. **289**(2): p. 611-615.
91. Lee, M.H. and C.W. Lee, *Preparation of alpha-emitting nuclides by electrodeposition.* Nuclear Instruments and Methods in Physics Research Section A: Accelerators, Spectrometers, Detectors and Associated Equipment, 2000. **447**(3): p. 593-600.
92. Lee, M.H. and M. Pimpl, *Development of a new electrodeposition method for Pu-determination in environmental samples.* Applied Radiation and Isotopes, 1999. **50**(5): p. 851-857.
93. Lee, S.C., J.G. Choi, and V.F. Hodge, *Electrodeposition of selected alpha-emitting nuclides from ammonium acetate electrolyte.* Journal of alloys and compounds, 1994. **213**: p. 465-466.

94. Da Cruz, P.A.L., L. Tauhata, and R.N. Alves, *Mixed alpha sources preparation by electrodeposition.* Applied Radiation and Isotopes, 1998. **49**(9–11): p. 1273-1275.
95. Crespo, M.T., *A review of electrodeposition methods for the preparation of alpha-radiation sources.* Applied Radiation and Isotopes, 2012. **70**(1): p. 210-215.
96. Delmore, J.E., *Micro Ion Source Program NA22 Plutonium Detection Portfolio Final Report*. 2010, Idaho National Laboratory (United States). Funding organisation: DOE-NA (United States).
97. Pallmer Jr, P., R. Gordon, and M. Dresser, *The work function of carburized rhenium.* Journal of Applied Physics, 1980. **51**(7): p. 3776-3779.
98. Fassett, J.D. and P.J. Paulsen, *Isotope Dilution Mass Spectrometry for Accurate Elemental Analysis.* Analytical Chemistry, 1989. **61**(10): p. 643A-649A.
99. Lee, C.-G., et al., *Ultra-trace analysis of plutonium by thermal ionization mass spectrometry with a continuous heating technique without chemical separation.* Talanta, 2015. **141**: p. 92-96.
100. Suzuki, D., et al., *Direct isotope ratio analysis of individual uranium–plutonium mixed particles with various U/Pu ratios by thermal ionization mass spectrometry.* Applied Radiation and Isotopes, 2015. **96**: p. 52-56.
101. Shibahara, Y., et al., *Determination of isotopic ratios of plutonium and uranium in soil samples by thermal ionization mass spectrometry.* Journal of Radioanalytical and Nuclear Chemistry, 2016. **307**(3): p. 2281-2287.
102. Studier, M.H., E.N. Sloth, and L.P. Moore, *THE CHEMISTRY OF URANIUM IN SURFACE IONIZATION SOURCES1.* The Journal of Physical Chemistry, 1962. **66**(1): p. 133-134.
103. Kelley, J.M. and D.M. Robertson, *Plutonium ion emission from carburized rhenium mass spectrometer filaments.* Analytical Chemistry, 1985. **57**(1): p. 124-130.
104. Dresser, M.J., *The Saha-Langmuir Equation and its Application.* Journal of Applied Physics, 1968. **39**(1): p. 338-339.
105. Kawano, H., *Effective work functions for ionic and electronic emissions from mono- and polycrystalline surfaces.* Progress in Surface Science, 2008. **83**(1–2): p. 1-165.
106. Jakopič, R., et al., *Isotope ratio measurements of pg-size plutonium samples using TIMS in combination with "multiple ion counting" and filament carburization.* International Journal of Mass Spectrometry, 2009. **279**(2–3): p. 87-92.
107. Smith, D.H. and J.A. Carter, *A simple method to enhance thermal emission of metal ions.* International Journal of Mass Spectrometry and Ion Physics, 1981. **40**(2): p. 211-215.
108. Pallmer, P.G., R.L. Gordon, and M.J. Dresser, *The work function of carburized rhenium.* Journal of Applied Physics, 1980. **51**(7): p. 3776-3779.
109. Jakopic, R., et al., *Determination of 240Pu/239Pu, 241Pu/239Pu and 242Pu/239Pu isotope ratios in environmental reference materials and samples from Chernobyl by thermal ionization mass spectrometry (TIMS) and filament carburization.* Journal of Analytical Atomic Spectrometry, 2010. **25**(6): p. 815-821.
110. Wayne, D.M., et al., *The thermal ionization cavity (TIC) source: elucidation of possible mechanisms for enhanced ionization efficiency.* International Journal of Mass Spectrometry, 2002. **216**(1): p. 41-57.
111. Smith, D.H., W.H. Christie, and R.E. Eby, *The resin bead as a thermal ion source: A sims study.* International Journal of Mass Spectrometry and Ion Physics, 1980. **36**(3): p. 301-316.

112. Kraiem, M., et al., *Experimental investigation of the ionization mechanisms of uranium in thermal ionization mass spectrometry in the presence of carbon.* International Journal of Mass Spectrometry, 2010. **289**(2–3): p. 108-118.
113. Fassett, J.D. and W.R. Kelly, *Interlaboratory isotopic ratio measurement of nanogram quantities of uranium and plutonium on resin beads by thermal ionization mass spectrometry.* Analytical Chemistry, 1984. **56**(3): p. 550-556.
114. Navratil, J. and L. Martella, *Comparison of anion exchange resins for recovering plutonium from nitric acid waste.* Nuclear Technology, 1979. **46**(1): p. 105-109.
115. King, A.R., D. Knight, and A. Fairhead, *Analysis of uranium and plutonium following adsorption on actinide resin.* Journal of Radioanalytical and Nuclear Chemistry, 2015. **304**(1): p. 163-169.
116. Kraiem, M., *Etude des processus d'évaporation et d'ionisation de l'uranium sur des filaments de spectrométrie de masse à thermo-ionisation*. 2007, Université Louis Pasteur (Strasbourg).
117. Bürger, S., et al., *A high efficiency cavity ion source using TIMS for nuclear forensic analysis.* Journal of Alloys and Compounds, 2007. **444–445**: p. 660-662.
118. Dietz, L.A., *Ion Optics for the V-Type Surface Ionization Filament Used in Mass Spectrometry.* Review of Scientific Instruments, 1959. **30**(4): p. 235-241.
119. Paul, S., et al., *Polymer based sorbent materials for thermal ionization mass spectrometric determination of uranium(vi) and plutonium(iv) ions.* Journal of Analytical Atomic Spectrometry, 2016. **31**(4): p. 985-993.
120. Ryan, J. and E. Wheelwright, *The recovery, purification, and concentration of plutonium by anion exchange in nitric acid*. 1959, General Electric Co. Hanford Atomic Products Operation, Richland, Wash.
121. McHugh, J.A., *Surface ionization—the rhenium V-type single filament.* International Journal of Mass Spectrometry and Ion Physics, 1969. **3**(3-4): p. 267-276.
122. Mannion, J.M., et al., *Rhenium filament oxidation: Effect on TIMS performance and the roles of carburization and humidity.* Talanta, 2017. **168**: p. 183-187.
123. Zhou, J., et al., *Formation and characterization of perfluorocyclobutyl polymer thin films.* Journal of Applied Polymer Science, 2013. **129**(6): p. 3226-3236.
124. Locklair, D., *Uptake of Plutonium on a Novel Thin Film for Use in Spectrometry (Master's Thesis).* 2015.
125. P. G. Pallmer, R.L.G., M. J. Dresser, *The work function of carburized rhenium.* Journal of Applied Physics, 1980. **51**(7): p. 3776-3779.
126. Mannion J.M., W.M.S., Shick C.R., Fugate G.A., Powell B.A., Husson S.M., *Ambient aging of rhenium filaments used in thermal ionization mass spectrometry: Growth of oxo-rhenium crystallites and anti-aging strategies.* Heliyon, 2017. **3**(1).
127. Mathew, K.J., et al., *Total evaporation method for uranium isotope-amount ratio measurements.* Journal of Analytical Atomic Spectrometry, 2013. **28**(6): p. 866-876.
128. Duan, Y., et al., *Characterization of an improved thermal ionization cavity source for mass spectrometry.* Journal of the American Society for Mass Spectrometry, 1999. **10**(10): p. 1008-1015.
129. Locklair, W.D., et al., *Uptake of plutonium on a novel thin film for use in spectrometry.* Journal of Radioanalytical and Nuclear Chemistry, 2016. **307**(3): p. 2333-2338.
130. Yunker, P.J., et al., *Suppression of the coffee-ring effect by shape-dependent capillary interactions.* Nature, 2011. **476**(7360): p. 308-311.

131. Baruzzini, M.L., et al., *Enhanced ionization efficiency in TIMS analyses of plutonium and americium using porous ion emitters.* International Journal of Mass Spectrometry, 2017. **412**: p. 8-13.
132. Suzuki, D., et al., *Direct isotope ratio analysis of individual uranium–plutonium mixed particles with various U/Pu ratios by thermal ionization mass spectrometry.* Applied Radiation and Isotopes, 2015. **96**(0): p. 52-56.
133. M. H. Studier, E.N.S., L. P. Moore, *The Chemistry Of Uraxium In Surface Ionizatiox Sources.* Journal of Physical Chemsitry, 1962. **66**(1): p. 133-134.
134. Kraiem, M., et al., *Development of an improved method to perform single particle analysis by TIMS for nuclear safeguards.* Analytica Chimica Acta, 2011. **688**(1): p. 1-7.
135. Duriez, C., *Rhenium Oxidation by Steam at High Temperatures.* Oxidation of Metals, 2004. **61**(1-2): p. 49-67.
136. Davis, J.R., *ASM Specialty Handbook: Heat-Resistant Materials*. 1997: ASM International.
137. Phillips, W.L., *The Rate Of Oxidation Of Rhenium At Elevated Temperatures In Air.* Journal Of The Less-Common Metals, 1962. **5**: p. 97-100.
138. Konitzer, D., S. Duclos, and T. Rockstroh, *Materials for sustainable turbine engine development.* MRS Bulletin, 2012. **37**(04): p. 383-387.
139. Bouchmella, K., et al., *Olefin metathesis with mesoporous rhenium–silicium–aluminum mixed oxides obtained via a one-step non-hydrolytic sol–gel route.* Journal of Catalysis, 2013. **301**: p. 233-241.
140. Bryskin, B.D., *Evaluation of properties and special features for high-temperature applications of rhenium.* AIP Conference Proceedings, 1992. **246**(1): p. 278-291.
141. Levi, R. and G.A. Espersen, *Preparation of Rhenium Emitters and Measurements of Their Thermionic Properties.* Physical Review, 1950. **78**(3): p. 231-234.
142. Blackham, A.U., R.R. Beishline, and L.S. Merrill, *Rhenium as a Catalyst in Hydrocarbon Reforming Reactions.* I&EC Product Research and Development, 1965. **4**(4): p. 269-273.
143. Greenlee, W.S. and M.F. Farona, *Olefin metathesis by rhenium carbonyl halide-alkylaluminum halide catalysts. Direct evidence for a coordinated carbene initiated process.* Inorganic Chemistry, 1976. **15**(9): p. 2129-2134.
144. Burch, R., *The Oxidation State of Rhenium and Its Role in Platinum-Rhenium Reforming Catalysts.* Platinum Metals Review, 1978. **22**(2): p. 57-60.
145. Spencer, N.D. and G.A. Somorjai, *Rhenium: an ammonia synthesis catalyst.* The Journal of Physical Chemistry, 1982. **86**(18): p. 3493-3494.
146. Sinfelt, J.H., *Structure of bimetallic clusters.* Accounts of Chemical Research, 1987. **20**(4): p. 134-139.
147. Mol, J.C., *Olefin metathesis over supported rhenium oxide catalysts.* Catalysis Today, 1999. **51**(2): p. 289-299.
148. Kunkes, E.L., et al., *The role of rhenium in the conversion of glycerol to synthesis gas over carbon supported platinum–rhenium catalysts.* Journal of Catalysis, 2008. **260**(1): p. 164-177.
149. Beamson, G., et al., *Selective hydrogenation of amides using bimetallic Ru/Re and Rh/Re catalysts.* Journal of Catalysis, 2011. **278**(2): p. 228-238.
150. Koso, S., Y. Nakagawa, and K. Tomishige, *Mechanism of the hydrogenolysis of ethers over silica-supported rhodium catalyst modified with rhenium oxide.* Journal of Catalysis, 2011. **280**(2): p. 221-229.

151. Kraiem, M., et al., *Filament chemistry of uranium in thermal ionisation mass spectrometry.* Journal of Analytical Atomic Spectrometry, 2010. **25**(7): p. 1138-1144.
152. Jakopič, R., et al., *Certified reference materials and reference methods for nuclear safeguards and security.* Journal of Environmental Radioactivity, 2013. **125**: p. 17-22.
153. Sturm, M., et al., *Optimized Chemical Separation and Measurement by TE TIMS Using Carburized Filaments for Uranium Isotope Ratio Measurements Applied to Plutonium Chronometry.* Analytical Chemistry, 2016. **88**(12): p. 6223-6230.
154. Lee, C.-G., et al., *Simultaneous determination of plutonium and uranium isotope ratios in individual plutonium–uranium mixed particles by thermal ionization mass spectrometry.* International Journal of Mass Spectrometry, 2012. **314**: p. 57-62.
155. Park, J.-H., I.-H. Choi, and K.-S. Song, *A technique to minimize impurity signal from blank rhenium filaments for highly accurate TIMS measurements of uranium in ultra-trace levels.* Mass Spectrometry Letters, 2010. **1**(1): p. 17-20.
156. Jeon, Y.-S., et al., *Background effect on the measurement of trace amount of uranium by thermal ionization mass spectrometry.* Analytical Science and Technology, 2008. **21**(6): p. 487-494.
157. Es-Said, O.S., et al., *The Effect of 45° Rolling Process on the Mechanical Properties of P/M Rhenium.* Materials and Manufacturing Processes, 1998. **13**(5): p. 693-717.
158. Murphy, N.R., et al., *Optical and chemical properties of mixed-valent rhenium oxide films synthesized by reactive DC magnetron sputtering.* Optical Materials, 2015. **45**: p. 191-196.
159. Chan, A., et al., *Surface atom core-level shifts of clean and oxygen-covered Re (12 3^{-} 1).* Physical Review B, 2005. **72**(3): p. 035442.
160. Miniussi, E., et al., *Non-local Effects on Oxygen-Induced Surface Core Level Shifts of Re(0001).* The Journal of Physical Chemistry C, 2012. **116**(44): p. 23297-23307.
161. Wang, H., W. Chen, and T.E. Madey, *Morphological evolution in oxygen-induced faceting of Re (12 3^{-} 1).* Physical Review B, 2006. **74**(20): p. 205426.
162. Wang, H., et al., *Facet Stability in Oxygen-Induced Nanofaceting of Re(12$3^{-}$1).* ACS Nano, 2007. **1**(5): p. 449-455.
163. Bai, M., et al., *Preparation of ultrafine rhenium powders by CVD hydrogen reduction of volatile rhenium oxides.* Transactions of Nonferrous Metals Society of China, 2013. **23**(2): p. 538-542.
164. Shcheglov, P.A. and D.V. Drobot, *Heterogeneous equilibria in the rhenium-oxygen system.* Russian Journal of Physical Chemistry, 2006. **80**(11): p. 1819-1825.
165. Rockland, L.B., *Saturated Salt Solutions for Static Control of Relative Humidity between 5° and 40° C.* Analytical Chemistry, 1960. **32**(10): p. 1375-1376.
166. Lacheen, H.S., P.J. Cordeiro, and E. Iglesia, *Isolation of Rhenium and ReOx Species within ZSM5 Channels and their Catalytic Function in the Activation of Alkanes and Alkanols.* Chemistry – A European Journal, 2007. **13**(11): p. 3048-3057.
167. Claassen, H.H. and A.J. Zielen, *Structure of the Perrhenate Ion.* The Journal of Chemical Physics, 1954. **22**(4): p. 707-709.
168. Cazzanelli, E., et al., *Characterization of rhenium oxide films and their application to liquid crystal cells.* Journal of Applied Physics, 2009. **105**(11): p. 114904.
169. Krebs, B., A. Mueller, and H.H. Beyer, *Crystal structure of rhenium(VII) oxide.* Inorganic Chemistry, 1969. **8**(3): p. 436-443.

170. Wltschek, G., I. Svoboda, and H. Fuess, *The crystal structure of Solid Perrhenic Acid Monohydrate.* Zeitschrift für anorganische und allgemeine Chemie, 1993. **619**(10): p. 1679-1681.
171. Lock, C.J.L. and G. Turner, *A reinvestigation of the crystal structure of potassium perrhenate.* Acta Crystallographica Section B, 1975. **31**(6): p. 1764-1765.
172. Pallmer, P.G., R.L. Gordon, and M.J. Dresser, *The emissivity of carburized rhenium.* Journal of Applied Physics, 1980. **51**(3): p. 1798-1801.
173. Gerischer, H. and W. Ekardt, *Fermi levels in electrolytes and the absolute scale of redox potentials.* Applied Physics Letters, 1983. **43**(4): p. 393-395.
174. Stokes, R.H. and R.A. Robinson, *Standard Solutions for Humidity Control at 25° C.* Industrial & Engineering Chemistry, 1949. **41**(9): p. 2013-2013.
175. Zeng, R.-c., et al., *Review of studies on corrosion of magnesium alloys.* Transactions of Nonferrous Metals Society of China, 2006. **16**: p. s763-s771.
176. Eberl, D., V. Drits, and J. Srodon, *Deducing growth mechanisms for minerals from the shapes of crystal size distributions.* American journal of Science, 1998. **298**: p. 499-533.
177. Kile, D.E., et al., *An assessment of calcite crystal growth mechanisms based on crystal size distributions.* Geochimica et Cosmochimica Acta, 2000. **64**(17): p. 2937-2950.
178. Moody, K.J., P.M. Grant, and I.D. Hutcheon, *Nuclear forensic analysis*. 2014: CRC Press.
179. Hanson, S.K., A.H. Mueller, and W.J. Oldham, *Kläui Ligand Thin Films for Rapid Plutonium Analysis by Alpha Spectrometry.* Analytical Chemistry, 2014. **86**(2): p. 1153-1159.
180. Gonzáles, E. and D. Peterson, *Rapid radiochemical sample preparation for alpha spectrometry using polymer ligand films.* Journal of Radioanalytical and Nuclear Chemistry, 2009. **282**(2): p. 543-547.
181. Rim, J.H., et al., *Developing and evaluating di(2-ethylhexyl) orthophosphoric acid (HDEHP) based polymer ligand film (PLF) for plutonium extraction.* Journal of Radioanalytical and Nuclear Chemistry, 2013. **296**(2): p. 1099-1103.
182. Mahanty, B.N., et al., *Polymer Inclusion Membranes Containing N,N,N′,N′-Tetra(2-ethylhexyl) Diglycolamide: Uptake Isotherm and Actinide Ion Transport Studies.* Industrial & Engineering Chemistry Research, 2015. **54**(12): p. 3237-3246.
183. Chavan, V., et al., *Thin extractive membrane for monitoring actinides in aqueous streams.* Journal of Hazardous Materials, 2013. **260**(0): p. 53-60.
184. Green, D.W. and G.T. Reedy, *Infrared spectra of matrix-isolated plutonium nitrides.* The Journal of Chemical Physics, 1978. **69**(2): p. 552-555.
185. Ogawa, T., *Thermodynamic properties of (U, Pu)N1 − x with a sublattice formalism — Equilibria involving the nonstoichiometric nitrides.* Journal of Nuclear Materials, 1993. **201**: p. 284-292.
186. Ogawa, T., et al., *Thermodynamics of carbothermic synthesis of actinide mononitrides.* Journal of Nuclear Materials, 1997. **247**: p. 151-157.
187. Baranov, V.G., et al., *High temperature behavior of simulated mixed nitrides.* IOP Conference Series: Materials Science and Engineering, 2016. **130**(1): p. 012022.
188. Handwerk, J.H. and O.L. Kruger, *Phosphides, sulfides and other actinide fuel compounds as possible ceramic fuel materials.* Nuclear Engineering and Design, 1971. **17**(3): p. 397-408.

189. Allbutt, M. and R.M. Dell, *Chemical aspects of nitride, phosphide and sulphide fuels.* Journal of Nuclear Materials, 1967. **24**(1): p. 1-20.
190. Saibaba, M., S.V. Varamban, and C.K. Mathews, *Effect of oxygen and nitrogen impurities on the thermodynamic properties of uranium-plutonium mixed carbide fuel.* Journal of Nuclear Materials, 1987. **144**(1): p. 56-64.
191. Ogawa, T., et al., *Actinide nitrides and nitride–halides in high-temperature systems.* Journal of Alloys and Compounds, 1998. **271–273**: p. 347-354.
192. Potter, P.E., *The volatility of plutonium carbides.* Journal of Nuclear Materials, 1964. **12**(3): p. 345-348.